

DEVELOPMENT OF A BONE TUMOR MODEL UNDER IN VITRO
CONDITIONS

A THESIS SUBMITTED TO
THE GRADUATE SCHOOL OF NATURAL AND APPLIED SCIENCES
OF
MIDDLE EAST TECHNICAL UNIVERSITY

BY

AYLİN KÖMEZ

IN PARTIAL FULFILLMENT OF THE REQUIREMENTS
FOR
THE DEGREE OF DOCTOR OF PHILOSOPHY
IN
BIOTECHNOLOGY

MARCH 2019

Approval of the thesis:

**DEVELOPMENT OF A BONE TUMOR MODEL UNDER IN VITRO
CONDITIONS**

submitted by **AYLİN KÖMEZ** in partial fulfillment of the requirements for the degree of **Doctor of Philosophy in Biotechnology Department, Middle East Technical University** by,

Prof. Dr. Halil Kalıpçılar
Dean, Graduate School of **Natural and Applied Sciences**

Assoc. Prof. Dr. Can Özen
Head of Department, **Biotechnology**

Prof. Dr. Vasıf Hasırcı
Supervisor, **Dept. of Biological Sciences, METU**

Prof. Dr. Nesrin Hasırcı
Co-Supervisor, **Dept. of Chemistry, METU**

Examining Committee Members:

Prof. Dr. Cemil Yıldız
Dept. of Orthopedics and Traumatology, SBU

Prof. Dr. Vasıf Hasırcı
Dept. of Biological Sciences, METU

Prof. Dr. Aykut Özkul
Dept. of Virology, Ankara University

Prof. Dr. Tülin Güray
Dept. of Biological Sciences, METU

Assoc. Prof. Dr. Çağdaş Devrim Son
Dept. of Biological Sciences, METU

Date: 22.03.2019

I hereby declare that all information in this document has been obtained and presented in accordance with academic rules and ethical conduct. I also declare that, as required by these rules and conduct, I have fully cited and referenced all material and results that are not original to this work.

Name, Surname: Aylin Kömez

Signature :

ABSTRACT

DEVELOPMENT OF A BONE TUMOR MODEL UNDER IN VITRO CONDITIONS

Kömez, Aylin

Doctor of Philosophy, Biotechnology

Supervisor: Prof. Dr. Vasıf Hasırcı

Co-Supervisor: Prof. Dr. Nesrin Hasırcı

March 2019, 140 pages

Osteosarcoma is one of the most common types of primary bone cancerous tumor. The structure of this tumor is solid, hard and irregular. Three dimensional (3D) models mimicking tumor tissue are needed for screening efficacy of the anticancer drugs for an effective personalized therapy. This study describes the design and production of a 3D bone tumor model (BTM) by using tissue engineering approach, and shows its capability to assess the efficacy of an anticancer drug. The model consists of two parts: (1) poly(lactic acid-co-glycolic acid) (PLGA)/beta-tricalcium phosphate (β -TCP) scaffold seeded with human fetal osteoblastic cells (hFOB) and human umbilical vein endothelial cells (HUVECs) (serve as the healthy microenvironment around the bone tumor tissue), and (2) collagen sponge seeded with human osteosarcoma cells (Saos-2) (mimic the tumor tissue). The second part is inserted in the central cavity of PLGA/ β -TCP scaffold to form 3D BTM. Responsiveness of the developed model to anticancer drug, doxorubicin, was studied as an indicator of mimicking of bone tumor. Confocal micrographs on day 21 of incubation present migration of HUVEC cells to the tumor region. Increase in expression of angiogenic factors (VEGF, bFGF, and IL-8) in the tumor component also confirms cell migration. Doxorubicin demonstrated high efficacy when applied to the BTM model, and resulted in a 7-fold decrease in

viability and apoptosis of Saos-2 cells (measured by caspase-3 enzyme activity). These show the suitability of the model in screening drug efficacies for personalized treatments.

Keywords: Osteosarcoma, Bone Tissue Engineering, Bone Tumor Model, Doxorubicin, Drug Efficacy Screening

ÖZ

İN VİTRO KOŞULLARDA KEMİK TÜMÖR MODELİ GELİŞTİRİLMESİ

Kömez, Aylin
Doktora, Biyoteknoloji
Tez Danışmanı: Prof. Dr. Vasıf Hasırcı
Ortak Tez Danışmanı: Prof. Dr. Nesrin Hasırcı

Mart 2019, 140 sayfa

Osteosarkom kemikte en yaygın olarak bulunan primer tümör çeşitlerinden biridir. Katı, sert ve düzensiz bir yapısı vardır. Hastaya özel etkili bir terapi için kanser ilaçlarının etkinliğini incelemek amacıyla tümör dokusunu taklit eden üç boyutlu (3B) modeller gereklidir. Bu çalışmanın amacı, doku mühendisliği yaklaşımı kullanılarak *in vitro*, 3B bir kemik tümör modeli (KTM) geliştirilmesi ve bu modelin osteosarkom tedavisi için antikanser ilaç geliştirmede bir test aracı olarak kullanılabilirliğinin araştırılmasıdır. Model iki kısımdan oluşmaktadır: (1) kemik tümör dokusu etrafındaki sağlıklı mikroçevreyi taklit etmek için, insan fetal osteoblastik hücreleri (hFOB) ve insan umbilikal ven endotel hücreleri (HUVEC) ile kültür edilmiş poli(laktik asit-ko-glikolik asit) (PLGA)/beta-trikalsiyum fosfat (β -TCP) iskeleler ve (2) tümör dokusunu taklit etmek için insan osteosarkom hücreleri (Saos-2) ile kültür edilmiş kollajen süngerler. İkinci parça, 3B KTM oluşturmak için PLGA/ β -TCP iskelenin merkez boşluğuna yerleştirilir. Geliştirilen modelin antikanser ilacı olan doxorubicine karşı duyarlılığı kemik tümörünü taklit etme yeteneğinin bir göstergesi olarak incelenmiştir. İnkübasyonun 21. gününde konfokal mikrograflar HUVEC hücrelerinin tümör bölgesine göç ettiklerini göstermektedir. Tümör bileşenindeki anjiyojenik faktörlerin (VEGF, bFGF ve IL-8) ekspresyonundaki artış, hücre göçünü de doğrular. Doxorubicin, KTM modeline uygulandığında yüksek etkinlik göstermiş

ve Saos-2 hücre canlılığında 7 katlık bir azalma ve hücre apoptozu (kaspaz-3 enzim aktivitesi ile ölçülmüş) ile sonuçlanmıştır. Bunlar, modelin hastaya özel kanser tedavileri için ilaç etkinliklerinin araştırılmasındaki uygunluğunu göstermektedir.

Anahtar Kelimeler: Osteosarkom, Kemik Doku Mühendisliği, Kemik Tümör Modeli, Doxorubicin, İlaç Etkinlik Testi

Dedicated to my lovely family

ACKNOWLEDGMENTS

I would like to express my special endless thanks and gratitude to my thesis supervisor, Prof. Dr. Vasıf Hasırcı for his continuous guidance, advice, support, encouragement and insight throughout my thesis. I feel very lucky to have had the opportunity to do my thesis research jointly in his laboratory and under his guidance. He has opened many paths in my life and has been more than an advisor to me.

I am very grateful to my co-supervisor Prof. Nesrin Hasırcı who has been a significant role model to me and has kind consideration regarding my academic requirements. I was fortunate for her mentoring and valuable advices which improved my scientific experience to an international level.

I would also like to thank my thesis monitoring committee members, Prof. Dr. Tülin Güray and Prof. Dr. Cemil Yıldız for all their collaboration, suggestions, and useful discussions.

I offer my deepest blessings to my family who supported me in any respect during my life. I owe my deepest gratitude to my mother Anakadın Kömez, my father Seyfi Kömez, my sisters Güler Kömez and Aslıhan Kömez and my brother Mesut Kömez for their understanding, love, caring, support, encouragement, patience and trust in me not only for this study, but for all my life. I feel very lucky to be raised in their hands. Life would be meaningless without sharing with them.

I am deeply thankful to my fiancée, my partner in life, my best friend, the best gift of my life Uluç Bilecen for his endless love, patience, support, encouragement and understanding.

I would like to thank to all my labmates and graduates for their friendship and support.

Lastly, I gratefully acknowledge TÜBİTAK (Scientific and Technological Research Council of Turkey) for their support through BİDEB 2211-C Ph.D. scholarship.

TABLE OF CONTENTS

ABSTRACT	v
ÖZ.....	vii
ACKNOWLEDGMENTS	x
TABLE OF CONTENTS	xi
LIST OF TABLES	xvi
LIST OF FIGURES	xvii
LIST OF ABBREVIATIONS	xxi
CHAPTERS	
1. INTRODUCTION	1
1.1. Bone Structure	1
1.1.1. Bone Anatomy	1
1.1.2. Bone Cells.....	2
1.1.3. Bone ECM Components	4
1.1.4. Bone Remodeling	5
1.1.5. Bone Mechanics and Mechanobiology.....	6
1.2. Tissue Engineering	6
1.3. Bone Tissue Engineering.....	7
1.4. Cancer.....	9
1.5. Cancerous Tumor of Bone-Osteosarcoma (OS).....	10
1.5.1. Bone Tumor Microenvironment	12
1.6. Tumor Models	15
1.6.1. Conventional Tumor Models	15

1.6.1.1. Two Dimensional (2D) Monolayer Culture	16
1.6.1.2. Animal Models	16
1.6.2. Three-Dimensional Culture Systems.....	18
1.6.2.1. Spheroids (Scaffold Free)	20
1.6.2.2. Device-assisted Tumor Models	21
1.6.2.3. Matrix-assisted Tumor Models (with Scaffold)	23
1.7. Approach, Aim, and Novelty of the Study.....	29
2. MATERIALS AND METHODS	33
2.1. Materials.....	33
2.2. Methods.....	34
2.2.1. Preparation of Sponges.....	34
2.2.1.1. Preparation of PLGA/TCP Sponges	34
2.2.1.2. Preparation of Collagen Sponges.....	35
2.2.2. Characterization of Sponges.....	36
2.2.2.1. Contact Angle Measurement	36
2.2.2.2. Degradation Test.....	36
2.2.2.3. Compressive Mechanical Test.....	37
2.2.2.4. Scanning Electron Microscopy (SEM).....	37
2.2.2.5. Micro Computed Tomography (MicroCT) Analysis.....	37
2.2.3. Preparation of Healthy Bone and Tumor Mimics	38
2.2.4. Characterization of Healthy Bone and Tumor Mimics	39
2.2.4.1. Alamar Blue Cell Viability Assay	39
2.2.4.2. Alkaline Phosphatase (ALP) Activity	40
2.2.4.3. Immunocytochemistry	41

2.2.4.4. SEM	41
2.2.4.5. MicroCT Analysis.....	42
2.2.5. Development of 3D Bone Tumor Model (BTM).....	42
2.2.5.1. Development of Model in Collagen Scaffolds (BTM-S).....	42
2.2.5.2. Development of Scaffolds with the Spheroids (BTM-SS).....	43
2.2.5.3. Development of GelMA Scaffolds (BTM-G).....	45
2.2.6. Characterization of Bone Tumor Models	47
2.2.6.1. Live/Dead Cell Viability Assay	47
2.2.6.2. Alamar Blue Cell Viability Assay	47
2.2.6.3. Alkaline Phosphatase (ALP) Activity	47
2.2.6.4. Immunocytochemistry	48
2.2.6.5. SEM	49
2.2.6.6. MicroCT Analysis.....	49
2.2.6.7. Molecular Analysis of Angiogenesis	49
2.2.7. Efficacy of Anticancer Agent on BTM-S Model.....	53
2.2.7.1. Preparation of Dose-Response Curve	53
2.2.7.2. Alamar Blue Cell Viability Assay	54
2.2.7.3. Live/Dead Assay	54
2.2.7.4. Caspase-3 Enzyme Activity Assay	54
2.2.8. Statistical Analysis.....	54
3. RESULTS AND DISCUSSION.....	55
3.1. Characterization of PLGA/TCP and Collagen Sponges.....	55
3.1.1. Wettability	55
3.1.2. Degradation.....	57

3.1.3. Compressive Mechanical Properties	58
3.1.4. Microarchitecture	60
3.1.5. MicroCT Analysis	65
3.2. Characterization of Cell Seeded Healthy Bone and Tumor Mimics.....	67
3.2.1. Alamar Blue Cell Viability Assay.....	67
3.2.2. Alkaline Phosphatase (ALP) Activity	70
3.2.3. Immunocytochemistry.....	71
3.2.4. SEM Analysis.....	75
3.2.5. MicroCT Analysis	77
3.3. Characterization of the Complete Bone Tumor Model, BTM-S	83
3.3.1. Microscopy of BTM-S	83
3.3.2. MicroCT	86
3.3.3. Molecular Analysis of Angiogenesis of BTM-S.....	87
3.4. Characterization of Bone Tumor Models, BTM-SS and BTM-G	91
3.4.1. Characterization of Saos-2 Spheroids	92
3.4.1.1. Morphology of Saos-2 Spheroids	92
3.4.1.2. Live/Dead Assay of Saos-2 Spheroids	93
3.4.1.3. SEM Analysis of Saos-2 Spheroids.....	95
3.4.2. Quantification of Cell Numbers in BTM-SS.....	95
3.4.3. Live/Dead Assay of BTM-SS.....	96
3.4.4. Alkaline Phosphatase (ALP) Activity of Cells in BTM-SS	97
3.4.5. MicroCT Analysis of BTM-SS	98
3.4.6. Immunocytochemistry of BTM-SS and BTM-G	100
3.4.7. SEM of BTM-SS and BTM-G	105

3.5. Efficacy of Anticancer Agent on BTM-S.....	107
3.5.1. Dose-Response Curve and Determination of IC ₅₀	107
3.5.2. Alamar Blue Cell Viability Assay	108
3.5.3. Live/Dead Assay.....	111
3.5.4. Caspase-3 Enzyme Activity Assay	112
4. CONCLUSION.....	115
REFERENCES.....	117
5. APPENDICES	133
A. Alamar Blue Assay Calibration Curve for hFOB and HUVECs	133
B. Alamar Blue Assay Calibration Curve for Saos-2.....	135
C. Standard Curve for DNA Quantification	137
CURRICULUM VITAE	139

LIST OF TABLES

TABLES

Table 1.1. Components of the organic phase of bone matrix (Salgado et al., 2004)...	5
Table 2.1. Reagent volumes used for first step of cDNA synthesis.	50
Table 2.2. Reagent volumes used for second step of cDNA synthesis.....	51
Table 2.3. Reagent volumes used for the qRT-PCR reaction.....	51
Table 2.4. qRT-PCR reaction conditions for VEGF, bFGF and IL-8 primers.	52
Table 2.5. qRT-PCR primers and the amplicon sizes.....	52
Table 3.1. Contact angles of PLGA/TCP and collagen sponges.	55
Table 3.2. Young's modulus of PLGA/TCP sponges, trabecular bone and collagen sponges.	60
Table 3.3. Porosity of unseeded and cell seeded PLGA/TCP scaffolds.....	77

LIST OF FIGURES

FIGURES

Figure 1.1. General appearance of a long bone.....	2
Figure 1.2. Classification of bone cells based on source, resorption, and formation function	3
Figure 1.3. Anatomy of sites where most frequent bone tumor development is detected.. ..	11
Figure 1.4. Interrelation between bone environment cell types and osteosarcoma. ..	15
Figure 1.5. Mouse osteosarcoma models.	17
Figure 1.6. 3D in vitro cancer models that are designed to mimic in vivo tumor.....	19
Figure 1.7. The physical and cellular components in 3D bone tumor models.....	24
Figure 1.8. Development of bone tumor model.	30
Figure 2.1. Preparation of PLGA/TCP sponge.	35
Figure 2.2. Preparation of collagen sponge.....	36
Figure 2.3. Preparation of the (A) healthy bone mimic, and (B) tumor mimic.	39
Figure 2.4. Principle of Alamar Blue cell viability assay.	39
Figure 2.5. Preparation of BTM-S.	43
Figure 2.6. Preparation of Saos-2 spheroid.....	44
Figure 2.7. Preparation of BTM-SS.	45
Figure 2.8. Preparation of BTM-G.....	46
Figure 3.1. Degradation of the PLGA/TCP sponges in PBS	57
Figure 3.2. Enzymatic degradation of the UXL-CS and DHT-CS in collagenase type II solution	58
Figure 3.3. Characteristic stress-strain curves of the sponges.	59
Figure 3.4. SEM micrographs of the PLGA/TCP sponges.	61
Figure 3.5. Energy dispersive X-ray (EDX) analysis of a NaCl particle and PLGA/TCP sponges before and after leaching.	62

Figure 3.6. SEM micrographs of the PLGA/TCP scaffolds.	63
Figure 3.7. SEM micrographs of oxygen plasma treated and untreated PLGA/TCP scaffold surfaces.	64
Figure 3.8. SEM micrographs of collagen scaffolds.	65
Figure 3.9. MicroCT images of the PLGA/TCP sponges after salt leaching.	66
Figure 3.10. MicroCT images of the DHT-CS.	67
Figure 3.11. Cell proliferation of hFOB/HUVEC on the PLGA/TCP scaffolds.....	68
Figure 3.12. Cell proliferation of Saos-2 on the DHT-CS.....	69
Figure 3.13. Alkaline phosphatase (ALP) activity of hFOB cells in healthy bone mimic.	70
Figure 3.14. CLSM micrographs of the hFOB and HUVECs on PLGA/TCP scaffolds on Days 7, 14 and 21	72
Figure 3.15. CLSM micrographs of the horizontal section of the hFOB and HUVECs on the PLGA/TCP scaffolds on Day 28	73
Figure 3.16. CLSM micrographs of the Saos-2 cells on collagen scaffolds.....	74
Figure 3.17. CLSM micrographs of a horizontal cross section of the collagen scaffolds showing the Saos-2 cells.....	75
Figure 3.18. SEM micrographs of hFOB/HUVEC cells on PLGA/TCP scaffold.....	75
Figure 3.19. SEM micrographs of Saos-2 cells on collagen scaffold.....	76
Figure 3.20. MicroCT images of cell-free and hFOB/HUVECs seeded PLGA/TCP scaffolds.	78
Figure 3.21. MicroCT images (Top View) and X-ray absorption spectra of the horizontal cross section of the cell-free and hFOB/HUVECs seeded PLGA/TCP scaffolds.....	79
Figure 3.22. MicroCT images of cell-free and Saos-2 seeded on the DHT-CS	81
Figure 3.23. MicroCT images and X-ray absorption spectra of the horizontal cross section of the cell-free and Saos-2 seeded collagen scaffolds	82
Figure 3.24. MicroCT and CLSM images of the Saos-2 seeded collagen scaffolds.	83
Figure 3.25. CLSM and SEM analysis of BTM-S.....	84
Figure 3.26. CLSM analysis of BTM-S.....	85

Figure 3.27. MicroCT images of a top view of the cell-free and cell seeded BTM-S on Days 7, 14, 21.	87
Figure 3.28. Analysis of VEGF and b-FGF secretion in the BTM-S	88
Figure 3.29. Agarose gel electrophoresis of IL-8 genes of Saos-2 cells on TCPS surface (TCPS), collagen sponge (Coll) and collagen sponge in bone tumor model (Coll/BTM-S) on Days 7, 14 and 21	90
Figure 3.30. Light microscopy images of Saos-2 spheroids on Day 7 and Day 40. ...	92
Figure 3.31. Cell viability assays of Saos-2 spheroids	93
Figure 3.32. Bright field microscopy image of cell spheroid (top) and the same image with pathophysiological gradients (bottom)	94
Figure 3.33. SEM of Saos-2 spheroids.	95
Figure 3.34. Cell (Saos-2 + hFOB + HUVEC) proliferation in the BTM-SS.....	96
Figure 3.35. CLSM micrographs of Live/Dead assay of the BTM-SS.....	97
Figure 3.36. Total ALP activities of hFOB and Saos-2 spheroids in the BTM-SS ...	98
Figure 3.37. MicroCT images of the cell-free and cell seeded BTM-SS (PLGA/TCP sponge+collagen sponge) on Days 7, 14, 21.....	99
Figure 3.38. MicroCT images (top view) and X-ray absorption spectra of the horizontal section of the cell-free and cell seeded BTM-SS (PLGA/TCP sponge+collagen sponge together) on Days 7, 14, and 21	99
Figure 3.39. CLSM micrographs of hFOB, HUVECs, Saos-2 cells and spheroids in the BTM-SS on Days 7 and 21	101
Figure 3.40. CLSM micrographs of BTM-G generated by encapsulating of Saos-2 spheroids in GelMA hydrogel (Day 21)	102
Figure 3.41. Microscopy analysis of Saos-2 spheroids containing BTM-SS and BTM-G on Day 21	104
Figure 3.42. SEM micrographs of BTM-SS on Days 7, 14, and 21	105
Figure 3.43. SEM analysis of bone tumor models on Day 21	106
Figure 3.44. Log Dose-Response curve of Saos-2 cells grown in a tissue culture plate treated with doxorubicin	108

Figure 3.45. Alamar Blue cell viability test results of doxorubicin-treated BTM-S. Reduction (%) of the dye is proportional to live cell number.	108
Figure 3.46. Cell viability assay of doxorubicin-treated BTM-S model using Live/Dead staining.....	111
Figure 3.47. Caspase-3 enzyme activity of doxorubicin treated BTM-S	113

LIST OF ABBREVIATIONS

µm	micrometer
2D	Two Dimensional
3D	Three Dimensional
Ab	Antibody
BSA	Bovine Serum Albumin
CLSM	Confocal Laser Scanning Microscopy
CO ₂	Carbon Dioxide
CT	Computer Tomography
DAPI	4', 6-diamidino-2-phenylindole
DMEM	Dulbecco's Modified Eagle Medium
DMSO	Dimethyl Sulfoxide
ECM	Extracellular Matrix
EDTA	Ethylenediaminetetraacetic Acid
EGM-2	Endothelial Growth Medium
FBS	Fetal Bovine Serum
GelMA	Methacrylated Gelatin
hFOB	Human Fetal Osteoblast Cells
HUVEC	Human Umbilical Vein Endothelial Cells
MW	Molecular Weight
PBS	Phosphate Buffer Saline
PLGA	Poly(lactic acid-co-glycolic acid)
Pen/Strep	Penicillin/Streptomycin
Saos-2	Human Osteosarcoma Cells
SEM	Scanning Electron Microscopy
TCPS	Tissue Culture Polystyrene

CHAPTER 1

INTRODUCTION

1.1. Bone Structure

Bone is a complex tissue and it has critical roles in the body. It is mainly composed of mineralized osseous tissue mainly consisting of collagen and calcium phosphate and includes marrow, endosteum and periosteum, nerves, blood vessels, and cartilage in its structure.

1.1.1. Bone Anatomy

Bone is classified in terms of its shape such as long, short, irregular or flat. It has an inorganic component, hydroxyapatite (HAp) (a specific type of calcium phosphate mineral), $(Ca_{10}(PO_4)_6(OH)_2)$, and an organic component (mostly type I collagen) in addition other types of proteins. Cellular organization, mechanical properties, complex hierarchical physical structure, and molecules constitute and contribute to the excellent functionality of bone. Long bones have three regions: diaphysis, epiphysis, and epiphyseal plates (Figure 1.1A). The long portion of bone is called as diaphysis and it contains compact (cortical) bone. Compact bone builds up approximately 80% of the total mass of bone. Compact bone basically consists of the Haversian system and the closely packed osteons. Osteons are generated by concentric rings (lamellae) that surround Haversian canal. In the space between rings, called as lacunae, osteocytes are located. Passage through the hard matrix is provided by small channels (canaliculi) that radiate from the lacunae toward the Haversian canals. A solid mass of compact bone is created by tightly packaging of Haversian system and the osteogenic canals are composed of vessels that are oriented parallel to long axis of the bone. These blood vessels are interconnected with the vessels that are found on the surface of the bone (Figure 1.1B).

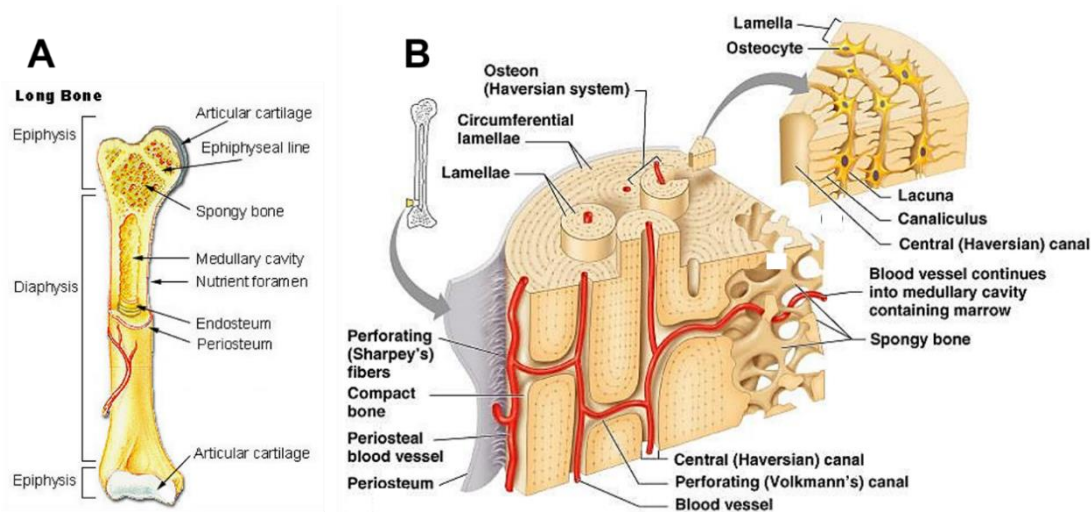


Figure 1.1. General appearance of a long bone. (A) The basic anatomy differences in cortical and cancellous bone and (B) microstructural features in cortical bone.

The epiphysis is composed of cancellous (spongy) bone and is surrounded by articular cartilage that introduces the low-friction contact with neighboring bones. Spongy bone is less dense than compact bone. Actually, it is formed by plates (trabeculae) and struts of bone located next to small, irregular cavities that consist of bone marrow. Unlike compact bone in which canaliculi is connected with Haversian canal, cavities are connected with canaliculi in the spongy bone to supply blood. It may be considered that spongy bone construct is designed in a manner that provides maximum strength (Alghazali et al., 2015).

1.1.2. Bone Cells

Bone cells originate from two cell lines: mesenchymal stem cells and hematopoietic stem cells. These cells differentiate into several types of cells that are classified based on morphology, function, and their location in the bone tissue (Figure 1.2). Osteoblasts play an important role in the formation and organization of extracellular matrix and mineralization, and they are located on the surface of the bone. They are differentiated from mesenchymal cells located in the bone marrow and secrete organic phase of the extracellular matrix (ECM) of bone. The main product synthesized by mature

osteoblasts is type I collagen that produces 90% of the protein in bone, bone specific vitamin-K dependent proteins, osteocalcin, matrix Gla protein, phosphorylated glycoproteins such as bone sialoproteins I and II, osteopontin and osteonectin, proteoglycans and alkaline phosphatase. Undifferentiated mesenchymal cells are capable of developing into osteoblasts and are referred to as preosteoblasts. They are located in the canals, endosteum, periosteum, and marrow, and they are characterized by their irregular shape, a single nucleus with minimum cytoplasm, and a few organelles. These cells have a critical role in the process of bone healing when they are stimulated to differentiate into osteoblasts. A proportion of osteoblasts become trapped in the lacunae within the bone matrix as osteocytes. They provide intercellular communications and form a large and complex network of cells which plays an important role in stress detection. Another important role of osteocytes is the breakdown of bone matrix to release calcium ions and regulate calcium homeostasis.

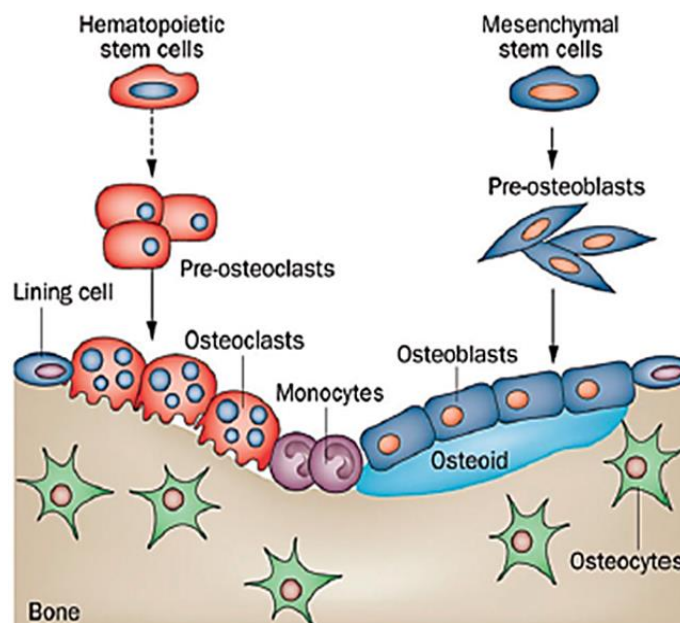


Figure 1.2. Classification of bone cells based on source, resorption, and formation function (Lian et al., 2012).

Osteoclasts are polarized cells differentiated from hematopoietic stem cells and they are found to be attached to the bone surface via integrins. They show osteoclastic bone resorption which start with mineral dissolution and followed by degradation of the organic phase. These processes are based on secretion of lysosomal enzyme and an acidic microenvironment. Osteoclasts actively synthesize lysosomal enzymes, especially the tartrate-resistant isoenzyme of acid phosphatase (TRAP) (a marker of the osteoclast phenotype), and cysteine-proteinases, such as cathepsins, which are responsible for degrading collagen (Jang et al., 2009).

1.1.3. Bone ECM Components

Bone matrix consists of an organic component, called osteoid, and an inorganic component contained primarily of hydroxyapatite crystals. The main organic component of bone is type I collagen that supports mineralization by acting as a template. Type V collagen is also present in ECM of bone. Along with collagenous part of the bone matrix, non-collagenous proteins are also found in the bone structure (Table 1.1).

Osteocalcin constitutes 15% of the non-collagenous proteins of the bone. Osteoblasts express this protein. The characteristic of osteocalcin is the γ -carboxyglutamic acid residues (Gla) which enhance binding to the mineral, hydroxyapatite, with its high affinity. It also plays role in bone turnover or mineralization. Osteopontin also supports cell adhesion to the bone surface by its Arg-Gly-Asp (RGD) integrin recognition motifs. Its acidic nature helps it to regulate the formation of calcium crystals in bone. These non-fibrillar organic matrix components osteocalcin and osteopontin also contributes to nanoscale mechanical properties by acting as a bonding agent between collagen fibrils.

Table 1.1. *Components of the organic phase of bone matrix (Salgado et al., 2004).*

Bone extracellular matrix constituent	Functions and properties
Collagenous proteins	
Type I Collagen	Provides framework for skeletal structure; matrix calcification
Type III Collagen	Promotes bone formation
Type V Collagen	Structural backbone of bone
Non-collagenous proteins	
Osteonectin	Glycoprotein; binds Ca ²⁺ and collagen; nucleates hydroxylapatite
Fibronectin	Osteoblast attachment to substrate
Osteopontin	Sialoprotein; constituent of cement line; involved in bone remodelling
Bone Sialoprotein	Sialoprotein; constituent of cement line
Osteocalcin	Skeletal gla protein; late marker of osteogenic phenotype; involved in bone remodelling; it may also be involved in the control of mineralization through its inhibition.

The proteoglycans (e.g., decorin, lumican, biglycan, epiphycan) of bone matrix are less abundant than those found in cartilage matrix, consisting of a small protein core and only 1 or 2 glycosaminoglycan (chondroitin sulfate) side chains. The bone proteoglycans have critical roles in bone formation, such as cell proliferation and matrix mineralization (Craig et al., 2016).

Bone ECM also helps the function of growth factors. Intracellular signaling pathways are initiated by ECM proteins and contribute to the regeneration process. It acts like substratum for cell adhesion and differentiation and also mineralization (Alford et al., 2015).

1.1.4. Bone Remodeling

Bone remodeling plays an important role in skeletal integrity, healing, calcium regulation in blood and adjustment of changes in bone stress profile. Bone remodeling is performed by the coupled activities of bone-resorbing osteoclasts and bone-forming

osteoblasts arranged within temporary structures called as “basic multicellular units” (BMUs). Forming of BMUs is essential for limited change in bone volume during remodeling. It is a complex process by which old bone is continuously replaced with new tissue in successive phases in a BMU; these phases are origination, osteoclast recruitment, resorption, osteoblast recruitment, mineralization and resting (Raggatt and Partridge, 2010).

1.1.5. Bone Mechanics and Mechanobiology

Mechanical stimuli play a critical role in bone physiology. *In vivo* loading stimulates the bone cells and affects bone modeling and remodeling. The exact mechanism of response of the bone cells to mechanical stimuli is not clear. There are two suggested models: (1) each bone cells sense the mechanical forces and the response is at the cellular level or (2) some sensory bone cells sense mechanical stimuli and secrete biochemical signals for neighboring cells to respond to and this is at the tissue level.

The tensile strength of cortical bone was measured as 78-151 MPa while its compressive strength was determined as 131-224 MPa. In the longitudinal direction, the Young’s Modulus of cortical bone is approximately 17-20 GPa and it is 6-13 GPa along the traverse axis. Cancellous (trabecular) bone is softer than cortical bone and its mechanical properties change widely with porosity, density, and location of the bone. Trabecular bone shows viscoelastic behavior (demonstrates dependence on loading rate). Its strength is 5-10 MPa and modulus is 50-100 MPa (Porter et al., 2009).

1.2. Tissue Engineering

Tissue engineering is comparatively a new area that uses cells, cell carriers (scaffolds), and bioactive agents (growth factors) to generate living tissue. In 1993, tissue engineering was defined as “an interdisciplinary field of research that applies the principles of engineering and the life sciences towards the development of biological substitutes that restore, maintain, or improve tissue function” (Langer and Vacanti, 1993). Its fundamental aim is to regenerate living tissues in order to replace damaged or lost organs and tissues of living organisms (Rosso et al., 2004). Biomaterials are

used in the form of three dimensional scaffolds to enable cell attachment and provide mechanical reinforcement to growing tissue. The cells on the scaffold secrete the extracellular matrix (ECM) to enhance mechanical and physical properties of tissues and organs (Zhang et al., 2005). Viable cells are used to generate the new tissue either seeded *in vitro* or implanted *in vivo*. In order to control the cellular functions, growth factors appropriate for tissue are chosen (Naito et al., 2011).

1.3. Bone Tissue Engineering

Bone tissue engineering (BTE) is a good alternative to current clinical treatments to regenerate bone. BTE needs to well understand the bone structure, bone mechanics, and tissue formation since it targets to form new functional bone tissue. There are several key components of BTE: (1) a biocompatible scaffold that mimics the natural bone ECM, (2) osteogenic cells to seed on the scaffold, (3) bone morphogenic agents that stimulate the cells to differentiate into desirable type, and (4) vascularization to enable sufficient nutrient supply to the growing tissue (Amini et al., 2012).

Tissue engineered bone constructs can not only be transplanted as a graft, but also can be used as 3D tissue models to study diagnosis and therapy of bone diseases and to analyze them at the cellular and molecular level. One of the main challenges is the choice of an appropriate biomaterial which can mimic the natural bone tissue matrix with its mechanical and biological characteristics (Melke et al., 2016). Bone scaffold should be structurally, functionally, and mechanically mimic the healthy bone. In addition, scaffolds should support cell adhesion, cell proliferation and differentiation for bone tissue regeneration (Venkatesan et al., 2015).

Today, the most widely used materials for construction of bone scaffold are biodegradable polymers. These have been accepted as ideal materials for tissue engineering. Biodegradable polymers are divided into two categories; natural and synthetic.

Natural biodegradable polymers are collagen, fibrinogen, chitosan, starch, hyaluronic acid and poly(hydroxybutyrate). These are obtained from animal and plant sources.

The advantages of using natural polymers are low immunogenic response, high bioactivity, good interaction with host tissue and unlimited source for some polymers such as starch and chitosan. There are also some disadvantages of natural polymers. They are expensive and their processability is difficult. In addition, their degradation time changes from person to person since degradability depends on the certain enzyme, and the activity of enzymes vary from patient to patient (Salgado et al., 2004).

Synthetic biodegradable polymers are poly(α -hydroxy acids) especially poly(glycolic acid) (PGA), poly(lactic acid) (PLA) and their copolymers poly(lactic acid-co-glycolic acid) (PLGA), poly(ϵ -caprolactone), poly(propylene fumarates), poly(carbonates), poly(phosphazenes), and poly(anhydrides). They have more advantages than the natural biodegradable polymers since they can be synthesized with the desired properties. In addition, they are economical do not cause severe immunologic responses (Zhou et al. , 2012).

There are several scaffold processing techniques for bone tissue engineering. An appropriate processing technique is chosen according to the features of the desired scaffold that will be used to construct bone tissue. The processing technique must not influence the chemical structure of biomaterial. Until now, solvent casting, phase inversion, fiber bonding, melt based technologies, freeze drying, rapid prototyping and electrospinning are used as scaffold processing techniques for bone tissue engineering.

As cell source, different types of stem cells have been used and their differentiation to bone-forming cells was achieved by controlling the culture condition. These are bone marrow (BM) or umbilical cord blood (UCB) mesenchymal stem cells (MSCs), and adipose stem cells (ADSCs), muscle-derived stem cells (MDSCs) and dental pulp stem cells (DPSCs) (Seong et al., 2010). Besides stem cells, osteoblastic cells are used in BTE. They are taken from patients' bone tissue with biopsies. Generally, it is considered as convenient cells for bone reconstruction since the natural bone also consists of osteoblastic cells (Baghaban and Faghihi, 2011).

Growth factors play a critical role in the formation of bone tissue and they are required for proliferation, differentiation, adhesion, and migration of cells for BTE. Bone morphogenetic proteins (BMPs), transforming growth factor beta (TGF- β), fibroblast growth factors (FGFs), insulin growth factor I and II (IGF I/II), and platelet derived growth factor (PDGF) are among widely used growth factors. They act as signaling molecules like cytokines and induces cells after binding specific receptors on cell surfaces which initiate signal transduction pathways and expression of bone proteins is predominated (Salgado et al., 2004).

1.4. Cancer

Cancer is a group of diseases defined as the uncontrolled growth and division of abnormal cells that can invade nearby tissues. Cancer cells can also spread to other parts of the body through the blood and lymphatic system. If the cell spread is not controlled, it can result in death.

Worldwide, one in seven deaths results from cancer; cancer causes more deaths than the combination of AIDS, tuberculosis, and malaria. Today, millions of people are living with cancer or have had cancer (“Cancer Facts and Statistics 2015, Research, American Cancer Society,” 2015).

In the field of cancer research, notable time and effort are exerted to develop and screen new cancer drugs that will improve patient survival and decrease morbidity. Annually, more than \$5 billion are spent on cancer research by the U.S. government; it corresponds to 20% of the total research funding provided by the National Institutes of Health (NIH) and much of this is aimed at finding new cancer therapeutics (“NIH Categorical Spending-NIH Research Portfolio Online Reporting Tools (RePORT),” 2016).

Any drug that is discovered or engineered must go through preclinical tests and clinical trials before it is considered as safe and efficient enough to enter the market. This process takes time approximately a decade and costs more than a billion dollars. However, among all the drugs that enter clinical trials, only about 5% are FDA

approved (DiMasi and Grabowski, 2007; Kola and Landis, 2004). This implies great expense both financially and clinically and much of it is consumed for compounds that will never enter clinical use. This great expense is even more dramatic in rare cancers like osteosarcoma. Although osteosarcoma is a common malignant bone tumor, it is still rare with less than 1,000 new cases each year in the United States. Since the patient base is small, it is difficult to place on record enough patients in a trial to provide clinical efficacy. Therefore, drug trials must be done at multiple institutions and longer time periods are required in order to provide requisite patient load and this all cause lots of money and time losses (Haffner, 2006; Wasfelt et al., 2006).

1.5. Cancerous Tumor of Bone-Osteosarcoma (OS)

Osteosarcoma (OS) or osteogenic sarcoma (OGS) is the most prevalent primary tumor of bones. Tumors may be benign (not cancer), or malignant (cancer). Most osteosarcomas are observed in children and young adults. Osteosarcoma commonly detected in areas where the bone is growing quickly, such as near the ends of the long bones. Primary tumors develop around the knee, either in the distal femur (lower part of thigh bone) (Figure 1.3A) (30%) or the proximal tibia (the upper part of the shinbone) (Figure 1.3B) (15%). The proximal humerus (the part of the upper arm bone close to the shoulder) (Figure 1.3C) (15%) is the other most common site. In the long bones, the tumor is usually (90%) placed in the metaphysis (Abarrategi et al., 2016).

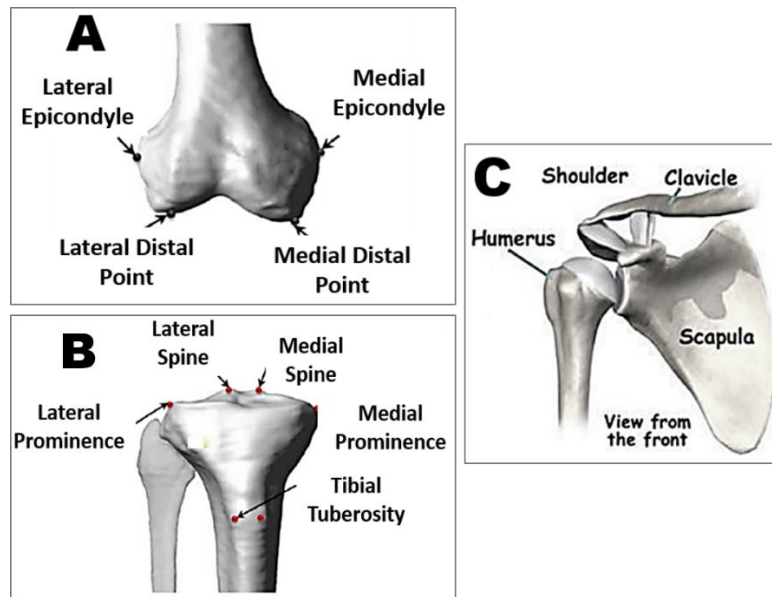


Figure 1.3. Anatomy of sites where most frequent bone tumor development is detected. (A) Distal femur, (B) proximal tibia, (C) proximal humerus (Subburaj et al., 2010).

In osteosarcoma, the tumor is primary when the underlying bone is normal and secondary when the bone is changed by some circumstances, such as radiation, coexisting Paget disease, infarction, or other disorders. Furthermore, OS is the most known radiation-induced sarcoma (Alfranca et al., 2015).

The first line treatment of OS is the surgical removal of the tumor and adjuvant chemotherapy (Rimann et al., 2014). As a primary therapy, nearly all patients get neoadjuvant intravenous combinational chemotherapy (doxorubicin and cisplatin with or without methotrexate). If complete surgical resection is not applicable or if surgical margins are not enough, radiation therapy may be applied. The postoperative chemotherapy is usually related to the size of tumor necrosis (Abarategi et al., 2016; Botter et al., 2014). OS is characterized by high local aggressiveness and rapid metastasizing potential resulting in an early onset of tumor (mean age is about 17 years) with poor survival rates. In spite of development in therapeutic strategies, involving the progression of multidrug chemotherapy, the survival rates have not changed for more than four decades. The survival rate is 75% at 5 years for located

diseases, however, two groups of patients are still at high risk. These are metastatic (general survival 40% at 5 years) or poor responders to chemotherapy (survival 20% at 5 years) (Verrecchia and R dini, 2018). To develop an effective cancer therapy, the first step has to be to understand the biology in tumor initiation and progression (Alemany-Ribes and Semino, 2014).

The histological heterogeneity of osteosarcoma may show a multipotent cell of origin, which is most probably the mesenchymal stem cell (MSC) along its path of differentiation to the osteoblastic lineage. A good understanding of osteosarcoma origin and etiology is confusing by several factors such as its extreme rearranged genome, the lack of precursor lesions and the high genetic instability preventing the detection of the driver genes. Furthermore, most osteosarcoma cases occur by sporadic means that there is no obvious hereditary cause. This induces early onset resulting into a full-blown tumor at the time of diagnosis. Moreover, although osteosarcoma is the most common primary bone tumor and in the pediatric age group it is the second highest cause of cancer-related death, its overall prevalence is low (4-5 per 1.000.000, worldwide). This makes it difficult to study the disease in large groups. Another limitation is due to the administration of pre-surgery high-dose chemotherapy. The therapy kills all cancer cells leaving very few viable tissues in the resected tumor to study (Mohseny et al., 2012). For this purpose, the complex cellular microenvironment needs to be constructed in simpler and more predictable systems. This approach helps researchers to identify and analyze the role of key chemical, mechanical and/or physical factors that might drive human pathophysiology.

1.5.1. Bone Tumor Microenvironment

To develop a bone tumor model, bone microenvironment and the cross talk between bone cancer and bone cells should be clearly understood. Tumors in the bone can develop from the bone itself or bone marrow, or metastasize from a tumor elsewhere in the body. In all cases, the special environment of the bone support cancer cells survival, proliferation, and metastasis.

Cellular component of the bone contains osteoblasts, osteoclasts, osteocytes, mesenchymal and vascular cells, and cells of the immune system and cells in the capillaries. The non-cellular component contains organic components, such as collagens, non-collagenous glycoproteins, hyaluronan and proteoglycans, and the inorganic (calcium phosphate) bone mineral. Bone has its unique characteristics such as low pH, hypoxia (low oxygen), high levels of extracellular calcium and response to different types of mechanical stimuli that are fundamental for bone homeostasis (Harada and Rodan, 2003). These special properties make an appropriate environment for survival, migration, colonization, and quiescence (being at rest) of cancer cells. Especially hypoxia and low pH in the bone control the survival and proliferation of tumor cells. Hypoxic microenvironment supports tumor metastasis and growth under favor of hypoxia inducible factor (HIF)-1 that promotes glycolytic enzymes, glucose transporters, and stimulates expression of the vascular endothelial growth factor, which initiates angiogenesis. Hypoxia also induces acidosis and increases production of lactic acid. Acidic bone environment promotes angiogenesis, stemness and metastatic behavior of the cells and initiate the production of osteoblast-stimulatory factors by osteosarcoma cell (Alfranca et al., 2015).

Most studies show that cancer cells can promote osteoclastic activation through the release of a kind of soluble factors. Among these factors, the most critical one is the parathyroid hormone-related protein (PTHrP) that stimulates many signaling pathways driving the ‘vicious cycle’ of tumor growth and bone disruption. Cancer cells can secrete factors that induce osteoclast-mediated bone resorption and inhibit osteoblasts, and increase the release of mediators from the bone matrix that stimulate tumor growth. Hypoxia and acidosis in the bone increase the spread of cancer cells from their original site to bone (bone metastasis). Extracellular acidification leads to high osteoclast resorption after increasing the release of calcium from the mineralized bone matrix that in turn propagates tumor growth. Surprisingly, metastatic cancer cells in bone not only remodel their microenvironment in order to survive, but also alter their phenotype and tend to resemble osteoblasts. As a result, cancer cells begin to

express bone matrix proteins (e.g. alkaline phosphatase) and molecules controlling the interaction between osteoblast and osteoclast. This ability to gain a bone cell phenotype is called as osteomimicry and it is an adaptive advantage that provides tumor cells a higher chance to survive and proliferate in the bone tissue (Villasante and Vunjak-Novakovic, 2015).

Until now, bone tumor microenvironment was explained in general apart from bone tumor type. In Figure 1.4, the interrelation between cell types in bone microenvironment and osteosarcoma is shown in detail (Alfranca et al., 2015).

The importance of bone tumor microenvironment in the progression of tumor directed the researchers to find a new therapeutic approach targeting the pro-tumorigenic signaling to treat OS. Studies regarding the molecular biology of cancer are currently emphasizing on the identification of the latest potential therapeutic targets with molecular principle. At this point, new treatments involving specific inhibitors, gene silencing strategies and antibodies generated to target neovascularization, immune system, osteoclast activation, growth factor signaling pathways or environment-induced drug resistance are being tested alone or in combination with conventional treatments. These targets are signaling cascades initiated by receptor tyrosine kinases (EGFR, VEGFR, IGF1R, HER2, or PDGFR), mTOR, or WNT/ β -catenin. In addition, since osteosarcoma cancer stem cells (OS-CSCs) are located in the bone microenvironment and this is critical in the regulation of tumor homeostasis, therapies targeting microenvironmental niche factors could provide the improvement of clinical response (Abarategi et al., 2016). In a study, TGF- β s that is secreted in the microenvironment and have a critical role in tumor progression was targeted rather than tumor cells themselves since tumor cells are heterogeneous in OS (Verrecchia and R dini, 2018).

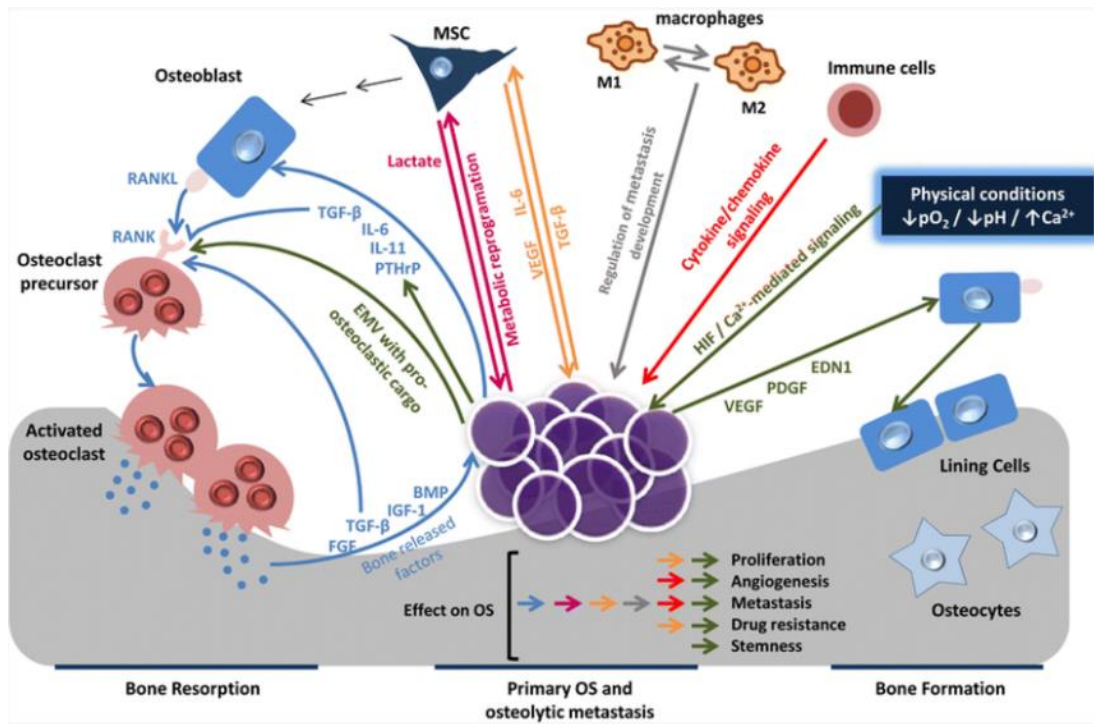


Figure 1.4. Interrelation between bone environment cell types and osteosarcoma. Adapted from (Alfranca et al., 2015).

1.6. Tumor Models

In the case of rare cancers, such as osteosarcoma, tumor models become very important since the capability to try several agents concurrently and under controlled conditions in humans is limited. The development of tumor models of OS offers a chance to discover the genetics and therapeutic targeting of OS under well prepared and controlled conditions even at times using the patient own cells.

1.6.1. Conventional Tumor Models

Conventional tumor models are either two dimensional (2D) monolayer cultures, or *in vivo* animal models.

1.6.1.1. Two Dimensional (2D) Monolayer Culture

2D monolayer culture has been used for culturing cancer cells for the last five decades and continues to be a common method for testing the efficacy of anticancer drug compounds. A 2D culture is easily performed using standardized methods, achieves rapid cell growth, uses translucent materials such as tissue culture polystyrene (TCPS) plates to observe cells in real time by light microscopy, requires no expensive special equipment, and is cost effective. However, the cancer research community is of the opinion that cells cultured on chemically inert, flat TCPS plates, under conditions of high oxygen tension, and abundant glucose and nutrients does not sufficiently mimic the cells within the native *in vivo* host (Pampaloni et al., 2007). Cancer cells are reported to lose some of their phenotypic and functional characteristics when grown in 2D monolayer cultures and this dramatically influences the susceptibility of the cells when exposed to anticancer agents. The 2D cell proliferation assays may give inaccurate data related to the anticancer potential of chemotherapeutic agents. In addition, drugs can enter the cells in 2D monolayer culture relatively easier than in 3D tissue-like cell clusters. All these factors have an impact on drug potency (Lama et al., 2013). Therefore, the critical protein targets and/or signaling cascades studied in high-throughput anti-cancer drug screening tests yield substantially different results than those in patients. These dissimilarities between 2D system and the actual tumor environment explains why the biologically targeted therapies perform well in the lab but fail in the clinic. Thus, despite of all the advantages of 2D cell culture for cancer research, if the information obtained is unreliable or even worse, it results in expensive clinical trials that give false hope to patients (Lamhamedi-Cherradi et al., 2014).

1.6.1.2. Animal Models

Animal models is a promising approach in understanding the genetic origin of OS, especially in the process of preclinical studies targeted to the development and validation of new therapeutic agents before passing clinical trials. A reliable and practical animal model of a human disease depends on mimicking the natural progress

of the disease. Unfortunately, the etiology and pathogenesis of OS are not totally understood, therefore the development of the experimental *in vivo* OS models is a challenging issue. Today, there is no ideal animal osteosarcoma model which mimics its biological, genetic and clinical properties under lab conditions (Guijarro et al., 2014). Until now, mouse and rat were the major species used as *in vivo* OS models. There are several types of osteosarcoma models such as genetically modified mouse models (GEMMs), radiation or chemically induced models and cell or tumor grafts created with the injection of murine (allograft) or human (xenograft) OS cells (Figure 1.5) (Uluçkan et al., 2015).

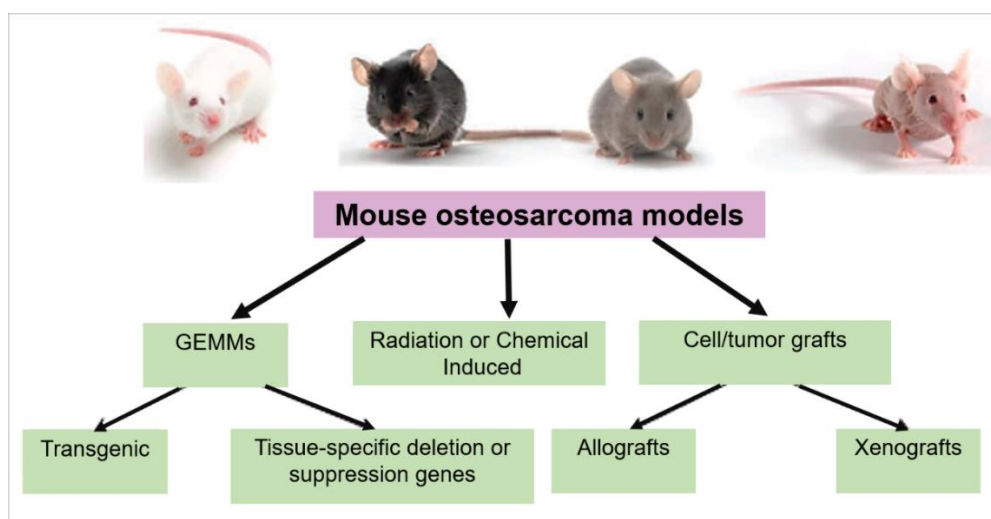


Figure 1.5. Mouse osteosarcoma models. Adapted from (Uluçkan et al., 2015).

Genetically modified mice are generally used in the cancer-drug studies however, their small size and short lifespan make some preclinical studies impossible. For instance, it is difficult to scale down radiological, thermal or surgical treatments of tumors, or carry out studies of tumor progression and remission, or long term response to therapy. In addition, cancer biology of human and mouse are different. Murine cells are very readily transformed *in vitro* than human cells, and the group of genetic events needed

for tumorigenesis is different. Mouse models may therefore not always serve as a valid model of human OS disease. However, larger animals may be better models. For example, *TP53* knockout pigs were used as model of OS developed in the long bones and skull and closely replicated the human disease (Saalfrank et al., 2016).

The number of animals used in research has substantially increased over the years with the developments in medical technology. Millions of experimental animals are used all over the world every year. These constitute ethical concerns. The pain, distress, and death experienced by the test animals in experimental studies have been a controversial issue for a long time. Along with the major concern of ethics, there are some other, practical disadvantages of animal use in experiments such as need for skilled manpower, time consuming protocols and high cost. Various alternatives were proposed to overcome the drawbacks associated with animal experiments and avoid unethical procedures. *In vivo* models require consideration of several ethical and technical issues such as animal handling, housing, expensive experimental procedures, and following rigorously the international statutes and regulations. An approach of 3 Rs (Reduction, Refinement, and Replacement) is being followed in the laboratory use of animals. Different methods and alternative organisms are used to achieve this 3 Rs strategy (Doke and Dhawale, 2015).

1.6.2. Three-Dimensional Culture Systems

Although many studies on pathologies of bone metastatic tumors (breast, prostate, renal and lung), multiple myeloma (MM) and primary bone invasive tumors (osteosarcoma, oral cancer, and melanoma) are being conducted, tumor-induced bone diseases are still a clinical problem. A model that accurately mimics the complexity of the natural bone is missing and this slows down the progress of the therapy of bone cancer. Many researchers have developed 3D models to be able to do long term analysis of fundamental cell-cell and cell-matrix interactions in the complex cancer microenvironment (Villasante and Vunjak-Novakovic, 2015).

Some examples of 3D models use spheroids, some use cells or spheroids embedded in biomaterials or scaffolds, 3D matrix co-cultures and cell seeded microcarriers (Figure 1.6) (Imparato et al., 2015). 3D *in vitro* models of OS constitute a good alternative between the limitations of 2D *in vitro* models and the complexity of *in vivo* models.

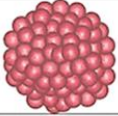
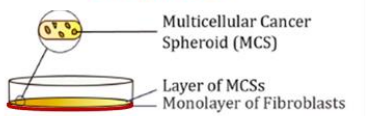
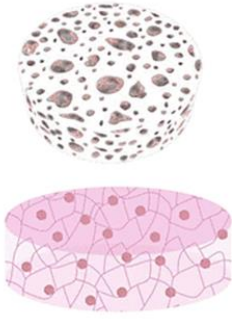
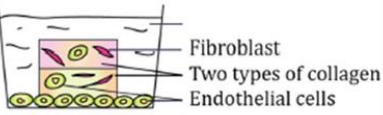
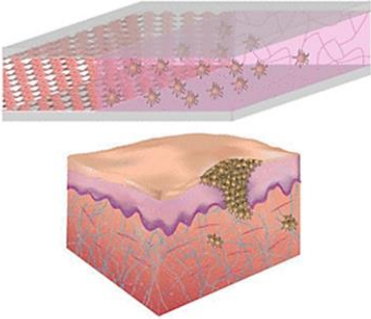
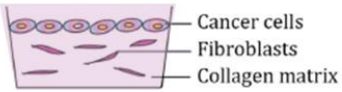
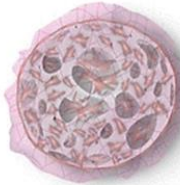
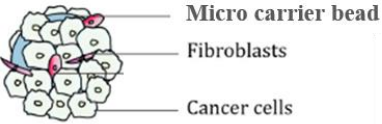
EXAMPLE	DESCRIPTION	EXAMPLES
	Spheroid	
	Cells or Spheroids embedded with various biomaterials/scaffold	
	3D matrix co-cultures to model cancer invasion	
	Cell-seeded microcarriers	

Figure 1.6. 3D *in vitro* cancer models that are designed to mimic *in vivo* tumor. Adapted from (Imparato et al., 2015; Kimlin et al., 2013).

1.6.2.1. Spheroids (Scaffold Free)

Spheroids are clusters of cells, generally 20–1000 μm in diameter. They have been widely used as a model system for anticancer drug screening, especially in high-throughput applications. Spheroids have been shown to mimic the physiological structure of the tumor, respond to chemotherapy and radiotherapy and preserve tissue-specific characteristics of the primary tissue (Zanoni et al., 2016). Moreover, tumor cells in spheroids have a much stronger cell-cell interaction and a different morphology than the cells in 2D monolayer culture. Cancer cells in 3D culture show a clustered, spheroid morphology that is similar to tumors *in vivo*. In 3D culture, the growth rate of tumor cells is similar to *in vivo* tumors. 2D cultured cells obtain excess nutrition and oxygen and proliferate faster than *in vivo* tumors but this is not true for the inner parts of the spheroids. The anticancer drug sensitivities of spheroids and 2D cultures are different and 3D cultures mimic *in vivo* drug delivery systems better than 2D cultures. The strong cell-cell interactions in 3D spheroids also increase the survival rates of the cancer cells when treated with anti-cancer agents which lead to the lower drug sensitivities of the 3D spheroid model unlike the 2D model. Screening with multi-cellular 3D spheroid cultures may eventually replace some animal tests (Charoen et al., 2014; Lama et al., 2013).

There are several techniques used in forming spheroids. Some are liquid overlaying, hanging drops, and microencapsulation on low attachment plates. In the liquid overlay method, cell attachment is prevented by using surfaces, which are covered with non-adherent materials, such as agar and agarose, or poly-hydroxyethyl methacrylate (HEMA), or by using commercially available low or ultralow adherent plates (De Luca et al., 2018). In a study, MG-63 (osteosarcoma cell line) spheroids were formed by liquid overlay technique, using plates coated with agar to study interaction between OS cells and the microenvironment and to assess the effects of hypoxia on attachment and spreading of MG-63. They found that hypoxia increased MG-63 spheroids adhesion on to plate (Indovina et al., 2008). In another study, OS 3D spheroids were developed by hanging drop method using Saos-2, HOS and MG-63 cell lines and cells

isolated from patient having osteoblastic and chondroblastic OS tissue (Rimann et al., 2014). The 3D microtissues were found to mimic the tissue heterogeneity of OS. Baek et al. formed 3D spheroids by culturing cells on special Corning® 96-well spheroid microplates. They used several 3D tumor cell spheroids including U2OS OS cell line in order to study the effect of doxorubicin (Baek et al., 2016) and cisplatin (Baek et al., 2016) on the cells. They showed that OS spheroids caused a reduction in permeability of drug. ECM of cell aggregates act as a barrier that prevents drug transport and increase drug IC₅₀ value in 3D by comparison with 2D models.

These techniques are time consuming and difficult to standardize since they generate spheroids with of non-uniform shapes and sizes due to the lack of control on the cell aggregation process (Arinzeh and Guiro, 2016). Although 3D spheroids mimic some properties of sarcoma *in vivo* (e.g. oxygen and drug diffusional gradients, cell-cell interaction, etc), non-attachment based culture model systems have poor control over the sarcoma structure and prevent cell adhesion on the surfaces (Fong et al., 2013).

1.6.2.2. Device-assisted Tumor Models

There are some models assisted by devices such as microfluidic systems or bioreactors.

1.6.2.2.1. Microfluidics

Microfluidic technology was used as a tool for biological analysis. It provides lots of advantages for analysis such as the ability to use very small quantities of reagents, doing experiments in a short period of time, high sensitivity and high resolution. These promising properties make microfluidics an alternative tool to study tumor progression, invasion, and angiogenesis (Xu et al., 2014). Microfluidics can become an innovative assay that offers accurate chemical, physical, and mechanical stimuli control over the cellular microenvironment. Moreover, these assays are very useful in clinical applications since they provide high throughput and automated drug screening (Arinzeh and Guiro, 2016).

Like spheroid cultures, several 3D models have been developed by using microfluidic devices to study initiation and progression of metastasis. Jeong et al. developed a microfluidic chip that combines HT-29 human colorectal carcinoma cell spheroids with cancer associated fibroblast (CAF) in proximity, providing bilateral interaction as *in vivo* tumor microenvironment. The 3D interaction between these two cell types was demonstrated by growth rate, ECM expression, drug accumulation, and drug sensitivity in spheroid and by alpha-smooth muscle actin (α -SMA) expression, morphology changes and increased migration in fibroblasts. This model can be used as a tool for drug testing (Jeong et al., 2016).

1.6.2.2.2. Tissue Engineering Bioreactors

The accurate development of cellular architecture and the microenvironment are essential in order to increase the reliability of an *in vitro* tumor model. This contains not only the creation of 3D cellular structure and the existence of ECM components and nutrients but also the maintenance at physiological levels of physicochemical environmental parameters known to affect drug response, such as temperature, pH, and oxygen, which could be regulated through use of bioreactors (Hickman et al., 2014). Some bioreactor types such as classical stirred culture vessels, rotary cell culture systems (RCCS) and last-generation microfluidic devices with potential application on cancer *in vitro* models are widely used. In a study, bioreactors are used in the culture of myeloma explants under dynamic flow conditions, using rotating vessels. These bioreactors both maintained tumor explants over long culture times and maintained the architecture of skin, blood and vessels, bone and bone marrow microenvironments. This study demonstrated that bioreactor cultures of tissue explants can be used for studying cancer biology, drug testing, and the development of patient targeted therapeutic approach (Ferrarini et al., 2013).

1.6.2.3. Matrix-assisted Tumor Models (with Scaffold)

The use of 3D cell culture model with scaffold enables the researchers to adjust chemical composition, shape, structure, porosity, and stiffness of the 3D construct and these have an important effect on cell-cell interaction and proliferative and migratory abilities of tumor cells.

Many aspects of the cell-ECM interactions have significant influence on cell-matrix interaction, mechanotransduction, cell shape and polarity, morphogenesis, matrix degradation and motility. Many of these factors are pathologically changed in tumor ECM especially the concentration and organization of ECM mechanical determinants and factors influencing matrix metastasis, making their modeling in 3D matrices of even greater importance (Gill and West, 2014).

Within tumor microenvironment, there are some criteria that should be met to show the accuracy of generated tumor model such as, the pre-vascularization at the initial stages of solid tumor growth, uncontrolled proliferative capacity, formations of regions of hypoxia surrounding a necrotic core and activation of genetic factors that result in the recruitment of local endothelial cells for angiogenesis (Godugu et al., 2013).

Biomimetic 3D tissue-engineered systems have been developed for many diseases. Meanwhile, 3D bone models which have similar complex structure of bone has also been developed. When generating a 3D model of bone and cancer, many parameters such as the strength, pore size, mineral composition, and fluid flow need to be taken into consideration because they are considerably different in the bone than any other tissue in the body. (Figure 1.7). For example, matrix rigidity affects cancer cell invasion, metastasis, and tissue tropism. The high rigidity influences stem cell differentiation and increases osteoblast differentiation and mineralization (Villasante and Vunjak-Novakovic, 2015).

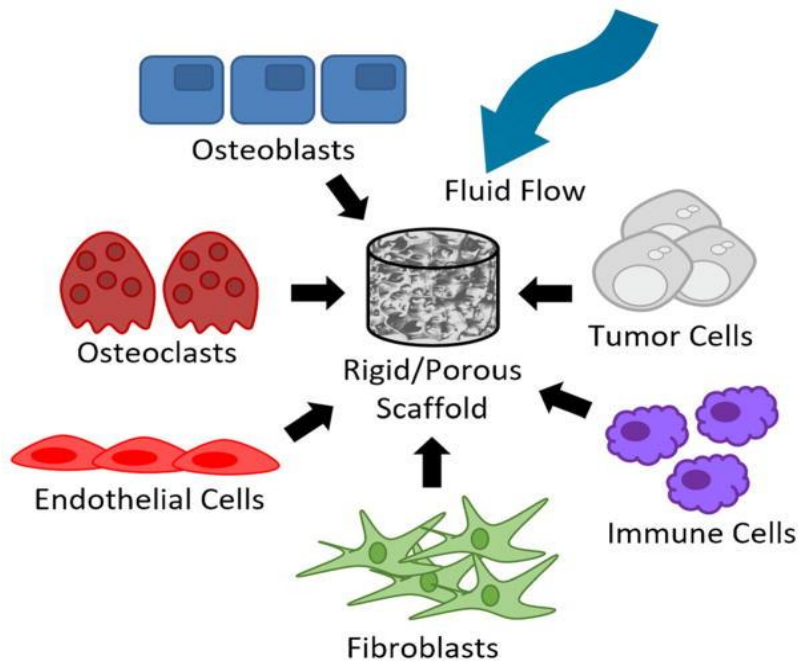


Figure 1.7. The physical and cellular components in 3D bone tumor models (Kwakwa et al., 2017).

As long as researchers continue to study bone microenvironment, models will include not only physical factors but also different cell types (Kwakwa et al., 2017). In conclusion, it is important to develop biomimetic tumor models that involve the primary components required for the precise mimicking of *in vivo* conditions that are not exceedingly complex and, therefore will not lead to complex data analysis (Schuessler et al., 2014).

In the following section, various types of matrices and components that have been used to develop 3D bone tumor models will be summarized.

1.6.2.3.1. Natural Matrix

Natural materials such as collagen, chitosan, cellulose, silk, alginate, hyaluronic acid, and chondroitin sulfate are different types of polymers used to produce scaffolds in the form of hydrogels and sponges to act as the supportive material of the tumor models.

Hydrogels

Hydrogels are hydrophilic polymer networks that closely mimic features of soft tissues in terms of their viscoelastic properties. Hydrogels are the most commonly used materials because of their capacity to offer controllable microenvironments for modeling cell-cell and cell-ECM interactions. In the development of tumor models, the ability to control the physiochemical and biological properties of the hydrogels, such as the introduction of cell adhesion ligands and enzymatically-degradable sites, matrix stiffness, and 3D topography is an advantage. Natural materials inherently improve tumor growth and angiogenesis since they support cell interaction properties, adhesion, and signaling, and they are also biodegradable. The most common sources of natural hydrogels are collagen and fibrinogen (Cox et al., 2015).

Type I collagen, the most abundant protein in the native ECM, is also a popular material because of its ability to offer a bioactive microenvironment including cell adhesion ligands and proteolytically-degradable sites that are critical for ECM remodeling. *Fibrinogen* is a large glycoprotein found in plasma, and it is generally used due to its inherent nano/macro fibrous structure mimicking native ECM and its controllable mechanical properties, which are critical to investigate the role of matrix stiffness on tumor progression and response to therapeutics. The main disadvantages of using natural hydrogels are limitation of changing matrix stiffness and cell adhesion moieties density independently, a narrow range of physical properties and batch-to-batch differences (Imparato et al., 2015).

Common examples of natural hybrid hydrogels are modified hyaluronic acid (HA) and peptide-modified alginate. HA is an important ECM molecule for tumor progression and invasiveness. In bone cancer model, co-culture of prostate cancer cells and osteoblast in a hydrogel were used to investigate prostate cancer metastasis in bone. Compressive modulus of hydrogels was 9.3 kPa when crosslinked with genipin. This value does not match with bone material properties and may affect the tumor cell behavior that does not mimic native bone microenvironment (Fong et al., 2016).

Fallica et al. (2012) studied the response of OS cells embedded in 3D collagen gel and studied the change in the cell response to Phosphatide Inositol-3 Kinase (PI3K) pathway inhibition which is a critical intracellular signaling cascade influencing cell growth, migration, protein expression, and survival, and was found as a possible target for new anti-cancer drugs for many cancer types. The authors tested a drug that has interacts with PI3K and found that it was effective to U2OS cell line in a 3D collagen matrix to change the activation of PI3K/Akt pathway. Higher concentration of collagen I showed a more resistant population of U2OS cells. This study showed that materials mimicking the ECM properties are very important in mimicking tumor (Fallica et al., 2012).

Elenjord et al. developed *in vitro* 3D fibrillar and 2D monomeric OS models to study the effect of cell-collagen I interactions on the synthesis and activation of matrix metalloproteinase-2 (MMP-2). MMP-2 is primary MMP enzyme which has a role in ECM remodeling, and its uncontrolled activity causes cancer. The culture of OS cells on two different forms of collagen I hydrogel had contrasting effects on cellular synthesis and activation of MMP-2. Results highlighted that the architecture of the matrix components had a significant effect on enhancing invasion and metastatic process of cancer of OS cells (Elenjord et al., 2009).

Sponges

Scaffolds in sponge form are stronger and more stable than highly hydrated hydrogel scaffolds and can be prepared by using more than one material. Their advantages are; they provide a high surface area for cell attachment and have good mechanical properties that allow longtime culture. In addition, they contain large pore sizes in comparison to hydrogels. All these features make sponges good matrices for cancer cell culture microenvironment (Sitarski et al., 2018).

Tan et al. prepared a porous silk sponge scaffold to study the difference in secretion profiles of OS cells cultured in 2D and 3D OS models. The expression level of hypoxia-inducible factors (HIF)-1 α , VEGF-A, basic fibroblast growth factor (bFGF), and interleukin (IL-8) of cells cultured in 3D mimicked that of in mouse xenograft tumor models. They concluded that it may be the results of the hypoxia generated within the 3D structure of porous silk scaffolds that is similar to *in vivo* model (Tan et al., 2011). These findings together with the results of other study (Tan et al., 2016) showed that silk itself does not lead to variations in tumor biology, instead 3D architecture of silk sponge causes the changes in drug resistance and cell proliferation. Silk fibroin is a natural polymer that shows good biocompatibility, high oxygen and water permeability, slow degradability, good cell adhesion and growth. Recently, tests with silk scaffolds showed an increased in the invasiveness of breast adenocarcinoma MDA-MB-231 cells (Talukdar et al., 2011) and enhanced development of a prostate cancer metastasis to bone model (Kwon et al., 2010) highlighting the applicability of silk scaffolds in the production of biomimetic tumor material.

Chitosan is the hydrolyzed form of the polysaccharide chitin and is used in the preparation of 3D porous scaffold for cancer research (Graciano et al., 2015) as well as scaffold in tissue engineering applications. It is a suitable material for bone tissue engineering due to its biocompatibility, biodegradability, and osteoinductive features, and besides it structurally mimics the glycosaminoglycans (Pattnaik et al., 2011). It was found that chitosan is non-toxic to osteoblast cells and chondrosarcoma cells *in vitro* (Tan et al., 2014).

1.6.2.3.2. Synthetic Matrix

Synthetic hydrogels and scaffolds have been developed to serve as a 3D matrix in tissue engineering applications to mimic the critical properties of the native ECM environment. There are several advantages of these systems such as allowing incorporation of specific cell attachment motifs and ECM proteins, controllable mechanical properties to match cellular requirements, enabling preparation of

complex geometric shapes, reproducible sourcing, production and manufacturing, ease in sterilization and adaptable to high throughput screening capabilities (Imparato et al., 2015). Although synthetic polymer scaffolds have these advantages, they are less hydrophilic and less biocompatible than natural materials, which have good cell adhesion and proliferation (Llorens et al., 2015). In addition, they generally have a slow degradation rate (PCL) and low mechanical properties (PLGA) (Guelcher, 2008).

Different types of poly(α -esters) have been widely used as synthetic polymers in bone tissue engineering and for tumor models involving poly(caprolactone) (PCL), poly(lactic acid) (PLA), and poly(lactic acid-co-glycolic acid) (PLGA). These are biocompatible and biodegradable polymers also used in other biomaterial applications such as coatings on metallic implants and drug delivery systems. They can also be mixed with hydroxyapatite (HAp) and other ceramics to develop composite materials that have the desired bone-like features (Zhang et al., 2011).

Polyester scaffolds have been used to investigate growth, morphology, and chemotherapy response to many cancer models consisting of the breast (Sahoo et al., 2005), osteosarcoma (Chen et al., 2003) and glioblastoma multiforme (Ma et al., 2012). Porous PLG scaffolds have been used to develop oral squamous cell carcinoma model to investigate metastasis-related signaling like *in vivo*-mimetic angiogenic signaling. In the interior of 3D PLGA tumor model, the oxygen concentration decreased over time to a level of hypoxia resembling that of tumors *in vivo* and induced the secretion of the angiogenic factors VEGF, IL-8 and bFGF (Fischbach et al., 2007). PLGA scaffolds formed with the bone mineral hydroxyapatite were used to study inflammatory and signaling changes in bone metastatic breast cancer (Pathi et al., 2010). In a study, the polyester poly(ϵ -caprolactone) (PCL) was used to develop an electrospun scaffold. The 3D culture of Ewing's sarcoma cells on electrospun PCL scaffolds more closely simulated human tumors in comparison to those cultured in 2D monolayer in terms of growth, expression patterns of important therapeutic-targeted signaling pathways (Fong et al., 2013).

1.7. Approach, Aim, and Novelty of the Study

In this thesis, a 3D bone tumor model (BTM) was developed by using tissue engineering approach and the efficacy of the anticancer drug was tested on this model. There were two primary components of the BTM. One of them was a cylindrical healthy bone mimic that mainly represents bone tissue microenvironment. And the second part of the BTM was a tumor mimic that was placed in the cavity of healthy bone mimic (Figure 1.8). Lyophilized, 3D, biodegradable, porous poly(lactic acid-co-glycolic acid) (PLGA)/beta-tricalcium phosphate (β -TCP) scaffolds were produced to mimic the healthy bone mimic. Human fetal osteoblastic cells (hFOB) and human umbilical vein endothelial cells (HUVEC) were co-cultured in a 1:1 ratio on these scaffolds to generate the healthy bone mimic. Lyophilized, biodegradable, 3D, porous collagen scaffolds were produced to act as ECM of the solid bone tumor. Human osteosarcoma cells (Saos-2) were cultured on collagen scaffolds to create tumor mimic. After the proliferation period, the collagen scaffolds cultured with Saos-2 cells were inserted into the cylindrical cavity in the PLGA/TCP scaffold which was previously cultured with hFOB and HUVEC. In this way, the osteosarcoma model that is being proposed consists of healthy bone tissue mimic with an embedded tumor tissue mimic inside was produced.

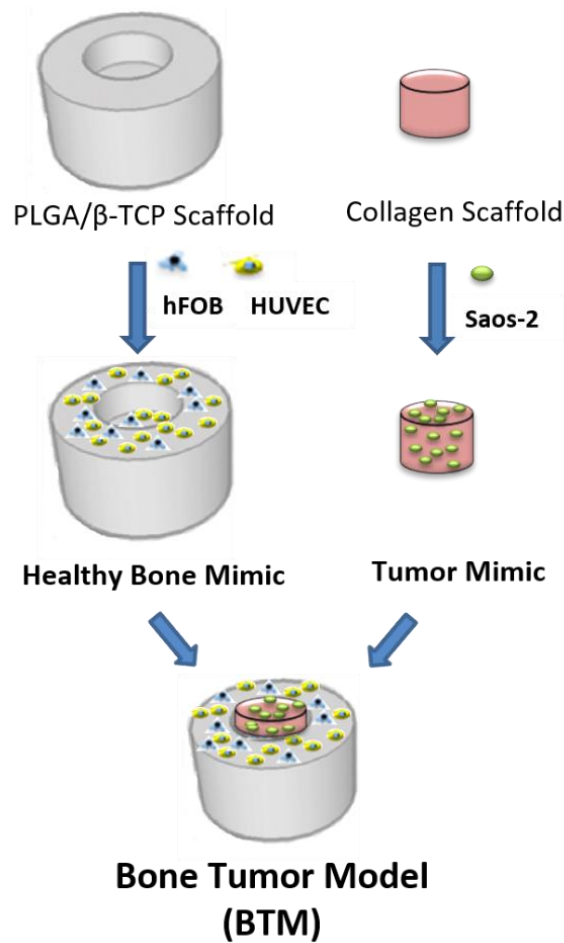


Figure 1.8. Development of bone tumor model.

PLGA/TCP scaffold was prepared as a matrix material of healthy bone mimic with freeze drying method. While PLGA was used to act as an organic part, and β -TCP was as inorganic component of the bone structure. PLGA is a FDA approved synthetic polymer, commonly used for *in vitro* and *in vivo* bone tissue engineering studies due to its mechanical properties, biocompatibility and controllable biodegradability rate that can be adjusted with co-polymer ratios (Doğan et al., 2014). PLGA (82:18) was chosen since it has low degradation rate and it is stable. β -TCP that is a bioactive ceramic, is commonly used for bone regeneration, and it is known to promote primary biological responses such as osteoconduction at the cell-material interface (Kim et al.,

2015). PLGA/ β -TCP scaffolds were used in many studies and demonstrated good cell interaction and osteoconductivity (Pang et al., 2007), enhancement in the bone regeneration of critical bone defects (Lin and Gao, 2016), better guidance in the culture of osteoblasts (Yang et al., 2011) and improvement in biological activity, such as calcium deposition (Kim et al., 2015). Because of all these, β -TCP containing PLGA scaffolds were chosen as the healthy component of the model.

As the tumor matrix, collagen scaffolds were produced by freeze drying. Collagen constitutes 95% of the organic part of the bone matrix. It is also widely used biomaterial for 3D modeling due to its biocompatibility, biodegradability, crosslinking capacity (Fitzgerald et al., 2015).

Three different types of bone tumor models were prepared in this study. The main model was consisting of Saos-2 cells seeded collagen scaffolds inserted in the cavity of PLGA/TCP scaffolds co-cultured with hFOB and HUVECs and acting as healthy bone mimic. This model was used to test the efficacy of the drug.

The other two models containing Saos-2 spheroids seeded on collagen scaffolds or embedded in methacrylated gelatin (GelMA) hydrogels were also inserted in the healthy bone mimic to check reproducibility of the systems.

2D cell culture, then animal models, and finally clinical trials in patients are the traditional stages of developing and testing new therapeutic agents. Using 3D cell culture models permit scientists to eliminate less reliable 2D models, reduce large-scale and expensive animal models, escape false positive findings, and advance clinical research by screening promising anticancer agents more rapidly. Moreover, tissue engineered models have started to bridge the gap between 2D *in vitro* cultures (used for discovery and screening) and *in vivo* animal models (used for efficacy and safety assessment before passing to clinical trials) by providing a predictive, inexpensive, rapid, 3D, *in vitro* alternative. The main novelty of this 3D bone tumor model is the coexistence of both a microenvironment mimicking bone and tumor tissue. Cancer is a complex disease where interactions between tumor cells and healthy

bone cells play an important role in carcinogenesis and metastasis. In the present study, we have taken a step forward in modeling the bone tumor by incorporating osteosarcoma cell seeded collagen constructs (serve as tumor mimic) into a tissue engineered bone stroma, and thus enabling multiple interactions of tumor cells with other tumor cells, bone tissue matrix and bone and endothelial cells.

CHAPTER 2

MATERIALS AND METHODS

2.1. Materials

PLGA 82:18 was purchased from Corbion (USA). Porcine skin gelatin type A (100 bloom), beta-tricalcium phosphate (β -TCP), 4',6-diamine-2-phenylindole dihydrochloride (DAPI), , bovine serum albumin (BSA), type II collagenase (from *C. histolyticum*) methacrylic anhydride, paraformaldehyde (37% w/v), sodium azide (ReagentPlus®, $\geq 99.5\%$), Piperazine-N,N'-bis(2-ethanesulfonic acid) (PIPES), 100 U/mL penicillin and 100 μ g/mL streptomycin, Irgacure 2959, and Costar® 6 well clear flat bottom ultra-low attachment multiple well plates were purchased from Sigma-Aldrich (USA).

Triton X-100 was purchased from AppliChem (USA). PCR primer was synthesized at Sentegen (Turkey). Mc Coy's 5A and EGM-2 BulletKit were purchased from Lonza (USA). DMEM/F12 colorless medium was purchased from Gibco (USA). Human bone osteosarcoma cell line Saos-2 (ATCC® HTB-85™) and osteoblast cell line hFOB 1.19 (ATCC® CRL-11372™) were purchased from ATCC (UK). Human umbilical vein endothelial cells (HUVEC) was purchased from Lonza (USA). Fetal bovine serum (FBS), Trypsin EDTA Solution B (0.25%) and C (0.05%) were purchased from Biological Industries (Israel).

Total DNA quantification kit PicoGreen dsDNA assay, DRAQ5, Alexa Fluor 532 goat anti-mouse IgG, Alexa Fluor 647 goat anti-rabbit IgG, Alexa Fluor 647 goat anti-rabbit IgG, Alexa Fluor 488 Phalloidin, and Alexa Fluor 532 Phalloidin were purchased from Invitrogen (USA). Caspase-3 assay kit, anti-TNF alpha antibody, anti-Von Willebrand Factor antibody and Alexa Fluor 594 donkey anti-sheep IgG were purchased from Abcam (USA).

Alexa Fluor 488 anti-mouse CD31 Antibody was purchased from BioLegend (USA), and SensoLyte[®] pNPP alkaline phosphatase assay kit was purchased from Anaspec (Belgium). SnakeSkin pleated dialysis tubing, AlamarBlue[®] cell viability assay kit and LIVE/DEAD[™] cell viability/cytotoxicity kit for mammalian cells were purchased from Thermo Fischer Scientific (USA). TO-PRO[™]-3 Iodide was from Cell Signaling Technology (USA).

Sprague-Dawley rat tails were kindly provided by Experimental Animal Production and Research Center at Başkent University (Turkey).

2.2. Methods

2.2.1. Preparation of Sponges

In this study, two different sponge types were prepared.

2.2.1.1. Preparation of PLGA/TCP Sponges

In the preparation of PLGA/TCP sponges, Teflon molds consisting two parts which interlock each other were used. They were designed by using the SketchUp program and produced at METU CAD/CAM Center. One of part is a hollow cylinder that has 5 mm wall thickness and the other one is a cylinder with a pit (5 mm diameterx4 mm height) inside to create a cavity in the sponge. Porous PLGA/TCP sponges were prepared by combining freeze drying and salt leaching methods (Hasirci et al., 2016). In the preparation of sponges, PLGA 82:18 (Corbion, USA) was dissolved in 1,4-dioxane at a concentration of 10 % w/v. β -TCP (Sigma, Germany) was added in PLGA solution at a concentration of 2.5 % w/v. Sodium chloride (NaCl) particles (diameter range 150-250 μ m) was added to PLGA/TCP suspension having weight ratios of PLGA+TCP to NaCl particles in a ratio of 1:4 and 1:8. The mixture was transferred into a Teflon mold, frozen at -80 °C and lyophilized. After leaching the salt in distilled water for 2 d, sponges were dried. Finally, cylindrical PLGA/TCP sponges (10 mm diameter \times 6 mm height) with a cavity (5 mm diameter \times 4 mm depth) were obtained (Figure 2.1).

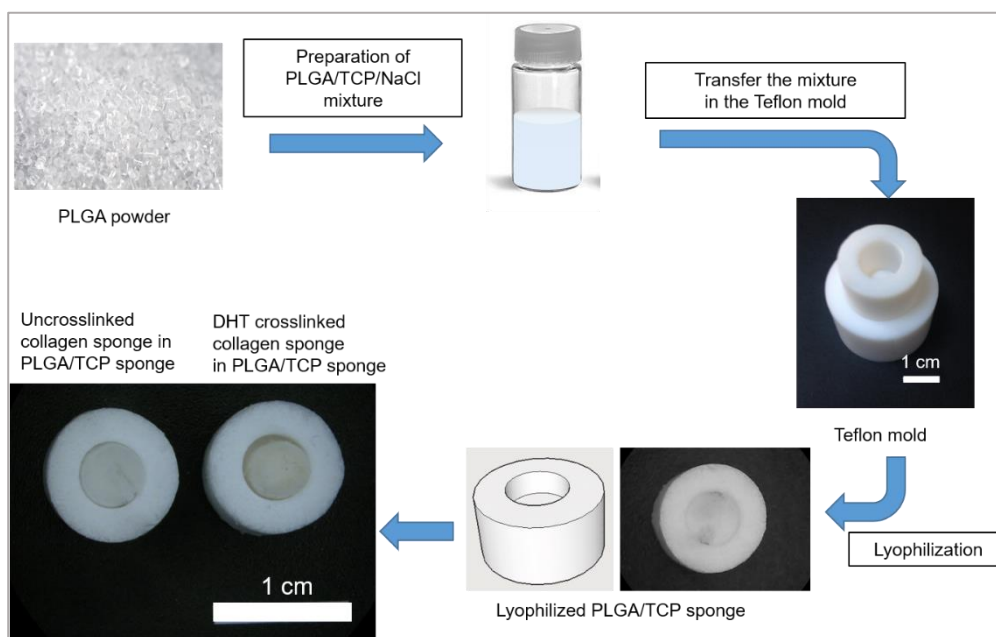


Figure 2.1. Preparation of PLGA/TCP sponge.

2.2.1.2. Preparation of Collagen Sponges

Isolation of Collagen from Rat Tail. Collagen type I was isolated from Sprague-Dawley rat tails as described previously (Kilic et al., 2014; Komez et al., 2016). Briefly, tendons were dissolved in acetic acid (0.5 M) at 4 °C for 2-3 days. The suspension was filtered through glass wool, dialyzed against phosphate buffer (24 mM, pH 7.2), and centrifuged (Sigma 3K30, Germany) (16,000 g, 10 min) at 4°C. The collagen pellet obtained was dissolved in acetic acid (0.15 M), precipitated with NaCl solution (5% w/v), and dialysis and centrifugation steps were repeated 2 times. Collagen precipitate was obtained by centrifugation and sterilized in ethanol (70%), frozen and lyophilized (Labconco Freezone 6, USA). In order to make the sponges, collagen solution (1.5 % w/v in 0.5 M acetic acid) was prepared, put in the molds, frozen at -20°C and lyophilized. Then, same sponges were dehydrothermally crosslinked by heating at 140 °C in a vacuum oven for 24 h. The uncrosslinked and dehydrothermally crosslinked collagen sponges are abbreviated as UXL-CS and DHT-CS, respectively (Figure 2.2).

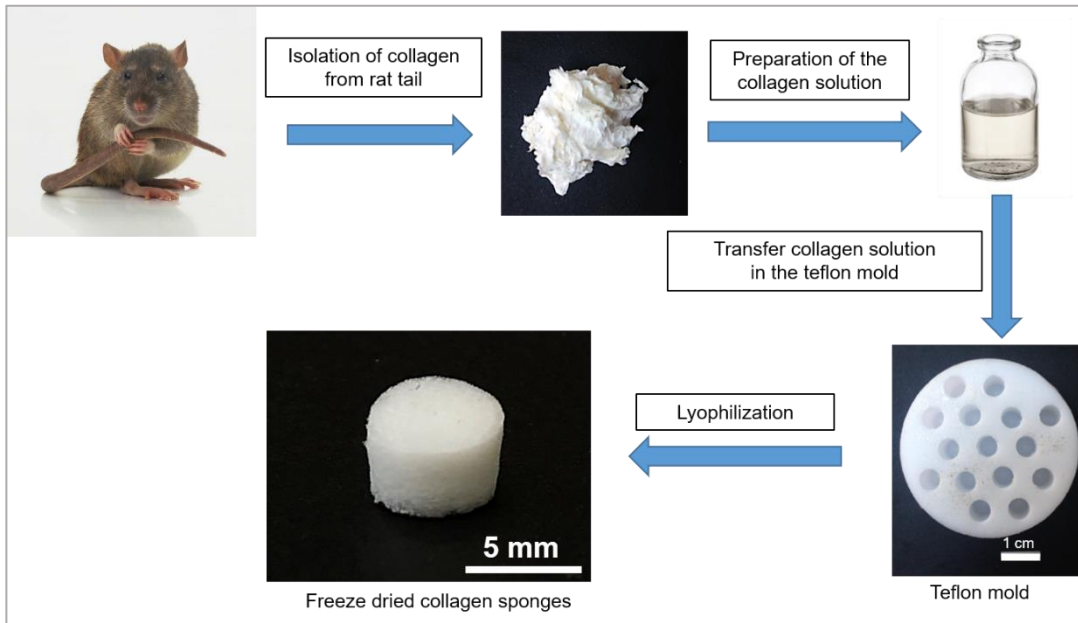


Figure 2.2. Preparation of collagen sponge.

2.2.2. Characterization of Sponges

2.2.2.1. Contact Angle Measurement

The water contact angle of the sponges was measured by the static sessile drop method using a contact angle goniometer (One Attention, Biolin Scientific, Finland). Distilled water (7 μL) was placed at 5 different locations on the sponges and contact angles were measured by processing these images with the software of the system.

2.2.2.2. Degradation Test

Degradation test of PLGA/TCP sponges was conducted in sterile phosphate buffer saline (PBS) (0.01 M, pH 7.4) containing sodium azide (0.5 mg/mL) at 37 $^{\circ}\text{C}$. PBS was replaced at every time point. At each time point, sponges were removed, washed with distilled water, lyophilized and weighed. Weight loss was calculated as shown below;

$$\text{Weight loss (\%)} = \frac{W_0 - W_1}{W_0} \times 100 \quad (1)$$

where W_0 is the dry weight of the sample before the degradation test and W_1 is the dry weight of the sample after the degradation test.

Degradation test of collagen sponges was conducted in collagenase Type II solution (0.1 mg/mL in PBS, pH 7.4) for 2 h and 4 h. Loss of weight was calculated by using the Equation 1.

2.2.2.3. Compressive Mechanical Test

Compressive mechanical test was performed on cylindrical shaped PLGA/TCP sponges and collagen sponges ($n \geq 5$) in the axial direction using a universal test machine (Shimadzu AGS-X, Japan, 5 kN load cell) at room temperature (RT). The compression test was carried out with application of displacement (compression) rate of 0.5 mm/min.

2.2.2.4. Scanning Electron Microscopy (SEM)

The PLGA/TCP and collagen sponges were placed on carbon tapes attached to SEM stubs, and coated with Au–Pd in a sputter coater. SEM images were obtained at 10-20 kV. Sponge topography was examined with SEM (QUANTA 400F Field Emission SEM, Netherland) at the Central Laboratory (METU).

2.2.2.5. Micro Computed Tomography (MicroCT) Analysis

PLGA/TCP and collagen sponges were scanned to reveal the inner structure using microcomputed tomography (microCT) (Bruker microCT, SkyScan 1172, Belgium). PLGA/TCP sponges were scanned using 100 kV and 100 mA power with Al 0.5 mm filter. The pixel size was adjusted to 6 μm and exposure time was 600 ms. Samples were scanned by rotating 360° with a rotation step of 0.4°. Collagen sponges were scanned with MicroCT using 35 kV and 21 mA power and the pixel size was adjusted to 6 μm and exposure time was 150 ms. Reconstruction was obtained with application of standard software NRecon. Porosity was determined with CTAn software (Bruker microCT). In addition, the collagen sponge was scanned with High-Resolution 3D X-ray Imaging System (XRadia, Micro XCT-400, USA).

2.2.3. Preparation of Healthy Bone and Tumor Mimics

Human umbilical vein endothelial cells (HUVEC) (C2517A Lonza, USA) were cultured in EGM-2 BulletKit (Lonza, USA) containing basal medium and SingleQuots™ Kit at 37 °C in a 5% CO₂ incubator. A human fetal osteoblast cell line (hFOB) (ATCC, UK) was cultured in DMEM/F12 colorless medium (Gibco, USA) supplemented with fetal bovine serum (FBS) (10%) and G418 (0.3 mg/mL) (Sigma, USA) at 34 °C in a 5% CO₂ incubator. Homo sapiens bone osteosarcoma cell line (Saos-2) (ATCC, UK) were cultured in McCoy's 5A medium (Lonza, USA) supplemented with FBS (15%) and penicillin/streptomycin (100 U/mL) (Sigma, USA) at 37 °C in a 5% CO₂ incubator.

PLGA/TCP scaffolds were treated with oxygen plasma (100 W, 3 min) and they were sterilized with UV (30 min for each side) prior to addition of cells. HUVEC were detached with trypsin-EDTA solution C and hFOB were detached with trypsin-EDTA solution B and cells were collected by centrifugation. HUVEC and hFOB cells were seeded on the PLGA/TCP scaffolds at a ratio of 1:1 (2×10^5 cells/scaffold) and incubated in DMEM/F12:EGM-2 medium (1:1) at 37 °C to produce healthy bone mimic (Figure 2.3A). During *in vitro* studies, growth media were refreshed every other day.

DHT crosslinked collagen scaffolds were treated with oxygen plasma (100 W, 5 min) and sterilized with UV (30 min). Saos-2 were detached with trypsin-EDTA solution B, cells were collected by centrifugation, seeded (1×10^5 /scaffold) on collagen scaffolds and incubated in McCoy's 5A medium at 37 °C in a CO₂ incubator to generate tumor mimic (Figure 2.3B). During *in vitro* studies, growth media was refreshed every other day.

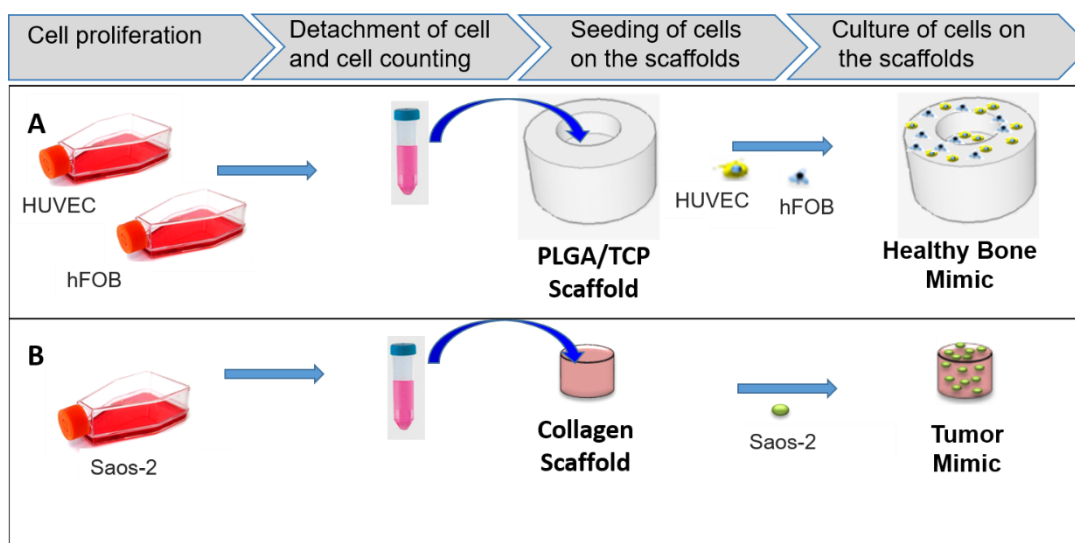


Figure 2.3. Preparation of the (A) healthy bone mimic, and (B) tumor mimic.

2.2.4. Characterization of Healthy Bone and Tumor Mimics

2.2.4.1. Alamar Blue Cell Viability Assay

Cell proliferation and metabolic activity on scaffolds was determined by Alamar Blue cell viability assay (Invitrogen, USA). Live cells convert non-fluorescence resazurin into fluorescent resorufin (Figure 2.4). With this method, the resazurin in the Alamar Blue dye is reduced by mitochondrial enzymes in the cells and the color change is measured spectrophotometrically and the number of cells is determined using a calibration curve (Borra et al., 2009).

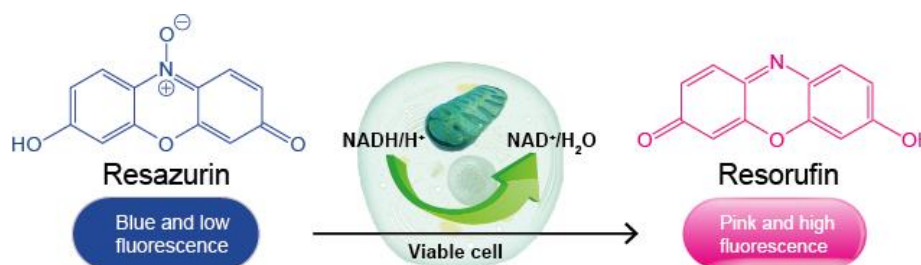


Figure 2.4. Principle of Alamar Blue cell viability assay.

The cell viability assay was performed for hFOB/HUVEC co-cultured on PLGA/TCP scaffolds and Saos-2 cultured on collagen scaffolds. Cell seeded and unseeded scaffolds were washed with PBS twice and incubated with 10% Alamar Blue solution in colorless DMEM for 1 h at 37 °C and 5% CO₂ condition. After incubation, the Alamar Blue solution (200 μL) was transferred into 96 well plates and the absorbance of the solution was measured at both 570 nm (λ_1) and 595 nm (λ_2) with a plate reader (Molecular Devices, USA). The absorbances were converted to 'percent reduction values by using the following equation:

$$\text{Reduction (\%)} = \frac{((\epsilon_{\text{ox}})_{\lambda_2} \times A_{\lambda_1}) - ((\epsilon_{\text{ox}})_{\lambda_1} \times A_{\lambda_2})}{((\epsilon_{\text{red}})_{\lambda_1} \times A'_{\lambda_2}) - ((\epsilon_{\text{red}})_{\lambda_2} \times A'_{\lambda_1})} \times 100 \quad (2)$$

where,

$\lambda_1 = 570$ nm

$\lambda_2 = 595$ nm

A_{λ_1} and A_{λ_2} = Absorbance of test well,

A'_{λ_1} and A'_{λ_2} = Absorbance of negative control well (blank)

Molar Extinction Coefficients

$(\epsilon_{\text{ox}})_{\lambda_2} = 117.216$ $(\epsilon_{\text{red}})_{\lambda_1} = 155.677$

$(\epsilon_{\text{ox}})_{\lambda_1} = 80.586$ $(\epsilon_{\text{red}})_{\lambda_2} = 14.652$

A calibration curve was constructed to convert the absorbance values to number of cells.

2.2.4.2. Alkaline Phosphatase (ALP) Activity

SensoLyte pNPP alkaline phosphatase assay kit was used to determine ALP activity of hFOB cell. P-nitrophenyl phosphate (pNPP) is a chromogenic substrate and after dephosphorylation, absorption maximum is at 405 nm. The kit manual was used for ALP assay. Briefly, cell seeded and cell-free scaffolds were washed with component

B. Lysis buffer (500 μ L) was added on the samples that were cut with a lancet. Cells cultured on TCPS culture plates were used as a positive control. Samples were frozen and thawed three times at -80 °C and 37 °C, respectively. Then, sonication was applied at 50 W 30 s and contents were centrifuged at 2000 rpm for 10 min. The supernatant (50 μ L), ALP dilution buffer (50 μ L) and Component A (50 μ L) were added to 96 well plates, incubated for 1 h at 37 °C, 50 μ L stop solution was transferred to each well and absorbance was measured at 405 nm by a plate reader. ALP concentration was calculated by using the calibration curve.

2.2.4.3. Immunocytochemistry

Cell seeded PLGA/TCP and collagen scaffolds were fixed with paraformaldehyde (4%) for 15 min at RT, treated with Triton-X-100 (1%) for 5 min at RT to permeabilize cell membrane and incubated in 1% BSA block solution at 37 °C to prevent nonspecific binding. Samples were incubated in Alexa Fluor 532-Phalloidin for 1 h at 37 °C and DRAQ5 for 15 min at RT. Samples were examined with a confocal laser scanning microscope (CLSM) (Leica DM2500, Germany).

Cell seeded samples were sectioned with cryomicrotome into 20-30 μ m thick slices, transferred to Polysine™ Microscope Adhesion Slides. Sections were incubated in Triton X-100, blocked in the 1% BSA solution, stained with Alexa Fluor 488 tagged anti-human CD31, Alexa Fluor 532-Phalloidin, and DRAQ5. Samples were examined with a CLSM.

2.2.4.4. SEM

Cell seeded scaffolds were washed twice with PIPES (piperazine-N, N'-bis(ethanesulfonic acid)) buffer and fixed with paraformaldehyde solution (4%) for 5 min and lyophilized. Samples were coated with gold-palladium (Au-Pd) under vacuum and examined with SEM (FEI Quanta 200F, USA).

2.2.4.5. MicroCT Analysis

Porosity analyzes were achieved with MicroCT. 1000 horizontal sections were investigated on PLGA/TCP scaffolds and CTAn software was used on the gray scale between 45 and 255. Collagen scaffolds were investigated in 200 sections in horizontal sections and CTAn software was conducted on the gray scale between 80 and 255.

2.2.5. Development of 3D Bone Tumor Model (BTM)

In this study, three different types of bone tumor models were prepared. In all models, as the healthy bone component, PLGA/TCP scaffolds co-cultured with hFOB and HUVECs were used. Tumor mimics were prepared in three different forms: (1) Saos-2 cell seeded in collagen scaffolds; BTM-S, (2) Saos-2 spheroids seeded in collagen scaffolds; BTM-SS, (3) Saos-2 spheroids embedded in methacrylated gelatin (GelMA); BTM-G. These 3 tumor mimics were inserted separately in the cavity of healthy bone mimic.

2.2.5.1. Development of Model in Collagen Scaffolds (BTM-S)

hFOB/HUVEC cells were co-cultured on PLGA/TCP scaffolds and Saos-2 cells were cultured on collagen scaffolds for 2 d as described in Section 2.2.3. Tumor mimic was placed in the cylindrical cavity of the bone mimic, and this bicomponent structure was cultured in EGM-2:DMEM/F12:McCoy's 5A (1:1:1) medium to develop BTM-S (Figure 2.5).

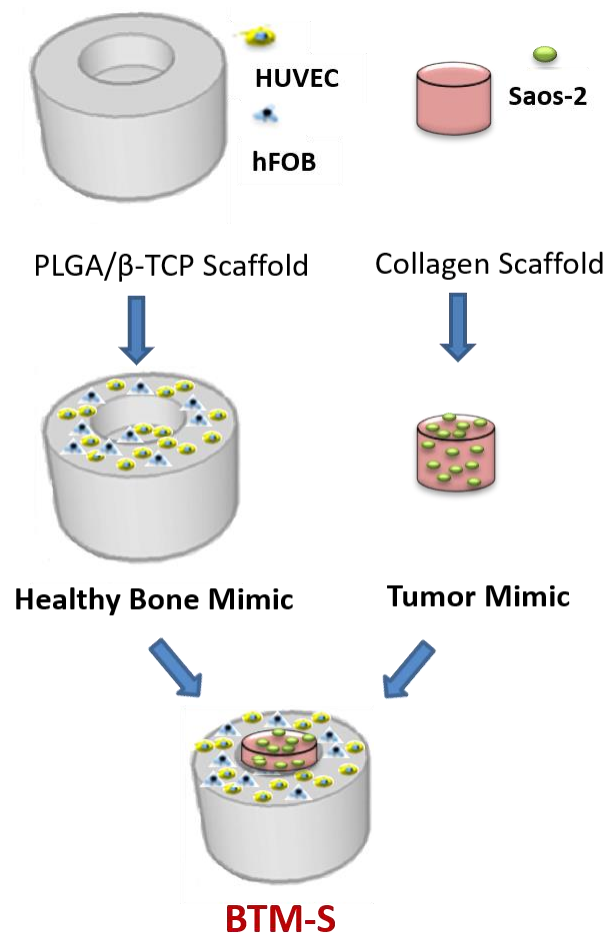


Figure 2.5. Preparation of BTM-S.

2.2.5.2. Development of Scaffolds with the Spheroids (BTM-SS)

In the preparation of BTM-SS, first step was the preparation of Saos-2 spheroids.

2.2.5.2.1. Preparation of Saos-2 Spheroids

To produce spheroids, Saos-2 cells were cultured on the Corning® Costar® ultra-low attachment 6-well plate (Sigma Aldrich, Germany) in McCoy's 5A medium. In this process, cells could not attach the plate surface and form cluster. Eventually, these clusters grow and form the spheroids (Figure 2.6).

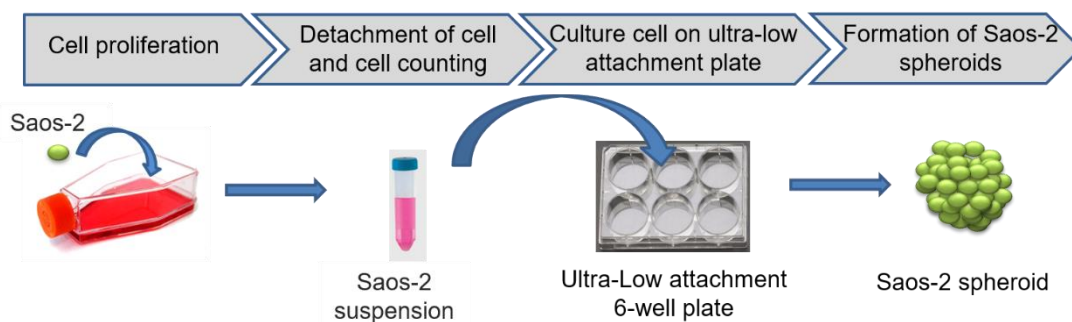


Figure 2.6. Preparation of Saos-2 spheroid.

Development of BTM-SS. The spheroids were grown for 10 days before seeding on collagen scaffolds. Meanwhile, hFOB/HUVEC cells were co-cultured on PLGA/TCP scaffolds as described in Section 2.2.3 and collagen scaffolds were placed in the cylindrical cavity of the bone mimic. Spheroids (3 or 4) were seeded on these collagen scaffolds. This composite structure was cultured in EGM-2:DMEM/F12:McCoy's 5A (1:1:1) medium to develop BTM-SS (Figure 2.7).

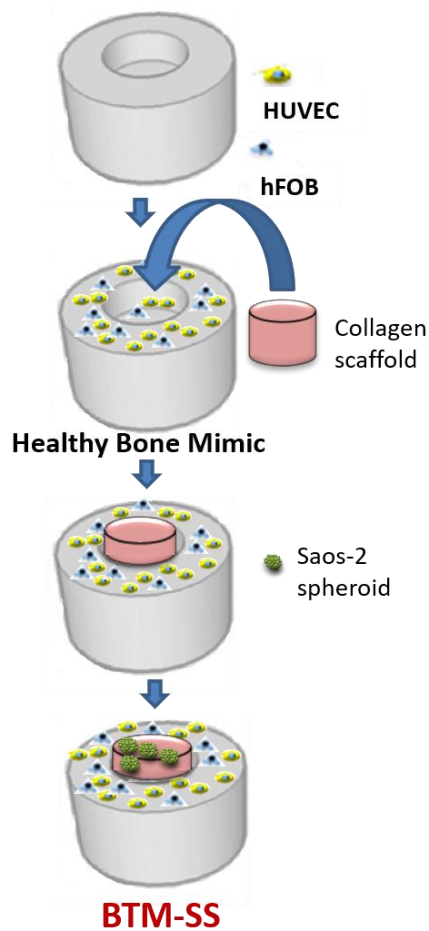


Figure 2.7. Preparation of BTM-SS.

2.2.5.3. Development of GelMA Scaffolds (BTM-G)

Synthesis of methacrylated gelatin (GelMA) hydrogels. Methacrylated gelatin was synthesized according to the process described by Kilic Bektas et al. (Kilic Bektas and Hasirci, 2018). Briefly, type A porcine skin gelatin was dissolved (10%, w/v) in PBS (10 mM, pH 7.4) at 50 °C. Methacrylic anhydride (20% v/v) was added into the solution at a rate of 0.5 mL/min under stirrer conditions at 50 °C for 1 h. The mixture was diluted five-fold with PBS to stop the reaction, dialyzed (CO 10,000) against distilled water for 1 week, the dialyzed solution was lyophilized and stored at +4°C for further studies.

Development of BTM-G. Spheroids formed over 10 days were suspended in GelMA solution (1% w/v in growth medium) and placed in the cylindrical cavities of bone mimic and then crosslinked with UV (0.120 Joule/cm²) for 1 min. Then, BTM-G were cultured in EGM-2:DMEM/F12:McCoy's 5A (1:1:1) medium (Figure 2.8).

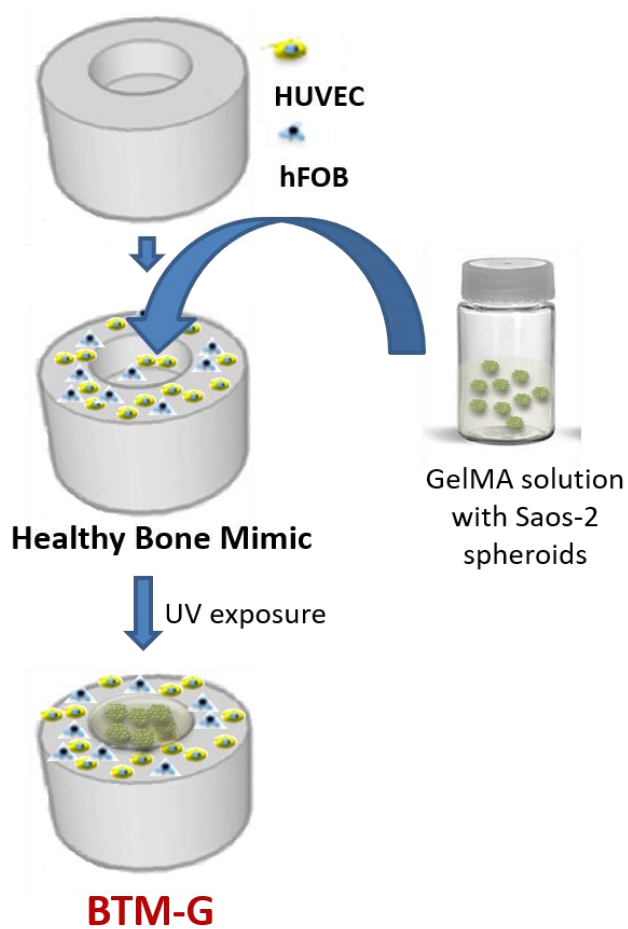


Figure 2.8. Preparation of BTM-G.

2.2.6. Characterization of Bone Tumor Models

2.2.6.1. Live/Dead Cell Viability Assay

Live/Dead cell viability assay was used to study the viability of the cells in the scaffolds. Samples were washed with PBS and incubated in a mixture of calcein AM (0.5 $\mu\text{L}/\text{mL}$ in PBS) and ethidium homodimer-1 (2 $\mu\text{L}/\text{mL}$ in PBS) for 15 min at RT. Stained samples were visualized with CLSM.

2.2.6.2. Alamar Blue Cell Viability Assay

Alamar Blue cell viability assay was conducted for BTM-SS as described in Section 2.2.4.1.

2.2.6.3. Alkaline Phosphatase (ALP) Activity

ALP activity assay was carried out for BTM-SS model. The SensoLyte pNPP alkaline phosphatase test kit was used to determine ALP activity. The Kit contains p-nitrophenyl phosphate (pNPP) as a phosphatase substrate transforming to yellow when it was dephosphorylated with the enzyme ALP ($\lambda_{\text{max}} = 405 \text{ nm}$). The samples were washed with component B in Kit, cut with a lancet, and 500 μL lysis buffer was added. Then, the samples were frozen and thawed three times at $-80 \text{ }^\circ\text{C}$ and $37 \text{ }^\circ\text{C}$, respectively, and sonicated with sonication probe at 50 W for 30 s. After centrifugation (2000 rpm, 10 min and then 5000 rpm, 2 min), the supernatant containing ALP was obtained. The supernatant (50 μL obtained from samples), ALP dilution buffer (50 μL) and component A (50 μL) was added on 96 well plates and incubated for 1 h at $37 \text{ }^\circ\text{C}$. Finally, 50 μL reaction stop solution was transferred to 96-well plates and the absorbances were measured at $\lambda=405 \text{ nm}$ in a plate reader (Molecular Devices, USA). ALP concentration was calculated by using a calibration curve prepared with the Kit components.

The supernatants obtained by this assay were also used to determine the amount of DNA by using PicoGreen Test (Quant-IT PicoGreen dsDNA test kit, Invitrogen). Thus, the total amount of DNA in the models was determined and the number of cells

in the samples was calculated. In the ALP activity test, supernatant also contained the DNA obtained in the last step. 50 μL cell supernatant and 150 μL PicoGreen working buffer (199 μL Tris-EDTA buffer and 1 μL Quant-IT PicoGreen® dsDNA reagent) were added to 96-well plates for each sample. The DNA concentration was then measured with the fluorometer by exciting at 485 nm and measuring the fluorescence intensity at 520 nm. All samples were tested in triplicate. The lambda DNA standard was prepared with ALP lysis buffer and diluted at the desired concentrations (10, 25, 50, 100, 250 and 500 ng/mL) with Tris-EDTA buffer solution to prepare a calibration curve. A single human diploid cell contains approximately 7 pg of DNA (Kumar et al., 2013, Macaulay and Voet, 2014). To calculate the number of cells, the amount of DNA obtained from the cells was divided by 7.

2.2.6.4. Immunocytochemistry

Immunocytochemistry staining was conducted for BTM-S, BTM-SS, and BTM-G as described in Section 2.2.4.3 without separating the two different scaffolds from each other. Specific antibody staining was performed for BTM-S. For sectioning of BTM-S, samples were incubated in the order of 15% sucrose, 30% sucrose and 30% sucrose:OCT (in the ratio of 1:1 v/v) (Tissue-Tek, USA) for 30 min. Samples were placed in OCT, frozen at $-80\text{ }^{\circ}\text{C}$ and sectioned with cryomicrotome. Sections were incubated in 1X blocking solution (5% goat serum, 1% Tween 20, 1% BSA and 1% sodium azide in PBS) for 1 h at $37\text{ }^{\circ}\text{C}$. Then, sections were incubated in anti-CD31 primary Ab ($10\text{ }\mu\text{g.mL}^{-1}$ in 0.1X blocking solution) and anti-von Willebrand factor (vWF) primary Ab ($0.05\text{ }\mu\text{g.mL}^{-1}$ in 0.1X blocking solution) at $4\text{ }^{\circ}\text{C}$ overnight, washed with PBS and incubated in donkey anti-sheep secondary Ab (Alexa Fluor® 594) ($0.02\text{ }\mu\text{g.mL}^{-1}$ in 0.1X blocking solution) and goat anti-rabbit secondary Ab (Alexa Fluor® 647) ($0.02\text{ }\mu\text{g.mL}^{-1}$ in 0.1X blocking solution) for 1 h at $37\text{ }^{\circ}\text{C}$. Samples were washed with PBS and incubated in Alexa Fluor 488-Phalloidin for 1 h at $37\text{ }^{\circ}\text{C}$ and DAPI for 15 min at RT and then examined with CLSM.

2.2.6.5. SEM

SEM analysis was performed as described in Section 2.2.4.4.

2.2.6.6. MicroCT Analysis

MicroCT analysis was conducted for BTM-S and BTM-SS. The effect of the cells on the internal structure of the sponges, calcium phosphate-forming capacities, the changes in sponge porosity due to the cells and the effect of integration of the separate cell seeded constructs were examined by analyzing MicroCT images. For BTM-SS, 1000 horizontal sections were used and analyses were performed on the grayscale values changes between 14 and 255. For BTM-S, 1273 slices were examined and analyses on the grayscale values change between 14 and 255. Digital microradiographic images of BTM-S were acquired at 59 kV and 167 μ A.

2.2.6.7. Molecular Analysis of Angiogenesis

2.2.6.7.1. RNA Isolation

Three different Saos-2 samples were analyzed: Saos-2 on TCPS (TCPS), Saos-2 on collagen scaffolds alone (Coll), and Saos-2 on collagen scaffolds placed in the cavity of the hFOB/HUVEC co-cultured PLGA/TCP scaffolds (Coll/BTM). On days 7, 14 and 21, RNA isolation was performed using the RNeasy Micro Kit (Qiagen) according to the manufacturer's protocol. Briefly, cells were disrupted with buffer RLT (350 μ L) by vortexing, added into QIAshredder spin column for homogenization and centrifuged (14000 rpm, 2 min). Total RNA content of the Saos-2 cultured on collagen scaffolds was also extracted by using the same Kit according to the manufacturer's instructions.

Ethanol (70%, 350 μ L) was added and the suspension was transferred to a RNeasy MinElute spin column and centrifuged (10000 g, 15 s). The spin column was washed with RW1 buffer (700 μ L), RPE buffer (500 μ L) and ethanol (80%, 500 μ L). RNA was eluted from the membrane by centrifugation (14,000 rpm, 1 min) with nuclease free water (22 μ L). Finally, the RNA sample was incubated at 65 °C for 7 min and

treated with DNase I to clean the contaminating DNA. DNase I treatment was performed using DNA-free™ kit (Ambion, Invitrogen, Germany). Briefly, RNA solution (20 µL) was incubated with DNase I buffer (2 µL) and rDNase I (1 µL) at 37 °C for 30 min. Then DNase inactivation reagent (2 µL) was added to the solution and incubated for 2 min at room temperature, mixing occasionally during the incubation. Lastly, the solution was centrifuged (10,000 g, 5 min) and the supernatant was transferred into a DEPC treated tube and stored at -80 °C until used.

2.2.6.7.2. First Strand cDNA Synthesis

First strand cDNA synthesis was performed by using RevertAid First Strand cDNA Synthesis Kit (Invitrogen, Germany). The reagents were added into a sterile, DEPC treated tube (Table 2.1).

Table 2.1. *Reagent volumes used for first step of cDNA synthesis.*

Reagent	Volume
Total RNA	1 µg
Oligo (dT)18 Primer	1 µL
Nuclease Free Water	To complete to 12 µL
Total volume	12 µL

This solution was incubated at 65 °C for 5 min and chilled on ice. Then the following components were added in the following order (Table 2.2).

Table 2.2. Reagent volumes used for second step of cDNA synthesis.

Reagent	Volume (µL)
5X Reaction Buffer	4
Ribolock RNase inhibitor (20 u/µL)	1
10 mM dNTP mix	2
Revertaid M-MuLV Reverse Transcriptase (200 u/µL)	1
Total Volume	20

2.2.6.7.3. Quantitative Real Time Polymerase Chain Reaction (qRT-PCR)

Molecular analysis of angiogenesis was conducted for BTM-S. It was assessed using qRT-PCR (Rotor-Gene Q; Qiagen) and $2^{-\Delta\Delta C_t}$ relative quantification method. In the qRT-PCR optimization of VEGF, bFGF and IL-8 primers, a mixture containing the following reagents were prepared (Table 2.3) and the qRT-PCR reaction conditions were as follows (Table 2.4). Primers for VEGF, bFGF and IL-8 genes by Sentegen (Sentegen, Turkey) according to the sequences and the amplicon sizes given in Table 2.5.

Table 2.3. Reagent volumes used for the qRT-PCR reaction.

Reagent	Volume (µL)
SybrGreen Master Mix (2X)	12.5
Forward Primer	2.5
Reverse Primer	2.5
cDNA	2.0
Nuclease Free Water	5.5
Total Volume	25.0

Table 2.4. *qRT-PCR reaction conditions for VEGF, bFGF and IL-8 primers.*

Process	Conditions
Initial Denaturation	95 °C, 5 min
Denaturation	95 °C, 5 s
Annealing and Extension	60 °C, 10 s
Melt	50 °C-99 °C; 1 °C/1 cycle

Table 2.5. *qRT-PCR primers and the amplicon sizes.*

	Primers (5'-3')	Sequence	Amplicon size (bp)
VEGF	Forward Primer	GAGTACCCTGATGAGATCGAGT	193 bp
	Reverse Primer	ATTTGTTGTGCTGTAGGAAGCT	
bFGF	Forward Primer	ATGGCAGCCGGGAGCATCACC	235 bp
	Reverse Primer	CACACACTCCTTTGATAGACACAA	
IL-8	Forward Primer	CATACTCCAAACCTTTCCAC	165 bp
	Reverse Primer	TCAAAAACCTTCTCCACAACC	

2.2.6.7.4. Agarose Gel Electrophoresis

Agarose (2%) was prepared in Tris-EDTA (1X) buffer solution, dissolved in the microwave and EtBr was added. The solution was poured into the tank and allowed to cool for 30 min for gel formation. The gel was then placed in the separator buffer tank, into which the electrodes were placed. Subsequently, samples were loaded into the wells and potential 100 V was applied. Samples were run on the gel for 75 min dissociation and visualized under UV light (UVP GelDoc Imaging System, USA).

2.2.7. Efficacy of Anticancer Agent on BTM-S Model

Doxorubicin (Sigma Aldrich, Germany) was chosen as anticancer agent and its activity on the model was investigated.

2.2.7.1. Preparation of Dose-Response Curve

The Dose-Response curve for doxorubicin was prepared using 2D culture at concentrations in the range 0.001 $\mu\text{g/mL}$ -100 $\mu\text{g/mL}$ to determine the dose of the drug to be applied to the 3D BTM-S. Saos-2 cells (2×10^4) were seeded on the 96-well tissue culture plate and incubated in McCoy's 5A medium for 24 h at 37 °C. Then, the medium was removed, cells were washed with PBS and doxorubicin-containing medium was added on cells and incubated for 24 h. The cells were washed with PBS and 200 μL fresh culture medium was added and incubated for another 24 h. The cells were then washed with PBS, 250 μL Alamar Blue solution (10%) was added and incubated for 1 h. 200 μL of Alamar Blue solution from each well was transferred to 96-well cell culture plates and absorbance was measured at 570 nm (λ_1) and 595 nm (λ_2) in a plate reader.

BTM-S was developed as described in Section 2.2.5.1 and the composite model was cultured in EGM-2:DMEM/F12:McCoy's 5A (1:1:1) medium for 7 d. According to dose-response curve, IC_{50} value was determined as 0.1876 $\mu\text{g/mL}$ with 2×10^4 cells/well. Since a total of 3×10^5 cells was seeded on the BTM-S, (Saos-2, HUVEC, and hFOB), 2.7 $\mu\text{g/mL}$ doxorubicin was applied on the 3D model and incubated for 24 h. The drug-containing medium was exchanged with fresh medium and incubated for 24 h. After that, characterization studies were carried out for both the control (drug-free) and drug-treated samples.

2.2.7.2. Alamar Blue Cell Viability Assay

Alamar Blue cell viability assay was performed on control and doxorubicin-treated samples by modifying the procedures in the Section 2.2.4.1. After treatment of drug for 24 h, samples were incubated for 3 days and then Alamar Blue solution (10% in DMEM high glucose colorless) was added on samples and incubated for 3 h at 37 °C and 5% CO₂ condition. After incubation, the Alamar Blue solution (200 µL) was transferred into 96 well plates. The absorbance of the solution was determined at both 570 nm (λ_1) and 595 nm (λ_2) with Elisa plate reader (Molecular Devices, USA). The absorbance was converted to 'percent reduction values' by using the Equation 2 (given on page 40).

2.2.7.3. Live/Dead Assay

Live/dead assay was conducted as described in Section 2.2.6.1.

2.2.7.4. Caspase-3 Enzyme Activity Assay

Caspase-3 Enzyme Activity Kit (Fluorometric) (Abcam, USA) was used to determine the caspase-3 enzyme activity in the control and doxorubicin-treated BTM-S according to the manufacturer's protocol. Cell lysis buffer was added to the samples and incubated on ice for 10 min. DTT and DEVD-AFC enzyme substrate from the kit components were added and incubated for 2 h at 37 °C. Fluorescence intensities were measured at 400 nm (λ_{ex}) ve 505 nm (λ_{em}) with a plate reader.

2.2.8. Statistical Analysis

Statistical analysis was performed with GraphPad Prism6 program. Differences between group means were analyzed with Student's T-test when the data were normally distributed. Comparisons of more than 2 groups were performed with One-way ANOVA with Tukey's posthoc test, to determine significant differences. All values are represented as the mean \pm standard deviation. Differences were taken to be significant for $p < 0.05$.

CHAPTER 3

RESULTS AND DISCUSSION

3.1. Characterization of PLGA/TCP and Collagen Sponges

3.1.1. Wettability

Water contact angle measurements were conducted to determine the wettability of the PLGA/TCP and collagen sponges. The contact angle of the PLGA/TCP sponge was found to be $114.5^{\circ} \pm 8.7^{\circ}$ indicating hydrophobicity (Table 3.1). Wettability is probably the most crucial factor defining the quantity and quality of proteins adsorbed on the surfaces and therefore affect biocompatibility. Although TCP is an inorganic material and more hydrophilic than PLGA, PLGA/TCP sponge was still hydrophobic. This can be due to the proportion of TCP (20% w/w) in sponges is not high enough to make the surface hydrophilic (Reinke et al., 2015) or the existence of porous structure. In a study, contact angles of PLGA films decreased significantly after incorporation of TCP (30% w/w) in the PLGA (Lee et al., 2019).

Table 3.1. *Contact angles of PLGA/TCP and collagen sponges.*

Sample	Contact angle
PLGA/TCP sponges	$114.5^{\circ} \pm 8.7^{\circ}$
Oxygen plasma treated PLGA/TCP sponges	$100.0^{\circ} \pm 6.1^{\circ}$
UXL-CS	$112.4^{\circ} \pm 2.4^{\circ}$
DHT-CS	$133.3^{\circ} \pm 2.2^{\circ}$
Oxygen plasma treated DHT-CS	$\sim 0^{\circ}$

Before tissue culture studies, oxygen plasma treatment (100W, 3 min) was applied on the PLGA/TCP sponges to oxidize the surface and open up pores for the migration of the cells in the depth of the sponges. After plasma treatment, the water contact angle was decreased to $100.0^{\circ} \pm 6.1^{\circ}$ (Table 3.1). In the literature, it is stated that there is a significant relationship between material properties and cell-substratum interaction. Anchorage-dependent mammalian cells (which need substratum adhesion for proliferation) favor modestly hydrophilic surfaces. Some researchers found that adhesion strength directly affects the cell growth rate and the wet surface is the most important factors of adhesion strength (Ermiş et al., 2018; Hasirci and Kenar, 2006).

The water contact angle of uncrosslinked (UXL) collagen sponge (UXL-CS) and dehydrothermal (DHT) crosslinked collagen sponge (DHT-CS) were measured as $112.4^{\circ} \pm 2.4^{\circ}$ and $133.3^{\circ} \pm 2.2^{\circ}$, respectively (Table 3.1). Collagen itself is a hydrophilic protein (Leikin et al., 1995). Nevertheless, scaffold processing techniques and fibrous nature of the collagen constructs change surface properties of the collagen scaffolds. According to a study conducted by Ghaeli et al., the water contact angle of crosslinked collagen films having nano roughness was measured as 97.14° (Ghaeli et al., 2017). The surface topography may also affect the wettability of collagen sponges. Moreover, the collagen sponges became more hydrophobic after DHT treatment. During DHT crosslinking, ester and amide bonds are created either by esterification or amide formation decreasing the amount of the free carboxyl, amine, and hydroxyl groups and result in more hydrophobic materials (Pulieri et al., 2008). After oxygen plasma treatment on DHT-CS, the contact angle was too low to measure, it was very hydrophilic. Oxygen plasma creates various functional groups such as hydroxyl, carbonyl, carboxyl, ether, and peroxide on the surfaces applied. Moreover, oxygen plasma etches scaffold surfaces by way of reactions between atomic oxygen and the surfaces (Lehocký et al., 2003; Cvelbar et al., 2005). All these combined effects lead to formation of more hydrophilic collagen sponges.

3.1.2. Degradation

Degradation test was carried out to determine the stability of the sponges in the aqueous environment. Degradation profile of the PLGA/TCP sponges in PBS is shown in Figure 3.1. It was observed that in 7 weeks, there was approximately 2% weight loss. It shows that the material is stable enough to be used in the drug affinity experiments.

The degradation rate is also a critical point that should be considered while designing a tissue-engineered scaffold to predict how long the implant will stay in cell culture for *in vitro* model system. Obviously, the presence of ECM-secreting cells or their absence, influence this rate significantly. Depending on the application, the material is chosen to be nondegradable or degradable (Wu and Ding, 2004). In this study, the first intended purpose of the 3D scaffolds is to prepare an *in vitro* bone tumor model system, and stable PLGA scaffolds are preferable since the long *in vitro* tests would require stability.

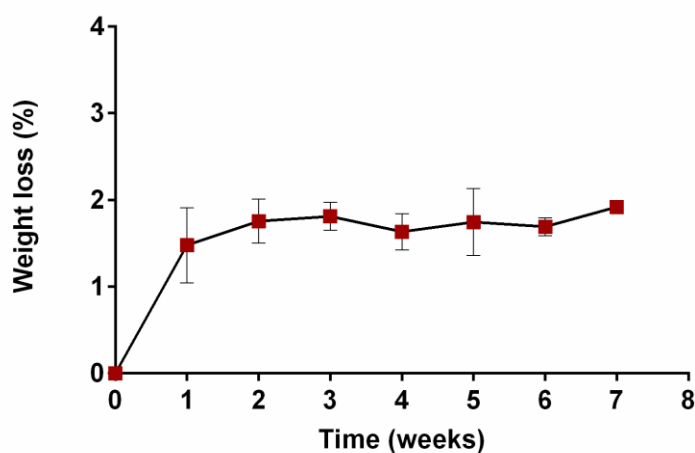


Figure 3.1. Degradation of the PLGA/TCP sponges in PBS (0.01 M, pH 7.4) at 37 °C.

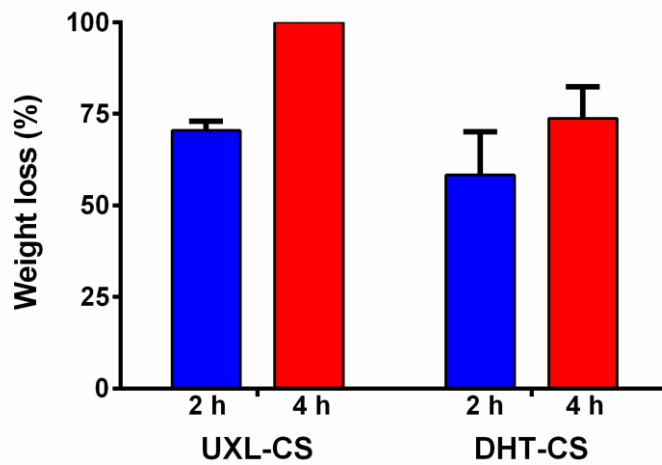


Figure 3.2. Enzymatic degradation of the UXL-CS and DHT-CS in collagenase type II solution (0.1 mg/mL in PBS) at 37 °C.

Enzymatic degradation of the UXL-CS and DHT-CS was carried out in collagenase type II solution (Figure 3.2). After 2 h incubation, the weight loss was $70.5 \pm 2.5\%$ for UXL-CS and $58.3 \pm 11.8\%$ for DHT-CS. When incubation time was increased to 4 h, UXL-CS completely disintegrated while DHT-CS lost $73.8 \pm 8.6\%$ of its weight (Figure 3.2). Dehydrothermal (DHT) treatment is a widespread physical crosslinking method of collagen (Sun et al., 2018). Other studies report also that DHT is effective as a crosslinking method and decrease the rate of the degradation (Weadock et al., 1996; Cornwell et al., 2007). In a study, after 24 h incubation in collagenase solution, weight loss of electrospun collagen scaffolds decreased from $89.95 \pm 10.15\%$ to $69.07 \pm 14.15\%$ when samples were DHT crosslinked, these reports support our results (Drexler and Powell, 2011).

3.1.3. Compressive Mechanical Properties

Compressive mechanical tests were conducted on the sponges. Figure 3.3A shows the characteristic stress-strain curve obtained with PLGA/TCP sponges prepared in two different compositions. The elastic modulus of the sponges with the weight ratio of PLGA/TCP/NaCl (4:1:20) and PLGA/TCP/NaCl (4:1:40) are 5.18 MPa and 4.76

MPa, respectively (Table 3.2). When the weight ratio of NaCl was increased, porosity also increased and so elastic modulus decreased, as expected. Similar results were also noted in a study (He et al., 2014). They compared the mechanical property and porosity of cylindrical shaped PLLA sponges prepared with different ratios of PLLA to NaCl particles and found that when the NaCl ratio increased, the porosity increased and Young's modulus decreased (He et al., 2014). As presented in Section 1.1.5, trabecular bone shows viscoelastic behavior and its modulus is 50-100 MPa. The modulus of our 3D model is around the 5 MPa that is not close the real bone. Since the bone tumor model will not be used in the load-bearing application, this kind of modulus may be acceptable. Xie et al. were prepared PLGA/TCP scaffolds by dissolving PLGA in 1,4-dioxane and adding TCP powders PLGA:TCP ratio of 4:1 (w/w) (same with our composition) by using computer-controlled biospinning technology, and Young's modulus of the scaffolds were found as 50 MPa that is 10 times higher than our scaffolds. This was probably the result of scaffold processing technique and lack of addition of salt particles that could result in higher porosity and lower mechanical properties (Xie et al., 2010).

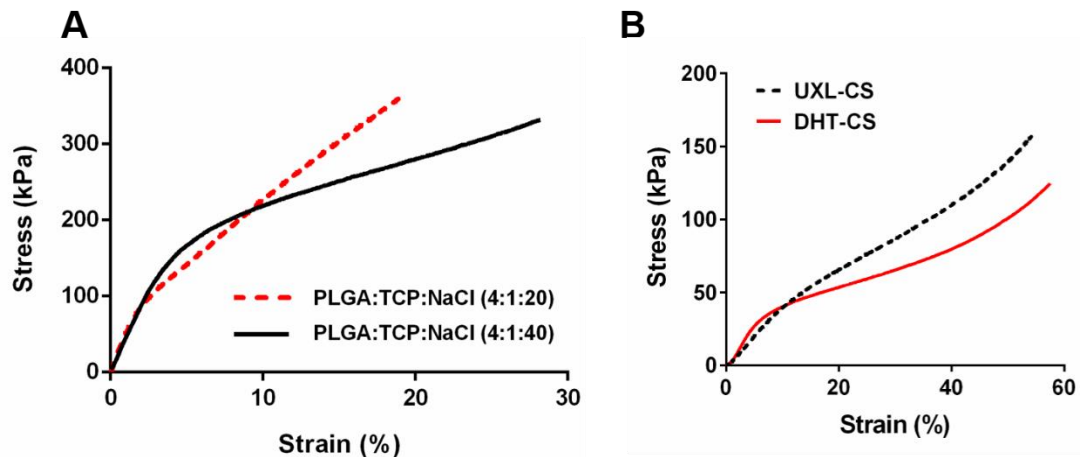


Figure 3.3. Characteristic stress-strain curves of the sponges. Stress-strain curve observed for (A) PLGA/TCP sponges with the weight ratio of PLGA:TCP:NaCl (4:1:20) and PLGA:TCP:NaCl (4:1:40); (B) UXL-CS and DHT-CS under compression.

Table 3.2. *Young's modulus of PLGA/TCP sponges, trabecular bone and collagen sponges.*

Sample	Young's Modulus
PLGA/TCP/NaCl (4:1:20)	5.18 MPa
PLGA/TCP/NaCl (4:1:40)	4.76 MPa
Trabecular Bone	50-100 MPa
UXL-CS	111±18 kPa
DHT-CS	140±46 kPa

Stress-strain curves of the UXL-CS and DHT-CS are shown in Figure 3.3B. Elastic modulus of the UXL-CS and DHT-CS were 111±18 kPa and 140±46 kPa, respectively (Table 3.2). There was an increase in the elastic modulus value after DHT treatment but it was not significant. It was expected that crosslinking increases the elastic modulus of the sponges. Since sponges may not be prepared with uniform porosity and pore structure by freeze drying technique, this can result in a variation of the elastic modulus of samples in the same group and this reduces the significance. There are several studies showing that DHT crosslinking increase the mechanical properties of the collagen-based constructs (Haugh et al., 2009; Keogh et al., 2010; Drexler and Powell, 2011; Yahyouche et al., 2011; Kozłowska et al., 2017; Sun et al., 2018).

3.1.4. Microarchitecture

Surface morphology is a property which influences protein adsorption and cell attachment (Zhang et al., 2002). SEM micrographs of the PLGA/TCP sponges are shown in Figure 3.4. NaCl particles were homogeneously distributed in the scaffolds and their sizes are in the range 150-250 µm, because of the salt crystal dimensions used (Figures 3.4A and 3.4B). The average pore size of the PLGA:TCP:NaCl (4:1:40) sponge was 199±52 µm by using ImageJ (NIH, USA). In bone tissue engineering, scaffolds are usually produced with a pore size similar to trabecular bone (200-900 µm) (Arca et al., 2011). It was reported that pores in the range 160–270 µm support rapid and extensive angiogenesis within a scaffold (Artel et al., 2011).

Hydroxyapatite scaffolds produced with average pore size of 200 or 500 μm for *in vitro* culture of human mesenchymal stem cells (MSCs) showed that 200 μm pore sized scaffolds have a faster rate of osteogenic differentiation than 500 μm pore sized scaffolds (Mygind et al., 2007). Moreover, 3D silk sponges were manufactured with a pore diameter of 200–325 μm to mimic bone matrix (Meinel et al., 2006). It can be said that the pore size of our construct (199 ± 52 μm) is in the range of the ideal pore size of the bone matrix.

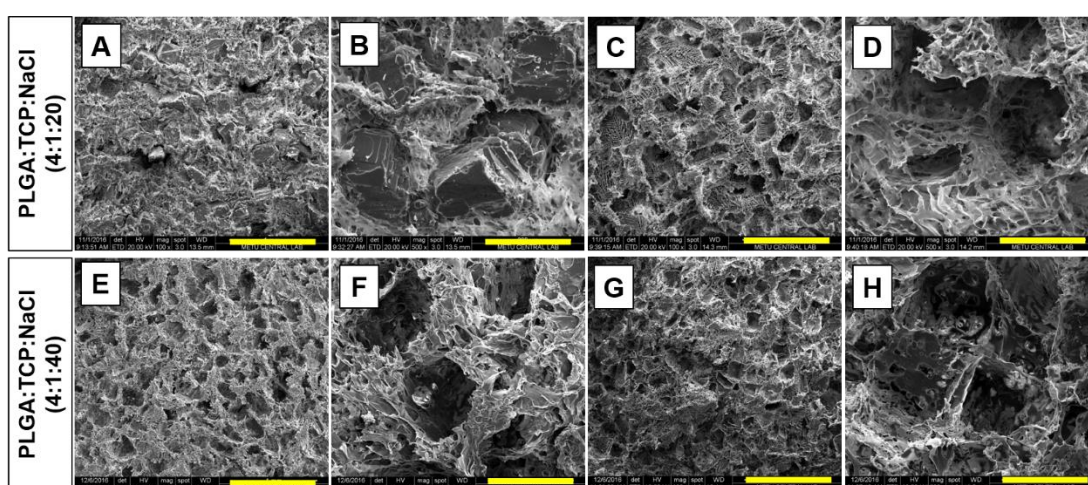


Figure 3.4. SEM micrographs of the PLGA/TCP sponges. (A-D) PLGA:TCP:NaCl (4:1:20), (A, B) as prepared with salt particles, (C, D) salt leached, horizontal cross section, (E-H) PLGA:TCP:NaCl (4:1:40), (E, F) salt leached, horizontal cross section, (G, H) salt leached, longitudinal cross section. (Scale bar: 1 mm for Figure A, C, E, G; 200 μm for Figure B, D, F, H).

The pore morphology and pore size were also examined with SEM. Figures 3.4C and 3.4D show horizontal cross sections of the salt leached sponges containing less NaCl and Figures 3.4E and 3.4F show that of high NaCl fraction. Figures 3.4G and 3.4H present the SEM micrographs of a longitudinal section of PLGA/TCP scaffolds containing high NaCl. There was no difference in the morphology and pore size of the scaffolds that were sectioned horizontally and longitudinally.

Energy dispersive X-ray spectroscopy (EDX) was used in the elemental analysis of the cross sections of the PLGA/TCP sponges to demonstrate the complete removal of the salt from the sponges. Figure 3.5A shows the EDX analysis of a NaCl particle. As expected, only Na and Cl peaks were detected. Figure 3.5B presents the EDX analysis of PLGA/TCP sponges. Na and Cl peaks are observed in this EDX analysis because this sample was not salt leached. Finally, EDX analysis was done for a cross section of salt leached PLGA/TCP scaffolds and no Na and Cl peaks were detected (Figure 3.5C) showing total salt leaching.

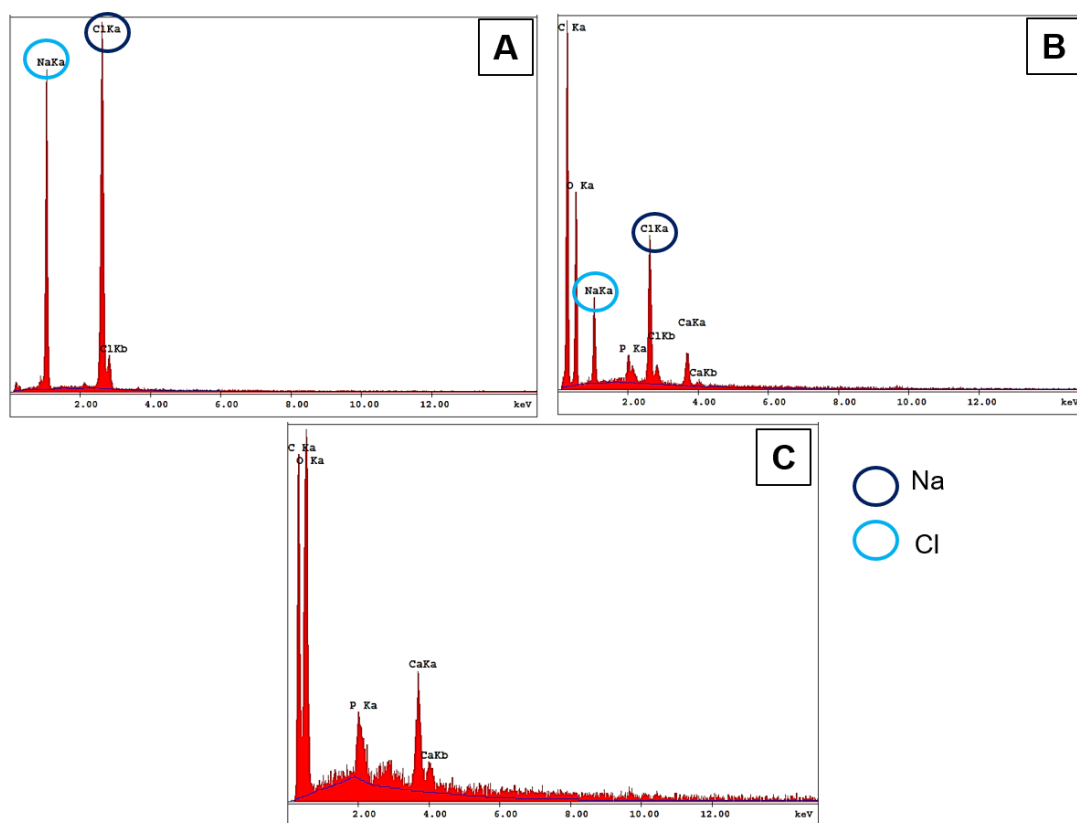


Figure 3.5. Energy dispersive X-ray (EDX) analysis of a NaCl particle and PLGA/TCP sponges before and after leaching. (A) NaCl particle, (B) PLGA/TCP sponge with salt particles, (C) PLGA/TCP sponge after salt leaching.

In addition to the analysis of horizontal and longitudinal cross sections of the PLGA/TCP scaffolds, the bottom of the cavity and wall surface of the scaffolds were examined with SEM to see the microstructural differences. A skin layer was formed on the scaffold that interacts the Teflon mold and this layer did not contain large pores like in the cross section of the scaffolds (Figures 3.6A and 3.6B). The SEM micrographs of the wall surface of the scaffold has different topography resemble like channels (Figures 3.6C and 3.6D).

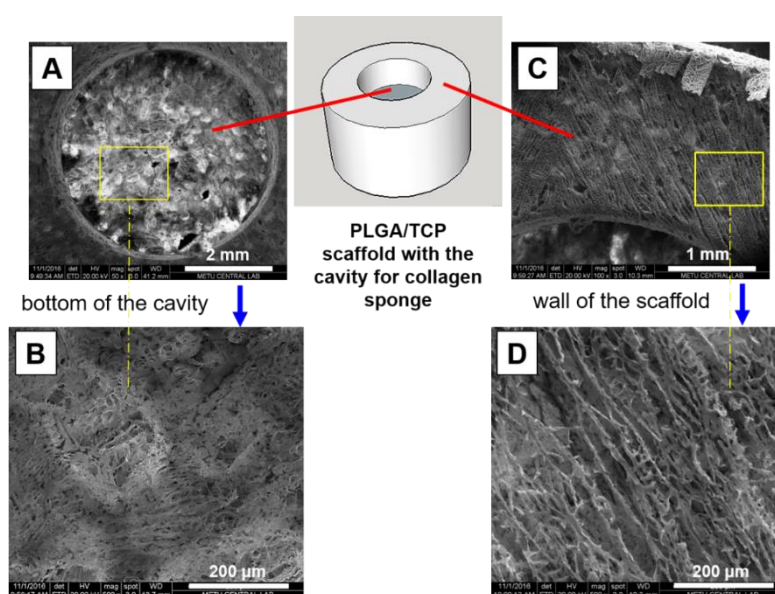


Figure 3.6. SEM micrographs of the PLGA/TCP scaffolds. (A, B) Bottom of the cavity, and (C, D) wall of the scaffold.

It was stated that hFOB and HUVEC cells may not be migrated to the inner parts of the scaffolds because of the skin layer formed on the wall surface of the constructs. Then, oxygen plasma treatment was conducted with different power and time to remove the skin layer and to generate pores on the surface. SEM micrographs of the surface of the sponges are given in Figure 3.7. When oxygen plasma treatment was applied 100 W for 3 min, pores were produced and for further studies, these plasma treatment parameters were applied to the samples before tissue culture studies.

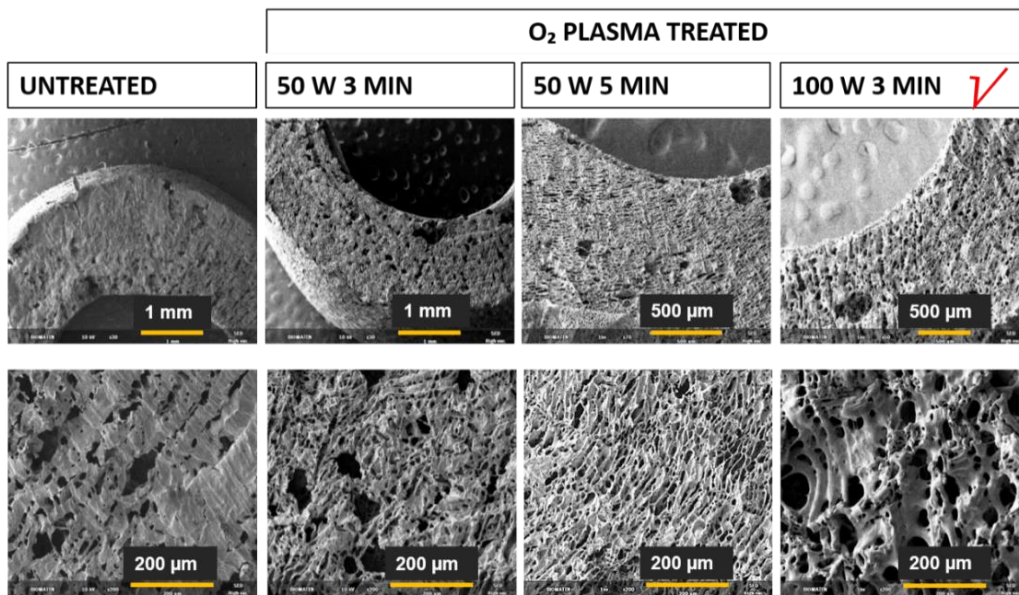


Figure 3.7. SEM micrographs of oxygen plasma treated and untreated PLGA/TCP scaffold surfaces.

The internal porous structure of the collagen scaffolds was also examined with SEM. Figures 3.8A and 3.8B present the SEM micrographs of the horizontal cross section of the collagen sponges showing that the sponges have high porosity and interconnectivity. Figures 3.8C and 3.8D show the SEM micrographs of the longitudinal cross section of the collagen scaffolds and porosity and pore interconnectivity are high here, too. There were no differences between the porosity and pore morphology of the horizontally and longitudinally cross sectioned sponges. High porosity and pore interconnectivity are very important for good cell culturing to generate the homogenous cell distribution in the whole part of the scaffold. The diameter of pores is in the range of 50-150 μm measured by using ImageJ (NIH, USA).

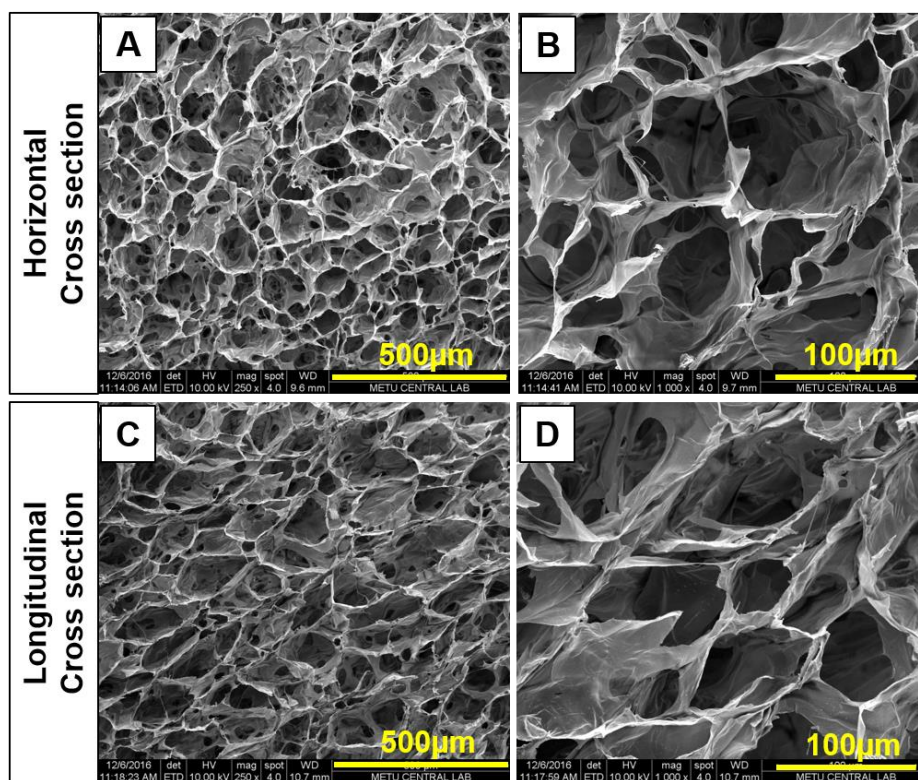


Figure 3.8. SEM micrographs of collagen scaffolds. (A, B) Horizontal cross section, (C, D) longitudinal cross section.

3.1.5. MicroCT Analysis

The inner microstructure of the PLGA/TCP and collagen sponges were examined and their porosities were determined with microCT. The porosities of the PLGA/TCP sponges prepared with the weight ratio of PLGA:TCP:NaCl (4:1:20) and PLGA:TCP:NaCl (4:1:40) were determined as 92.6% and 96.7%, respectively. It was an expected result because porosity increases with increasing the fraction of leachable NaCl particles. The porosity of PLGA/TCP scaffolds are similar to that found in cancellous bone (75–95%) (Ramírez-Rodríguez et al., 2017). MicroCT images of the PLGA/TCP scaffolds prepared with different NaCl fractions observed from different angles (Figures 3.9A-D) showed that TCP particles are homogeneously distributed through the sponges. The perfect cylindrical shape of the scaffold and the cavity that was formed at the center of the scaffold can be observed in the images.

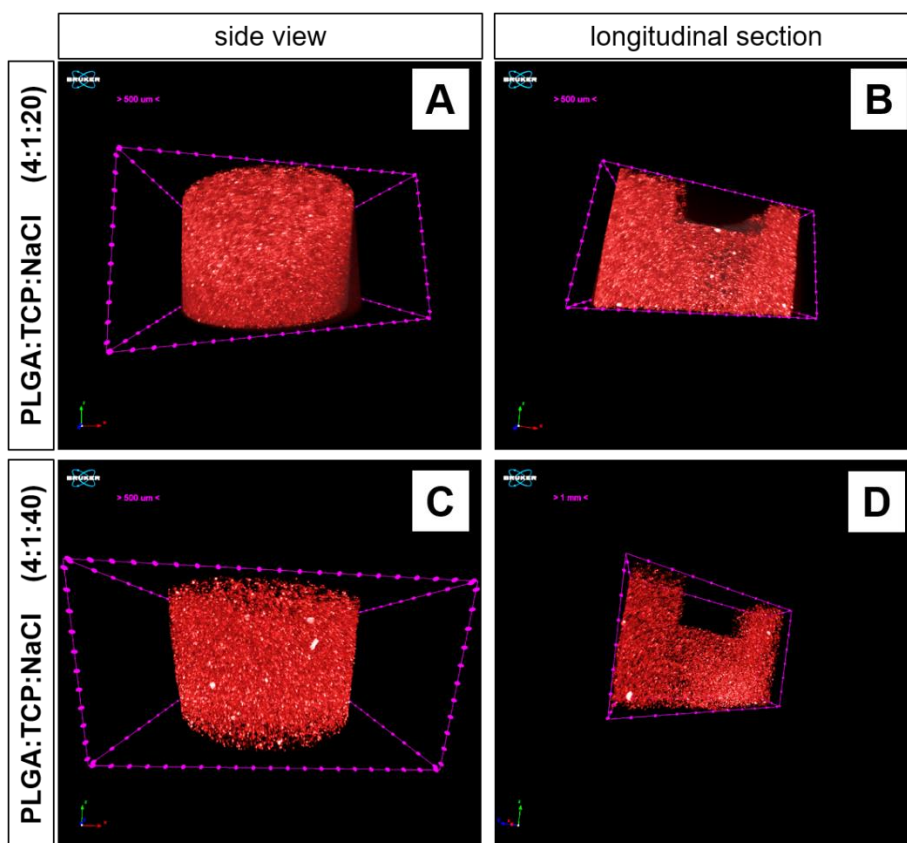


Figure 3.9. MicroCT images of the PLGA/TCP sponges after salt leaching. (A-B) Scaffolds prepared with the composition (w/w) PLGA:TCP:NaCl (4:1:20) (A) side view, (B) longitudinal section; (C-D) scaffolds prepared with the composition (w/w) PLGA:TCP:NaCl (4:1:40) (C) side view, (D) longitudinal section.

Figures 3.10A and 3.10B present side view and top view of the collagen sponges showing the cylindrical shape of them. The porosity of the collagen sponges was determined as 86%. High pore interconnectivity of the sponges can be clearly seen in the microCT image the sponge (Figures 3.10C and 3.10D). Figure 3.10E shows a representative microCT image of horizontal cross section of the sponge that shows collagen part (white) and pore part (red) of the sponges.

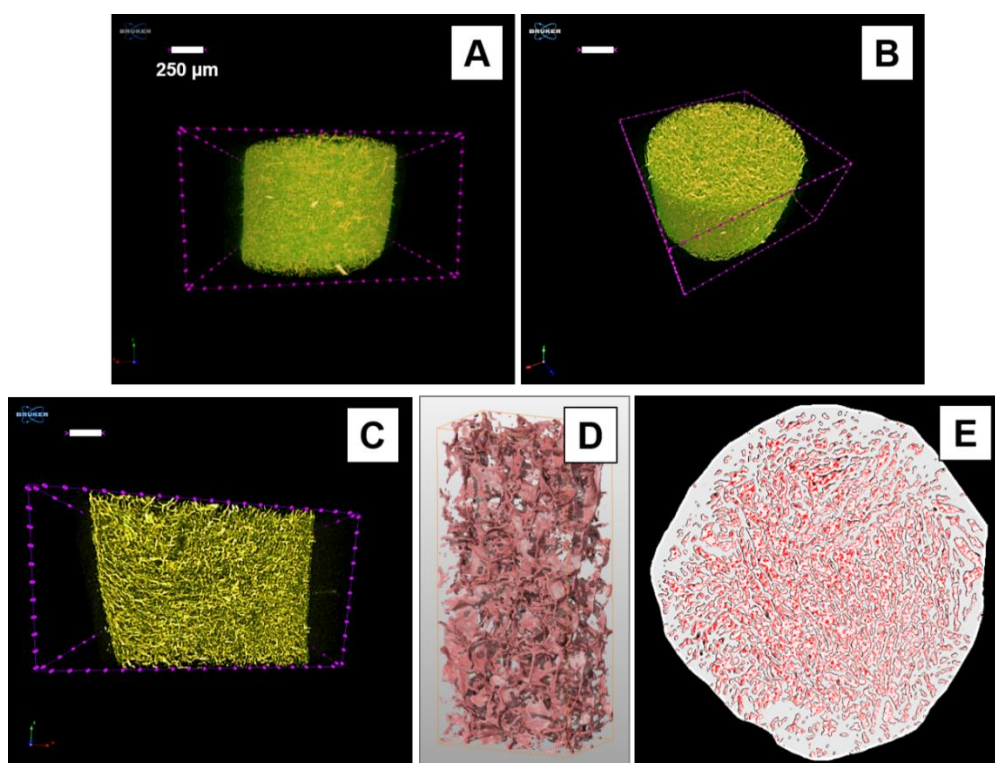


Figure 3.10. MicroCT images of the DHT-CS. MicroCT images of (A) side view, (B) top view, (C, D) longitudinal cross section, and (E) top view of the sponges.

3.2. Characterization of Cell Seeded Healthy Bone and Tumor Mimics

3.2.1. Alamar Blue Cell Viability Assay

Proliferation of the hFOB/HUVEC on PLGA/TCP scaffolds and Saos-2 on collagen scaffolds were determined with Alamar Blue cell viability assay. The cell number on Days 7, 14 and 21 were calculated by using a calibration curve prepared with known cell numbers.

The results of Alamar Blue cell viability assay of hFOB/HUVEC cells (1:1) on the PLGA/TCP scaffold are shown in Figure 3.11. Cell seeding density was 2×10^5 cells per well and on Day 1 approximately 2.7×10^5 cells were counted on the TCPS control while much less (8.7×10^4) cells were determined on the scaffolds. During cell seeding procedure, cell suspension containing the cells ran through the sponge into the culture

well and therefore the number of cells attached on the scaffold was roughly three times less than the TCPS surfaces. Cell numbers on scaffolds increased gradually over time, while, on TCPS, the cell number reached a plateau in a week indicating that confluency is reached. Pang et al. also showed that PLGA/ β -TCP scaffolds support the proliferation of bone mesenchymal stem cells (BMSCs) during two weeks (Pang et al., 2007).

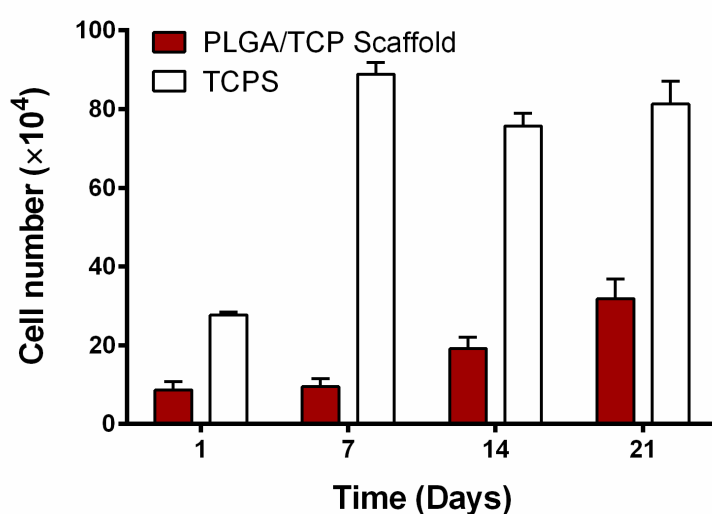


Figure 3.11. Cell proliferation of hFOB/HUVEC on the PLGA/TCP scaffolds. TCPS is a positive control. (Cell seeding density: 2×10^5 /scaffold).

The results of the Alamar Blue assay of Saos-2 cells seeded on the collagen scaffold are presented in Figure 3.12. Cell seeding density was half of that of the hFOB/HUVEC (1×10^5 cells/well). The proliferation of Saos-2 on TCPS was higher than that on the collagen. The cell number increase on TCPS continued for 3 weeks but on collagen, the rate of cell number increases and the cell number itself were lower. One reason for this difference might be that the TCPS has a larger area than the scaffold and the other reason could be that the cells on TCPS has easier nutrient and oxygen access due to its being 2D. On the 3D collagen sponges, cells must have

migrated into the pores of the sponge and probably could not have sufficient nutrient and oxygen flow as on TCPS. Other reason of the low cell numbers on the collagen sponges could be from the detection method: the dye reduced by the cells within the porous structure of the collagen sponge during the Alamar Blue test might not completely be detected unlike on the 2D TCPS. A lower cell division rate of osteosarcoma cells in 3D culture was also reported in literature. One study showed that G₁ phase cell cycle arrest of osteosarcoma cells can be seen in 3D culture. This might be the result of agents that are specific to the cell cycle in 3D cultured osteosarcoma cells, proliferation markers cyclin B1 and actin regulator RhoA, being significantly lower than those in 2D culture (Tan et al., 2016). Moreover, the 3D microenvironment is enough to influence the activation of the PI3K/AKT pathway that is a critical intracellular signaling cascade for the growth and migration of osteosarcoma cells. The decreased activity of the PI3K/AKT pathway in 3D cultured cells leads to decreasing the proliferation and migration of cells (Fallica et al., 2012).

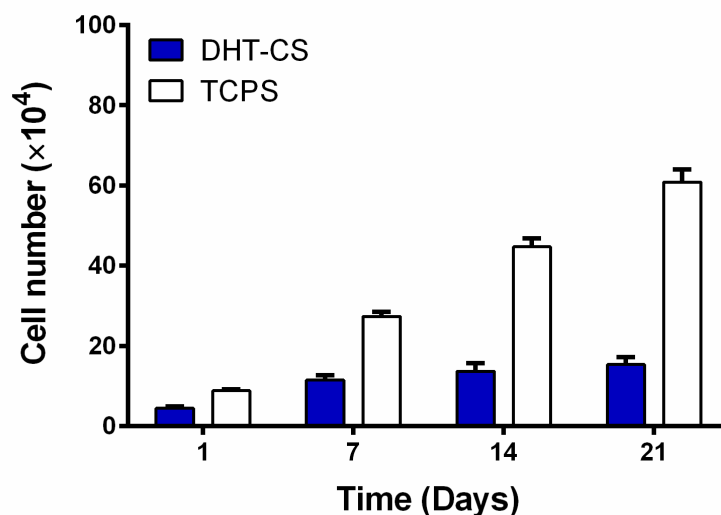


Figure 3.12. Cell proliferation of Saos-2 on the DHT-CS. TCPS is a positive control. (Cell seeding density: 1×10^5 cells/scaffold).

3.2.2. Alkaline Phosphatase (ALP) Activity

ALP activity of hFOB cells in the healthy bone mimic was measured to determine the osteoblastic activity of the cells (Figure 3.13A). ALP activity of hFOB on PLGA/TCP scaffolds increased during the 7 day incubation, however, it was approximately three times lower in comparison to control (TCPS). When ALP activity was normalized to the number of cells and specific ALP concentration was obtained with normalized data (Figure 3.13B), the activity of the 3D form is superior to the TCPS. Alkaline phosphatase activity is an indicator of bone formation capability. It was expected that 3D PLGA/TCP scaffold that mimics bone matrix would have a higher specific ALP activity than the 2D TCPS control.

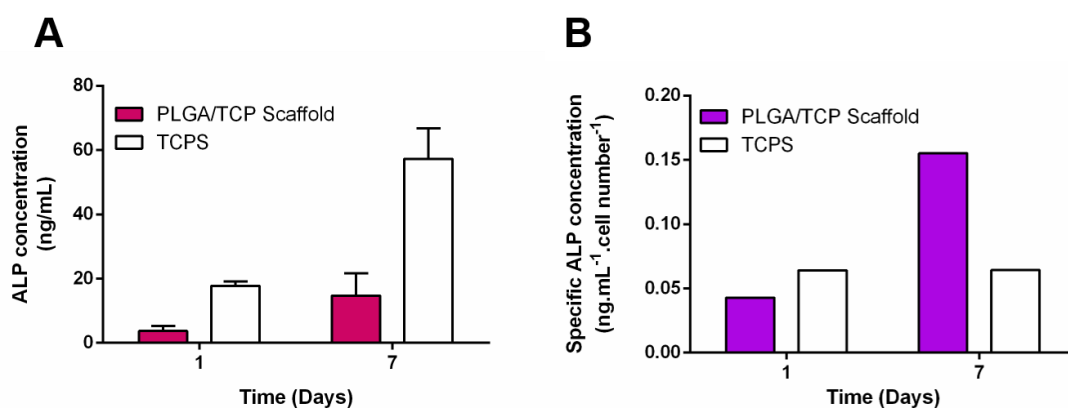


Figure 3.13. Alkaline phosphatase (ALP) activity of hFOB cells in healthy bone mimic. (A) Alkaline phosphatase (ALP) activity of hFOB cells on PLGA/TCP scaffolds. (B) Specific ALP activity of the hFOB on PLGA/TCP scaffolds normalized to cell numbers obtained from Alamar Blue cell viability assay.

3.2.3. Immunocytochemistry

Nucleus and cytoskeleton of hFOB/HUVECs co-cultured on PLGA/TCP scaffolds and of Saos-2 cells cultured on collagen scaffolds were stained to study cell morphology, intercellular interaction, and cell-material interactions through confocal microscopy.

CLSM micrographs of actin filaments (green) representing the cytoskeleton and nuclei (red) of hFOB and HUVECs on the PLGA/TCP scaffold are shown in Figure 3.14. Actin and nucleus dyes stained both the cells because no cell specific dye was used. On Day 7, the cells appear attached and spread well and covering most of the surface. On Day 14, the scaffold surface was completely covered cells. The cells adapted to the sponge surface topography over time and oriented themselves along the channel-like structures on the PLGA/TCP scaffold surface. On Day 21, the cells covered all the scaffold surface. The results of CLSM micrographs were supported by the cell viability test results given in Figure 3.11.

A study also reported good adhesion, proliferation, and growth of osteoblast cells on PLGA/TCP scaffolds. They showed that cells spread like flat spindle shape with protruded cellular extensions on scaffolds after incubating for 7 and 14 Days (Yang et al., 2011) as observed in our study. In another study, cellular extensions of osteoblast cells and ECM secreted between the cells on PLGA/TCP scaffolds were reported. They also observed that endothelial progenitor cells (EPCs) completely covered the scaffolds and showed high cellular interaction and a typical cobblestone morphology (Khojasteh et al., 2016). It can be concluded that the present PLGA/TCP scaffolds support hFOB and HUVECs attachment and proliferation and are a suitable matrix to generate bone tissue mimic by indicating normal cell metabolism such as good cell adhesion, spreading and proliferation on the scaffolds.

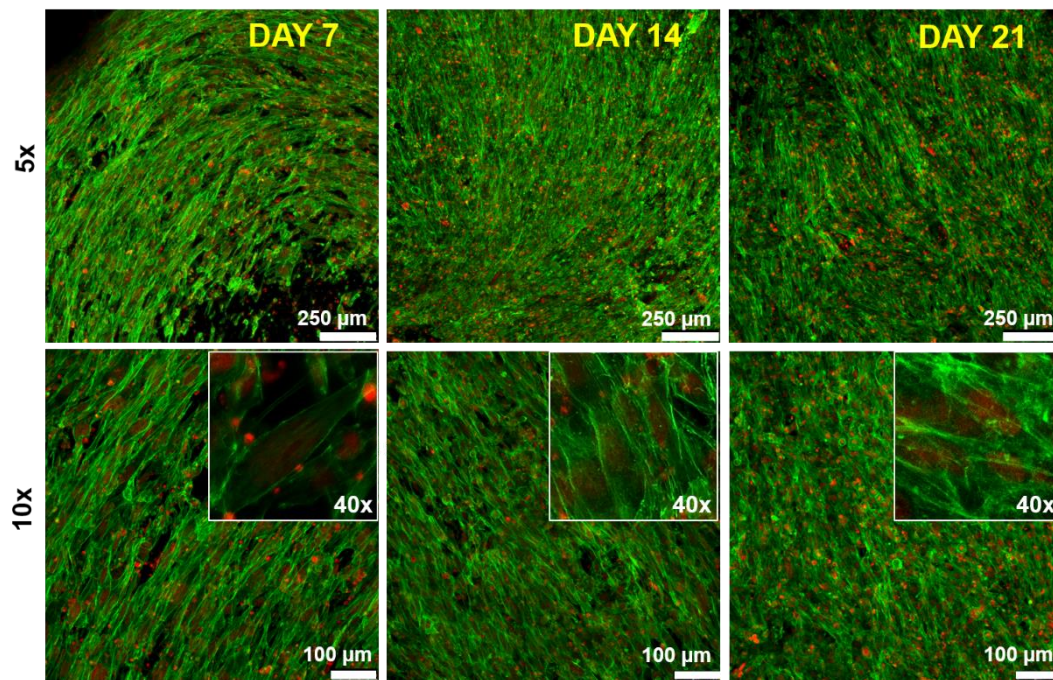


Figure 3.14. CLSM micrographs of the hFOB and HUVECs on PLGA/TCP scaffolds on Days 7, 14 and 21. Stains: Actin: Alexa Fluor 532 Phalloidin (green), and Nuclei: DRAQ5 (red). Cell seeding density = 2×10^5 /scaffold.

The CLSM micrographs of the healthy bone mimic is presented in Figure 3.15. Anti-human CD31 immunostaining of HUVECs on PLGA/TCP scaffolds showed that HUVECs express CD31 which is known as platelet endothelial cell adhesion molecule-1 (PECAM-1) and is expressed at high levels by early and mature endothelial cells (Edwards et al., 2018). These stains show that the HUVECs and hFOB on the PLGA based scaffolds.

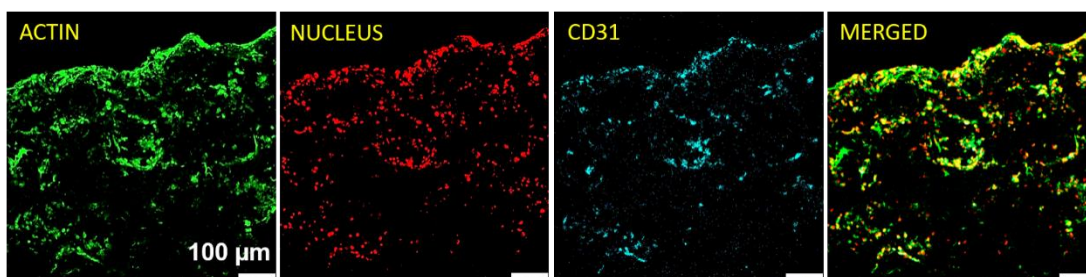


Figure 3.15. CLSM micrographs of the horizontal section of the hFOB and HUVECs on the PLGA/TCP scaffolds on Day 28. Stains: Actin: Alexa Fluor 532 Phalloidin (green), Nuclei: DRAQ5 (red), and CD31: Alexa Fluor 488 anti-human CD31 (blue). Scale bar: 100 μm.

A similar staining was also applied to Saos-2 cells. CLSM micrographs of cytoskeleton (green) and nucleus (red) of Saos-2 cells on collagen sponge are shown in Figure 3.16. On Day 7 (Figure 3.16A), the cells appear attached and spread on the pore of the collagen sponge. In time, cells proliferated, started to cover the pores in the sponge (Day 14, Figure 3.16B), and they eventually appeared to form cell layers over the surface (Day 21, Figure 3.16C). Figures 3.16D-F (high magnification images) are superimposed images of the cell nuclei and the cytoskeletons. Nuclei are elliptical (close to the round), preserved the morphology of typical Saos-2 cell nuclei (Figures 3.16G, 3.16I and 3.16K). Cytoskeletons at different times (Figures 3.16H, 3.16J, and 3.16L) show cell elongation and high density of actin. It is observed that cells attach and spread on the surface of the collagen scaffold and have spindle-like cell shape.

These findings were also parallel with the Saos-2 Alamar Blue assay results (Figure 3.12). The cell number could not increase anymore because the scaffold was fully covered with cells. CLSM studies were performed on both the upper (cell seeded side) and lower (non-direct cell seeded side) surfaces of the collagen sponge, and cell adhesion and proliferation were observed in both surfaces.

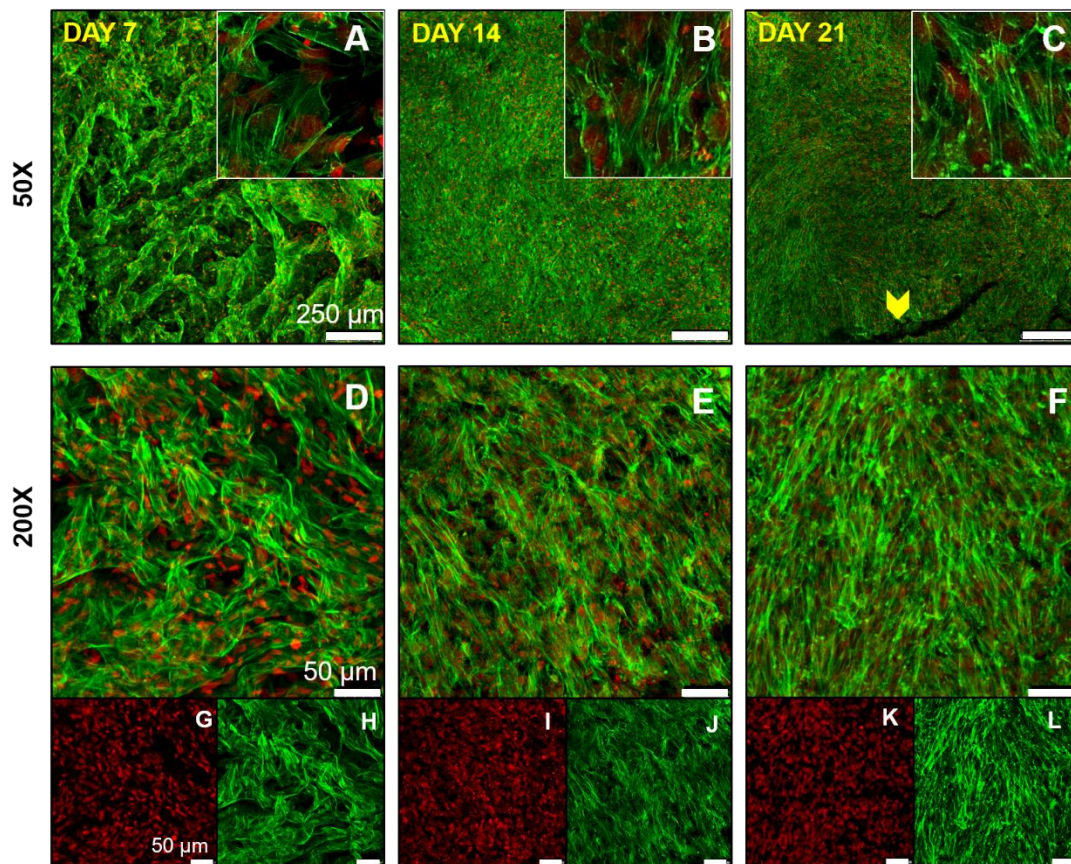


Figure 3.16. CLSM micrographs of the Saos-2 cells on collagen scaffolds. Merged images of the cytoskeleton and nucleus on (A, D) Day 7, (B, E) Day 14, (C, F) Day 21. (G, I, K) Images of cell nuclei and (H, J, L) the cytoskeleton on Day 7, 14, 21, respectively. Stains: Actin: Alexa Fluor 532 Phalloidin (green) and Nuclei: DRAQ5 (red). Cell seeding density = 1×10^5 /scaffold. (Yellow arrow head show crack in cell layer).

CLSM analysis was also performed on the horizontal cross sections of the Saos-2 seeded collagen scaffolds to determine whether Saos-2 cells migrated to the core of the scaffold (Figure 3.17). Cells are observed to be attached the walls of the pores at the inside of the sponge and spread.

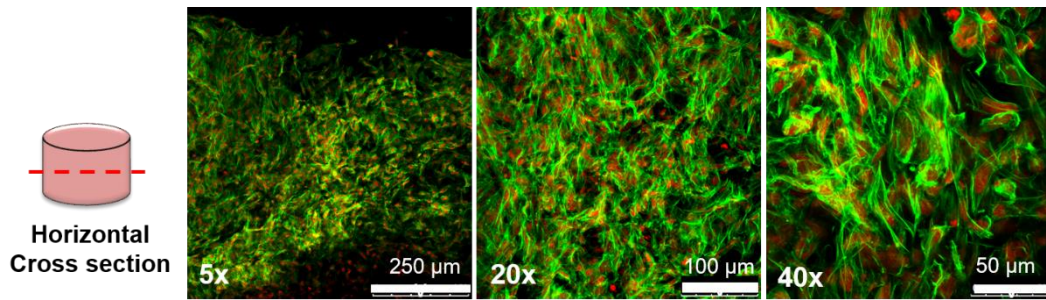


Figure 3.17. CLSM micrographs of a horizontal cross section of the collagen scaffolds showing the Saos-2 cells.

3.2.4. SEM Analysis

SEM micrographs of hFOB/HUVEC cells on the PLGA/TCP scaffolds are shown in Figure 3.18. Filamentous extensions (filopodia) that the cells use to attach the surface were observed on the micrographs. These extensions, which allow cells to attach to the surface as they grow and proliferate after adhering to a surface, are crucial in showing that cells and materials are interacting.

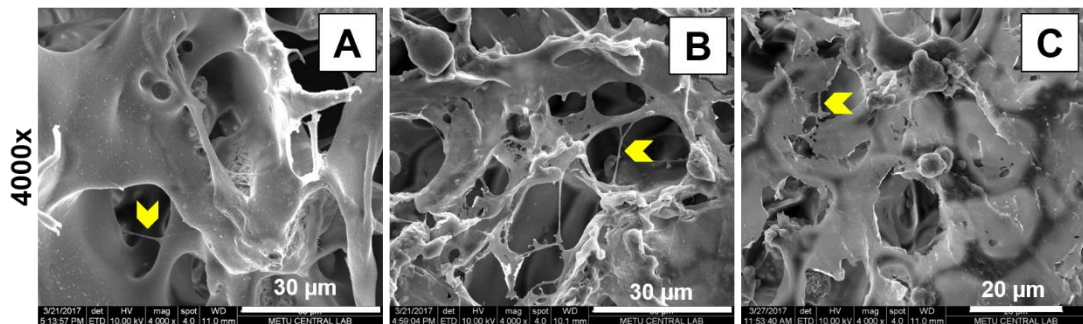


Figure 3.18. SEM micrographs of hFOB/HUVEC cells on PLGA/TCP scaffold. (A) Day 7, (B) Day 14, and (C) Day 21. Yellow arrow heads show filamentous cell extensions (filopodia).

SEM micrographs of Saos-2 cells on the collagen sponge are shown in Figure 3.19. On Day 7 (Figure 3.19A, 100x and 1000x magnification), the porous structure of the collagen sponges can be seen, over time the cells proliferated and began to fill the pores on Day 14 (Figure 3.19B, 100x and 1000x magnification). After 21 days, the entire sponge surface was covered with cells (Figure 3.19C, 100x and 1000x magnification). The yellow arrow heads show fine filamentous extensions of cells on high magnified images (4000x).

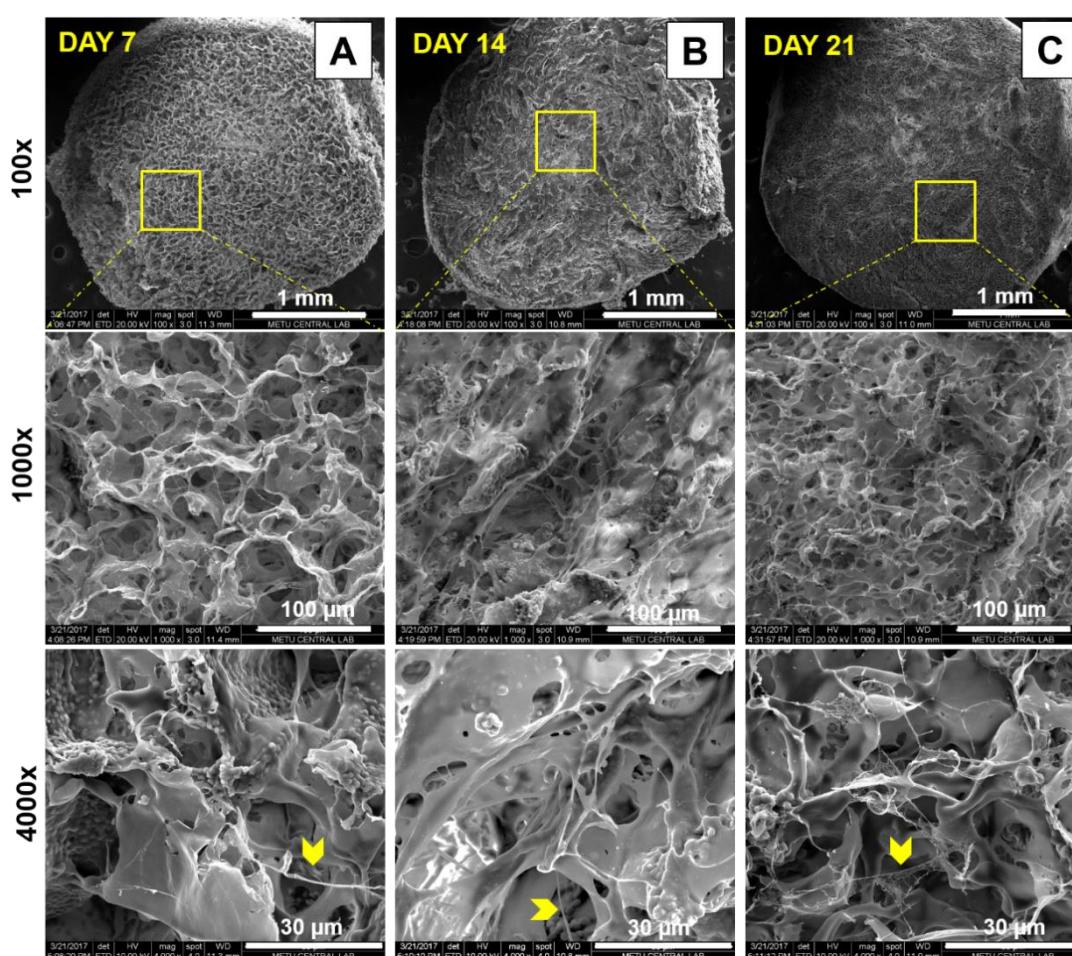


Figure 3.19. SEM micrographs of Saos-2 cells on collagen scaffold. Day (A) 7, (B) 14 and (C) 21. Yellow arrow heads indicate filamentous cell extensions (filopodia).

3.2.5. MicroCT Analysis

The effect of the cells on the internal structure of the PLGA/TCP scaffold such as mineralization of cells, changes in the scaffold porosity and cell proliferation over time were examined with microCT. MicroCT images of cell-free (control) and hFOB/HUVEC seeded PLGA/TCP scaffolds are shown in Figure 3.20. Calcium phosphate crystals produced by cells and TCP particles added during the scaffold preparation can be seen as white spots in microCT images.

Unseeded PLGA/TCP scaffolds had a porosity of 96.7% while the porosities of cell seeded sponges on Days 7, 14 and 21 were 89.6%, 90.2%, and 85.7%, respectively (Table 3.3). There is 11% decrease in the porosity of the cell seeded PLGA/TCP scaffolds after 3 weeks by comparison with the unseeded ones that probably the results of filling of the pores of the scaffold with the cells and deposition of calcium by the cells.

Table 3.3. Porosity of unseeded and cell seeded PLGA/TCP scaffolds.

Sample	Porosity
Unseeded PLGA/TCP Scaffold	96.7%
Cell Seeded PLGA/TCP Scaffold on Day 7	89.6%
Cell Seeded PLGA/TCP Scaffold on Day 14	90.2%
Cell Seeded PLGA/TCP Scaffold on Day 21	85.7%

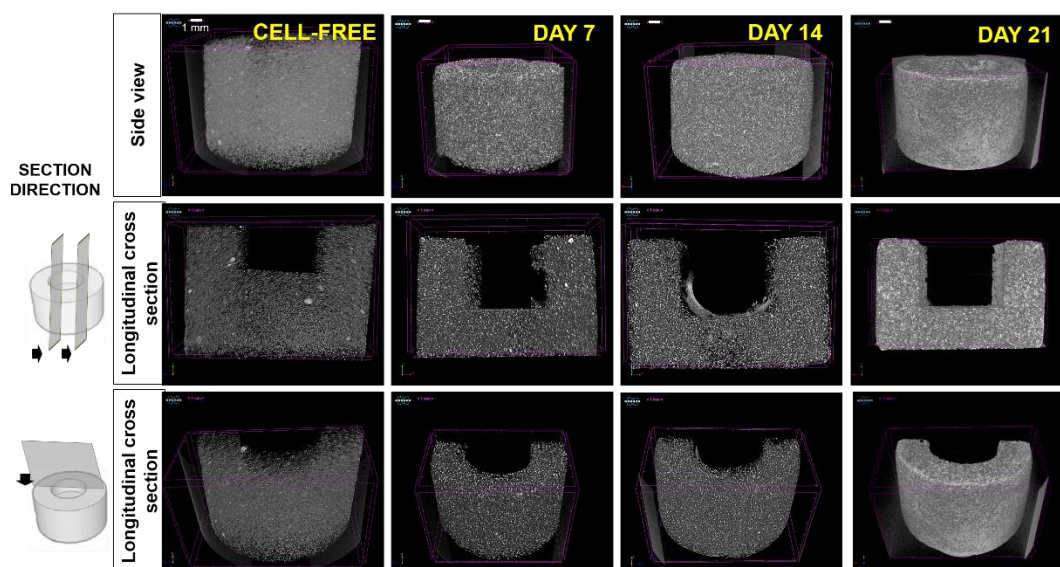


Figure 3.20. MicroCT images of cell-free and hFOB/HUVECs seeded PLGA/TCP scaffolds. The sectioning directions of the microCT images are shown in the leftmost column.

The X-ray absorption spectra of the horizontal cross sections of cell-free and hFOB/HUVECs seeded PLGA/TCP scaffolds were also analyzed (Figure 3.21). Left images show the horizontal sections of the scaffolds and right graphs show the X-ray absorption spectra that was taken along the red line. As the X-ray passes through the sample, it is absorbed if sample is radiopaque or it passes through the sample if sample is radiotransparent (Wu et al., 2015). When a sample absorbs X-ray, it gives peak in the X-ray absorption spectra as a grayscale value depends on the degree of opacity. Grayscale values change between 0 and 255 corresponds to black (air) and white (radiopaque material), respectively. Since the center of the scaffold is empty, there was no X-ray absorption, only small noise peaks were observed at this region. On the other hand, high peaks were seen at the scaffold due to the TCP particles in the scaffold and X-ray absorption increased in the cell seeded constructs on Day 21. It may probably due to calcium deposition by cells.

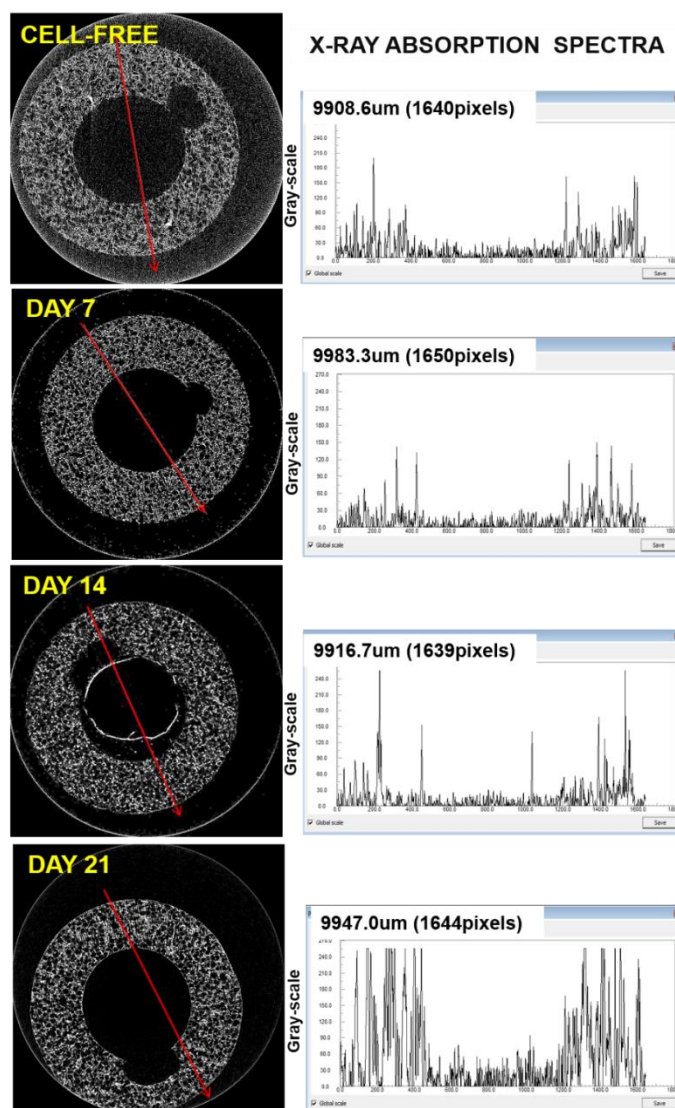


Figure 3.21. MicroCT images (Top View) and X-ray absorption spectra of the horizontal cross section of the cell-free and hFOB/HUVECs seeded PLGA/TCP scaffolds. The red lines show the direction in which the spectra are taken.

Calcium deposition by cells cannot be distinguished from images since the scaffolds also contain high amount of TCP particles (%20 w/w). ECM mineralization on scaffolds by cell was reported recently for X-ray translucent silk fibroin and polycaprolactone scaffolds (Hagenmüller et al., 2007; Porter et al., 2007; Peister et al., 2009; Peister et al., 2011). The transparent property of the polymer-based constructs

allowed to distinguish mineralized tissue from the scaffold. Since many scaffolds for bone tissue engineering are X-ray-opaque biomaterials, such as ceramics, a microCT that distinguishes the mineralized tissue from the biomaterials would be needed to analyze the development of bone-like tissue (Thimm et al., 2013). In the present study, the presence of high percent of TCP in the scaffold makes it relatively X-ray-opaque material and makes it difficult to examine the mineralized ECM by cells seeded within PLGA/TCP scaffolds.

The effects of cells on the internal structure of collagen scaffolds, calcium phosphate-forming capacities, changes in scaffold porosity were also examined for Saos-2 seeded collagen scaffolds with microCT. MicroCT images show the changes in the internal and external structure of unseeded and Saos-2 seeded collagen sponges (Figure 3.22). MicroCT images of the side view of the scaffolds showed that X-ray opacity increased during 3 weeks in cell seeded constructs. In the longitudinal and horizontal cross sections of the scaffolds, especially the outer edge of the scaffolds is brighter than the center of the sponges. These are the mineralized regions where cells mainly populated and generated mineralized ECM. Cell-free collagen sponge has a porosity of 86% and after cell seeding at the end of 7 days, it was decreased to 73%. Then, the porosity of the cell seeded collagen scaffolds dropped to 56% after 3 weeks. Since the Saos-2 cells are bone cells, they carry also calcium phosphate-forming properties, such as healthy bone cells (e.g., hFOB) (Bozycki et al., 2018). In cell seeded scaffolds, the increase of calcium phosphate formation due to cell proliferation over time decreases the porosity. Since collagen scaffolds are X-ray-translucent biomaterials, the mineralization by the cells can be easily distinguished with microCT images.

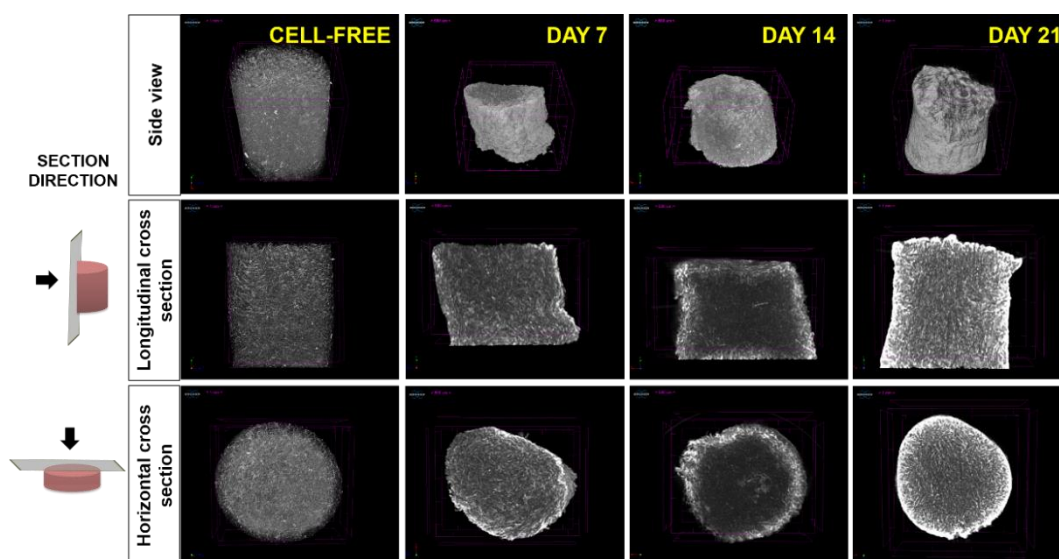


Figure 3.22. MicroCT images of cell-free and Saos-2 seeded on the DHT-CS. The section direction of the microCT images is given in the leftmost column.

X-ray absorption spectra of the horizontal cross section of the cell-free and Saos-2 seeded collagen scaffolds are shown in Figure 3.23. On the cell-free scaffolds, X-ray absorption peak heights through the scaffolds are similar showing homogenous pore distribution in the construct. The X-ray absorption values of cell seeded collagen scaffolds on Days 7 and 14 are at the highest level especially at the perimeter of the cylindrical collagen sponge and these regions were brighter where cell proliferated and formed cell clusters mostly. It can be related with the limitation of the oxygen and nutrient at the core of the scaffold and so cells colonized the exterior of the scaffold where there is no limitation of nutrient and oxygen. Brighter parts of images represent high X-ray absorption and so high gray-scale value. Cells located at the edge of the scaffolds deposit the calcium phosphate.

In cell seeded scaffolds, the increase of calcium phosphate formation due to cell proliferation over time and the increase of X-ray absorption of the samples were also supported by the CLSM micrographs of horizontal cross section of Saos-2 seeded collagen sponges (Figure 3.24) showing the similarity between the microCT and CLSM images of the section of the cell seeded scaffolds.

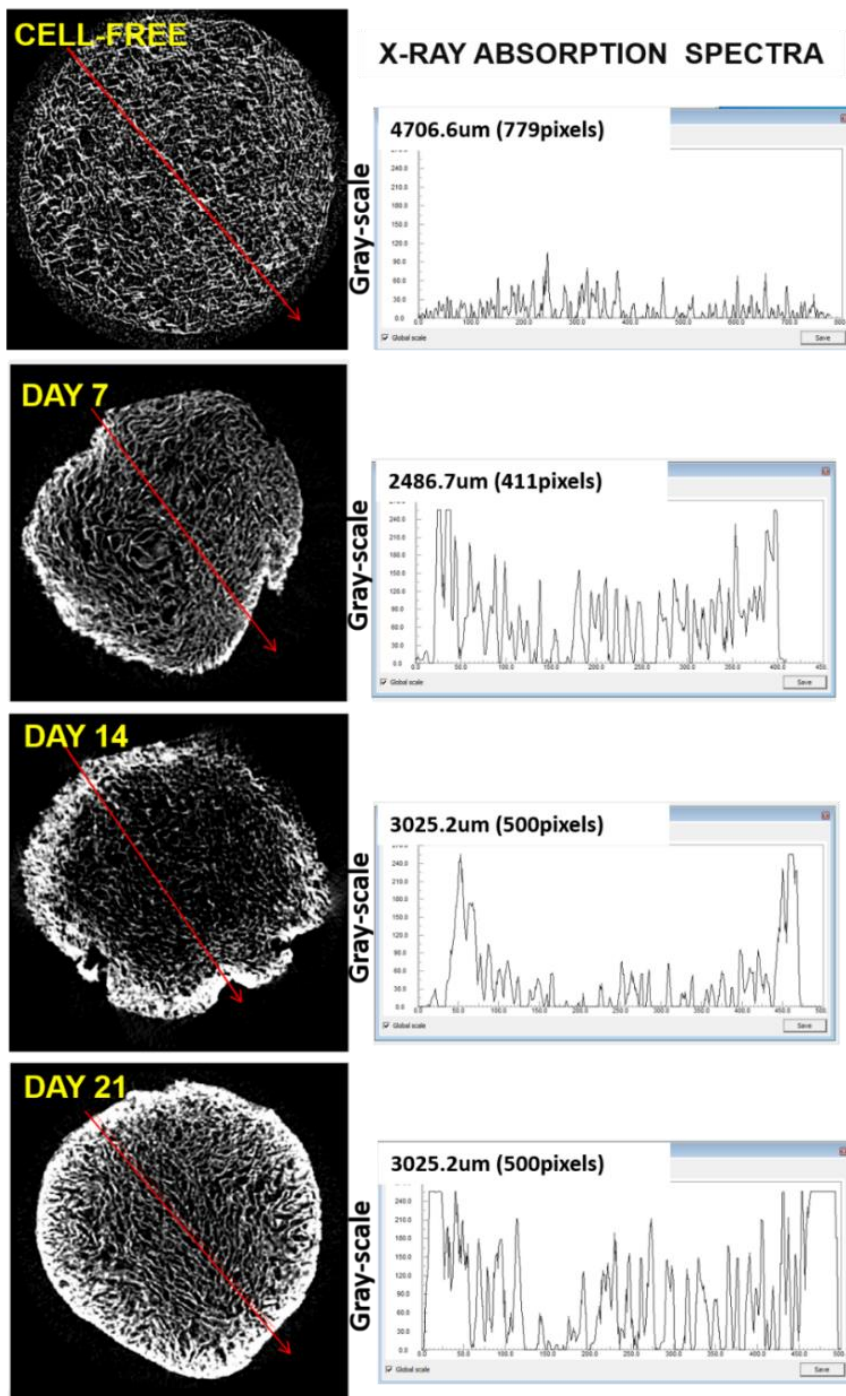


Figure 3.23. MicroCT images and X-ray absorption spectra of the horizontal cross section of the cell-free and Saos-2 seeded collagen scaffolds. The red lines show the direction in which the spectra are taken.

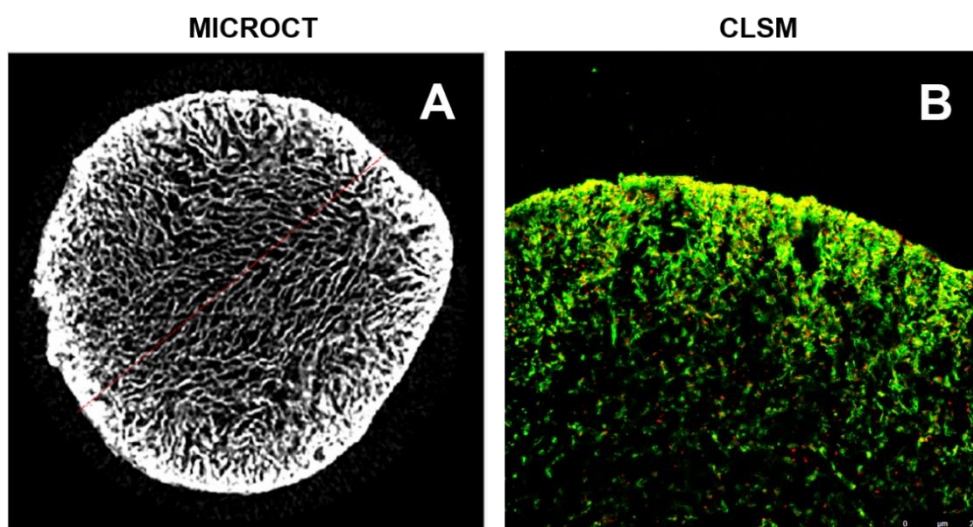


Figure 3.24. MicroCT and CLSM images of the Saos-2 seeded collagen scaffolds. (A) MicroCT and (B) CLSM image of horizontal section of the Saos-2 cell seeded scaffold on Day 21.

3.3. Characterization of the Complete Bone Tumor Model, BTM-S

3.3.1. Microscopy of BTM-S

The BTM-S is the combined structure of the tumor mimic and the surrounding healthy bone mimic. After inserting Saos-2 seeded collagen scaffolds (tumor mimic) in the cavity of hFOB/HUVEC seeded PLGA/TCP scaffolds (healthy bone mimic) and forming the complete bone tumor model, BTM-S, cells were co-cultured for 3 weeks. After that, the morphology, intercellular interaction and cell-material interactions were examined with CLSM (Figures 3.25A-H) and SEM (Figures 3.25I-L). In Figures 3.25A-D, cell nuclei and the cytoskeleton were stained and since these dyes were not specific to a certain cell type, cells of different types could not be distinguished from each other. Cells attached and spread on the wall of the pores of collagen scaffolds, attached and aligned on the PLGA/TCP scaffold and covered the surfaces by Day 21. Integration of cancer and healthy bone mimics did not affect the typical morphology and spreading of the cells. In Figures 3.25E-H, samples were stained with anti-von Willebrand factor (vWF) (red) and CD31 antibody (pink), dyes specific for HUVECs. Cytoskeleton (green) and nucleus (blue) of the cells of all three types of cells were

also stained. vWF is an adhesive glycoprotein that is synthesized, stored, and released from specialized secretory granules called Weibel-Palade (WP) bodies by endothelial cells (Kaufmann et al., 2000). Since HUVECs were seeded on the PLGA/TCP scaffolds before integration, the presence of HUVECs on the PLGA/TCP scaffold is an expected result (Figures 3.25G and 3.25H). Moreover, the observation of the HUVECs on collagen sponge interface and top surfaces of collagen (Figures 3.25E and 3.25F) indicated that HUVECs migrated towards collagen scaffold which is the tumor mimic. Spreading and coverage of the surface by hFOB, HUVECs and Saos-2 was observed also with SEM micrographs (Figures 3.25I-L).

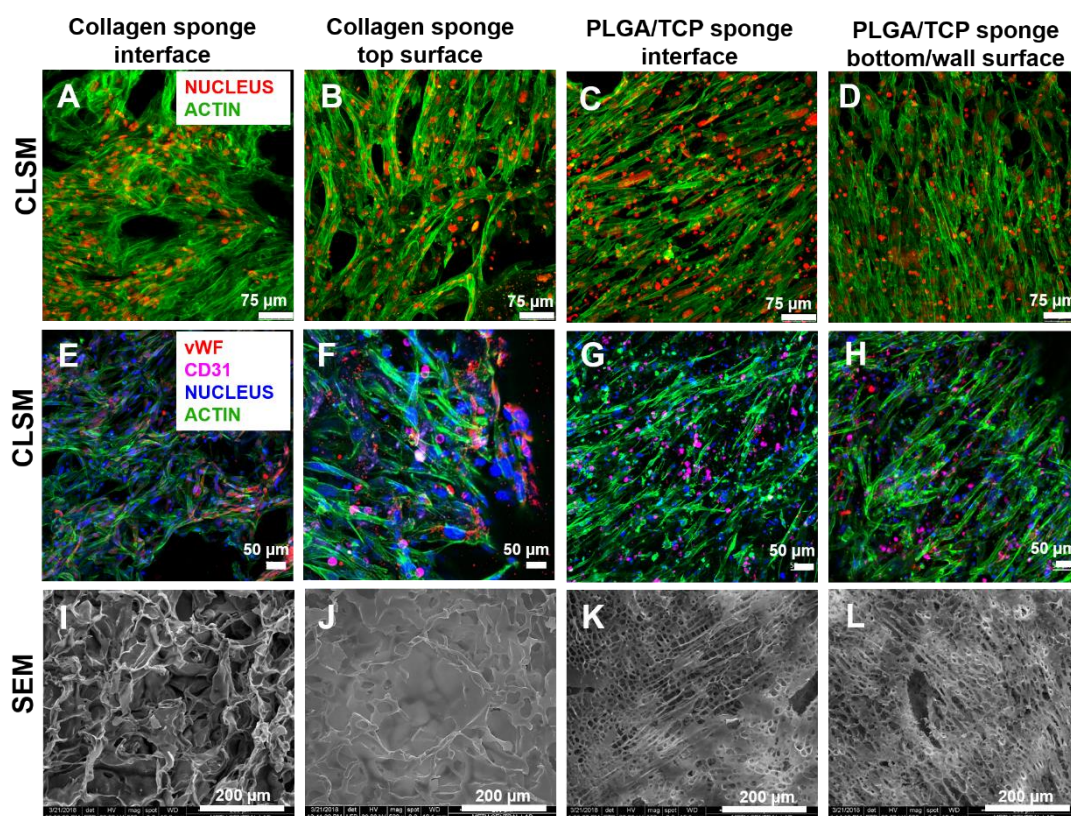


Figure 3.25. CLSM and SEM analysis of BTM-S. (A, B, C, D) CLSM micrographs of actin and nucleus staining, (E, F, G, H) antibody staining and (I, J, K, L) SEM micrographs of hFOB, HUVECs, and Saos-2 on PLGA/TCP and collagen scaffolds on Day 21. A-D Stains: Actin: Alexa Fluor 532 Phalloidin (green) and Nuclei: DRAQ5 (red). E-H Stains: Actin: Alexa Fluor 488 Phalloidin (green), Nuclei: DAPI (blue), CD31: anti-CD31 antibody (pink), vWF: anti-vWF antibody (red). CD31 and vWF stains HUVECs.

Horizontal sections of the BTM-S (Figures 3.26A-C) were stained to show the migration of HUVECs from the healthy bone mimic to the core of the tumor mimic. The interface of the tumor and the healthy bone mimics are shown with yellow dash lines. CD31 staining show only the HUVECs in BTM-S. Cells are homogeneously distributed throughout the section of the tumor mimic. Cells in the healthy bone mimic were mainly populated at the regions that have direct contact with cancer cells containing collagen core. HUVECs migrated into the collagen tumor mimic during the 21 day cell culture period (Figures 3.26B and 3.26C). There was physical contact between the two tissue mimics and this allowed endothelial cell migration.

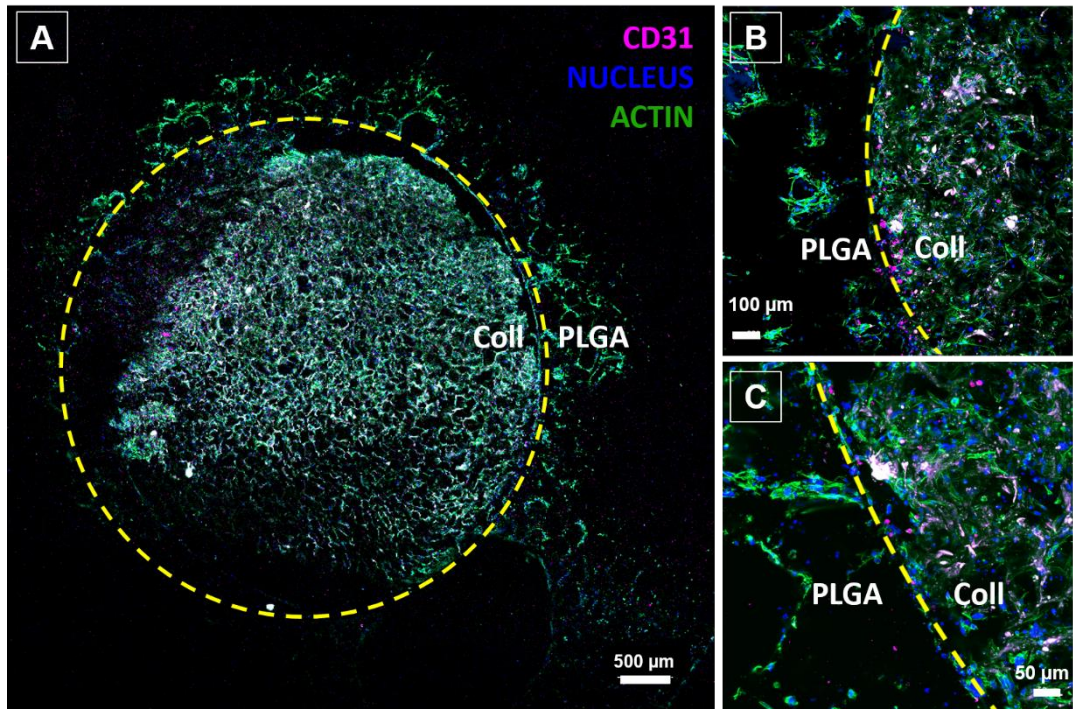


Figure 3.26. CLSM analysis of BTM-S. (A) CLSM micrographs of a total section of BTM-S on Day 21. (B, C) Magnified images of interface between healthy bone and tumor mimics in BTM-S. Stains: Actin: Alexa Fluor 488 Phalloidin (green), Nuclei: DAPI (blue), CD31: anti-CD31 antibody (pink). Yellow dash lines show the interface between healthy bone and tumor mimics.

The initiation of angiogenesis and the stimulation of tumor growth and invasiveness are crucial steps of metastasis and are directly related to interactions between tumor cells and their microenvironment. The importance of microenvironment in migration of endothelial cells was reported in a study (Tan et al., 2014). The authors reported that 3D co-culture of U2OS (osteosarcoma cell line) with fibroblasts resulted in significant upregulation of angiogenic factors (IL-8 and VEGF-A), which induced migration of HUVECs in a transwell system. Pietrovito et al. noted that cross-talk between bone marrow-derived mesenchymal stem cells (BMSCs) and osteosarcoma (OS) cells induce the secretion of pro-angiogenic factors in the tumor cells, and enhances both migration and invasion of HUVECs, and in addition, their ability to create tube-like structures (Pietrovito et al., 2018).

3.3.2. MicroCT

The effect of the Saos-2, hFOB, and HUVECs on the internal structure of the BTM-S such as calcium phosphate deposition and cell proliferation over time were studied with microCT. MicroCT images of horizontal cross section of BTM-S show the collagen-tumor mimic at the center of PLGA/TCP-healthy bone mimic with a direct contact (Figure 3.27). In cell-free sample, since the PLGA/TCP scaffold absorbs higher X-ray than the collagen, it seems brighter than the collagen construct. In cell seeded models, collagen part becomes brighter over time due to the mineralization by cells. On the other hand, there was no significant change in the X-ray absorption and so brightness in the healthy bone mimic (PLGA/TCP) since the scaffold contained a high amount of TCP particles (%20 w/w) and calcium phosphate produced by cells cannot be distinguished effectively.

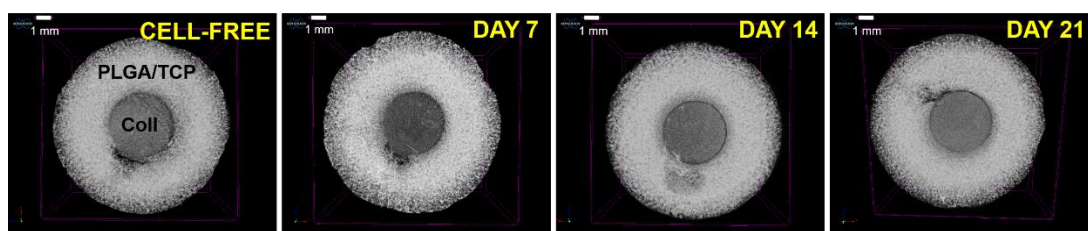


Figure 3.27. MicroCT images of a top view of the cell-free and cell seeded BTM-S on Days 7, 14, 21.

3.3.3. Molecular Analysis of Angiogenesis of BTM-S

Angiogenesis is well known for playing a critical role in tumor progression, aggressiveness, metastasis, and also resistance to cancer therapies. In this study, to better mimic tumor angiogenesis, we co-cultured HUVECs and hFOB in one scaffold with Saos-2 cells in another. Expression levels of angiogenic factors (VEGF, bFGF, and IL-8) by Saos-2 in the BTM-S were examined by real-time quantitative polymerase chain reaction (qRT-PCR) (Figure 3.28). In this analysis, three types of samples were used: Saos-2 cells cultured on 1) TCPS surfaces, 2) collagen sponges, and 3) collagen sponge of the complete bone tumor model. After the culture period, collagen sponges were removed from PLGA/TCP scaffolds, RNA isolated and qRT-PCR analysis was performed. Relative VEGF and bFGF gene expression levels are presented in Figures 3.28A and 3.28B. Gene expression level of Saos-2 cells cultured on TCPS served as a reference. There was no significant difference in VEGF expression by Saos-2 cells cultured in collagen scaffolds. However, on the collagen sponge of BTM-S, VEGF expression was significantly high on Day 7. Then, VEGF expression decreased on Day 14 and 21. Some studies reported that presence of bone mimic around the tumor tissue affected the expression level of VEGF, thereby the tumor progression supporting our results (Bachelder et al., 2001; Deckers et al., 2000). VEGF is known as a powerful angiogenic factor and generally believed that tumor cells can self-secrete VEGF to enhance the formation of its own vasculature (Peng et al., 2016). It stimulates the formation of new blood vessels and controls apoptosis and differentiation of tumor cells and osteoblasts. It has an effect on tumor progression

and pathological remodeling. However, the VEGF expression level decreased over time probably the results of a negative feedback mechanism of VEGF. As reported in some studies, there are some negative regulators that influence angiogenesis in an autocrine manner leading to downregulation of VEGF. Some of them are directly induced by stimulators of angiogenesis, especially VEGF, as a consequence of a specific negative-feedback regulator mechanism of angiogenesis (Coch et al., 2014; Lobov et al., 2007; Saito et al., 2013; Suzuki et al., 2010). These studies support the decrease of the VEGF expression by Saos-2 cells in BTM-S after reach the highest level on Day 7.

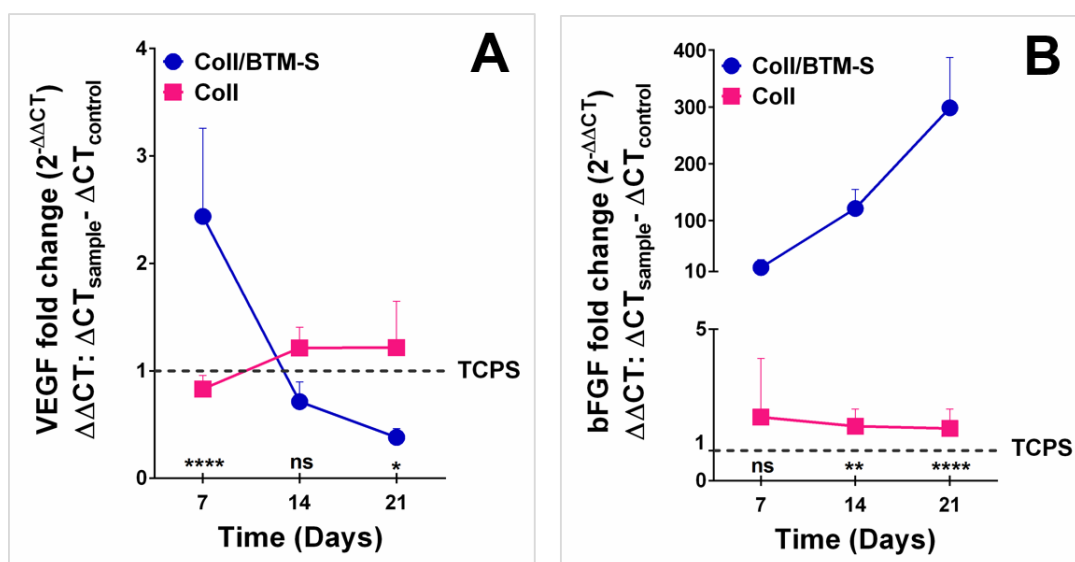


Figure 3.28. Analysis of VEGF and b-FGF secretion in the BTM-S. Relative expression levels of (A) VEGF and (B) bFGF genes of Saos-2 cells on collagen sponge (Coll) and collagen sponge in bone tumor model (Coll/BTM-S). TCPS served as a reference and accepted as 1. Statistical analysis between samples (Coll and Coll/BTM-S) was carried out using two-way ANOVA. * $p < 0.05$, ** $p < 0.01$, **** $p < 0.0001$, and ns: not significant.

There was also no significant difference in bFGF expression of Saos-2 cells in collagen sponge, however, for the Saos-2 cells cultured in BTM-S, these values were higher by approximately 10, 110 and 300 times on Days 7, 14 and 21, respectively. This high level increase is probably an effect of hFOB and HUVECs caused by cross-talk within the model. This result also supported the CLSM analysis of BTM-S showing HUVECs migration toward tumor mimics probably induced by angiogenic factors secretion by Saos-2 cells in BTM-S.

IL-8 has some critical effects on angiogenic, migratory, and osteoclastogenic activities. Many cancerous cell types express IL-8 which result in proliferation and migration of cancer cells, tumor angiogenesis and metastasis. Researchers have shown that highly metastatic solid tumors express significant amounts of IL-8 (Ning et al., 2011). In this study, relative IL-8 gene expressions between samples could not be calculated because IL-8 gene expression levels of Saos-2 on TCPS surface and collagen sponge were too low for qRT-PCR. For this reason, the expression of IL-8 gene in BTM-S was shown by agarose gel electrophoresis (Figure 3.29). Agarose gel micrographs showed the expression of the GAPDH control gene (housekeeping gene) and IL-8 gene in three samples as bands. IL-8 expression of Saos-2 in the BTM-S was significantly increased on Days 7, 14 and 21. Co-culture of Saos-2 in close vicinity of hFOB and HUVECs in the microenvironment of the tumor tissue mimic significantly upregulated the IL-8 expression. This was also noted in a study where they found that co-culture of U2OS osteosarcoma cells with immortalized fibroblasts resulted in the upregulation of angiogenic factors (VEGF, IL-8, bFGF), especially IL-8 (Tan et al., 2014).

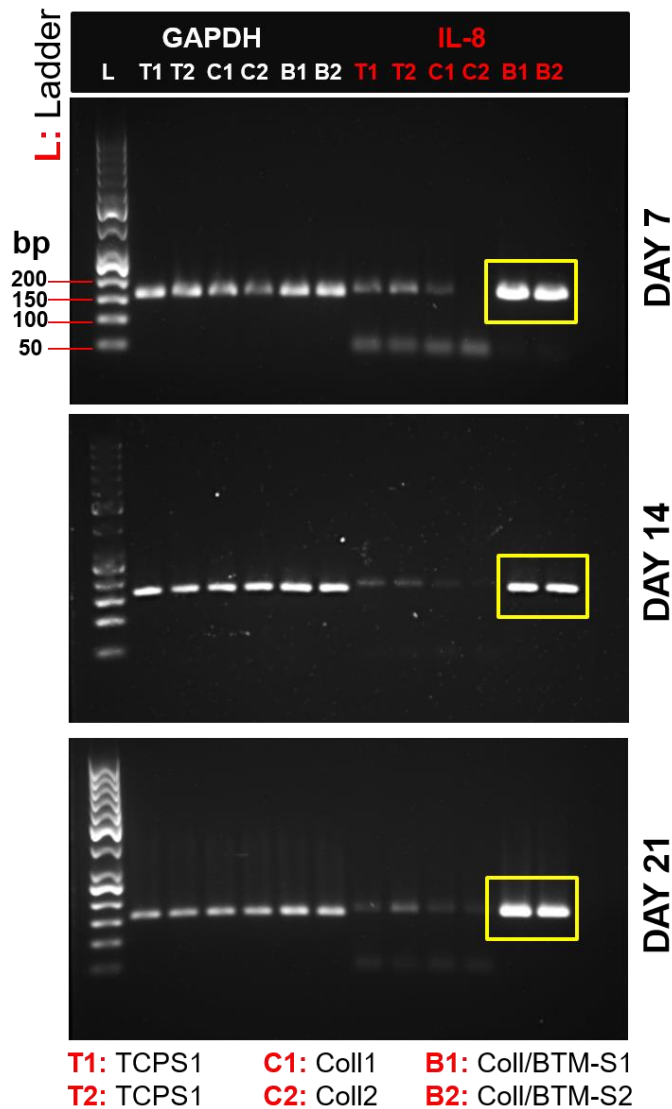


Figure 3.29. Agarose gel electrophoresis of IL-8 genes of Saos-2 cells on TCPS surface (TCPS), collagen sponge (Coll) and collagen sponge in bone tumor model (Coll/BTM-S) on Days 7, 14 and 21. Yellow rectangles show the cDNA bands corresponding to IL-8 mRNA of Saos-2 in Coll/BTM-S.

There are several studies in which cancer cells were co-cultured with vascular cells in the natural matrix to develop a model of tumor angiogenesis. In one such study, HUVECs were cultured on collagen gels containing oral squamous carcinoma cells. HUVECs initiated different degrees of invasion and migration. This behavior of endothelial cells was induced by secretion of the angiogenic growth factors IL-8 and

VEGF by cancer cells (Verbridge et al., 2010). In another study, the importance of tumor microenvironment was shown in a model where tumor cell spheroids were cultured in a bone tissue environment consisting of human mesenchymal stem cells in decellularized bone matrix. Their results demonstrated that cancer cells re-expressed focal adhesion and cancer-related genes that are highly expressed in tumors but lost in monolayer cultures and gained angiogenic capacity that favor tumor initiation and progression (Villasante et al., 2014).

In the present study, analysis of angiogenesis together with CLSM examination showed that HUVEC migrated toward the tumor mimic as a result of angiogenic factor secretion by Saos-2 cells in BTM-S. We developed a model where angiogenesis and especially the migration ability of endothelial cells into the tumor could be mimicked without addition of cytokines.

3.4. Characterization of Bone Tumor Models, BTM-SS and BTM-G

In BTM-S model, Saos-2 cells attached, spread well and proliferated on the collagen sponge and no cell clusters were observed. Since they grew throughout the scaffold, it was suitable in the generation of a tumor mimic. However, we also planned to compare a tumor mimic composed of aggregated cells as in a spheroid knowing that spheroids closely mimic tumor structure. For this purpose, Saos-2 spheroids were produced, seeded on collagen sponge to form the tumor mimic part of BTM-SS. In another model, spheroids were entrapped in GelMA hydrogels to form the tumor mimic part of BTM-G. Both models had the PLGA/TCP healthy bone mimic surrounding the tumor.

3.4.1. Characterization of Saos-2 Spheroids

3.4.1.1. Morphology of Saos-2 Spheroids

Saos-2 spheroids were prepared by culturing Saos-2 cells on ultralow attachment cell culture plates. Cells could not attach the plate surface and formed cell clusters that grew and formed the spheroids. Figure 3.30 shows the light microscopy images of the spheroids with different morphology and size at different culture times. Spheroid sizes and complexity are generally determined by proliferation rates of the cells, cell density during seeding, duration of culture and tightness of cell-cell interactions within the cellular aggregates (Schmidt et al., 2016).

On Day 7, cells aggregated into loose, irregular shaped clusters surrounded by nonaggregated cells that differed in size and tightness. On Day 40, tight, well-shaped spheroids with smooth surfaces were formed. In the image, darkest region of the spheroid represents mainly quiescent or dead cells (Hirschhaeuser et al., 2010). Since spheroid size can influence the reproducibility of the assays, it is important to create spheroids of uniform size and cell numbers for biochemical analysis and high-throughput screening. In the present study, a group of spheroids were generated in an ultra-low attachment 6-well plate, so the size of the spheroids was not uniform (Figure 3.30).

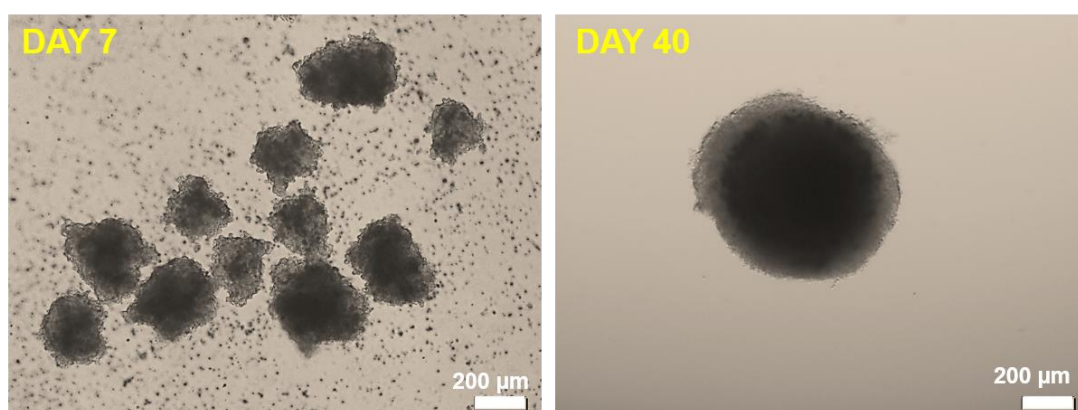


Figure 3.30. Light microscopy images of Saos-2 spheroids on Day 7 and Day 40.

3.4.1.2. Live/Dead Assay of Saos-2 Spheroids

Live/Dead assay was performed to show cell viability in the spheroids on Day 25 (Figure 3.31). Calcein AM (green) stains viable cells, and ethidium homodimer-1 (red) stains nonviable cells. Spheroids are composed of mostly live cells, with minimal dead cells. While most live cells were located on the exterior part of the spheroids, dead cells were observed at the core, far from the nutrients and oxygen. Spheroids have limitations in the diffusion of drugs, nutrients, and other factors and can generate necrotic cores and hypoxia regions (Chaddad et al., 2017) as observed in the present study.

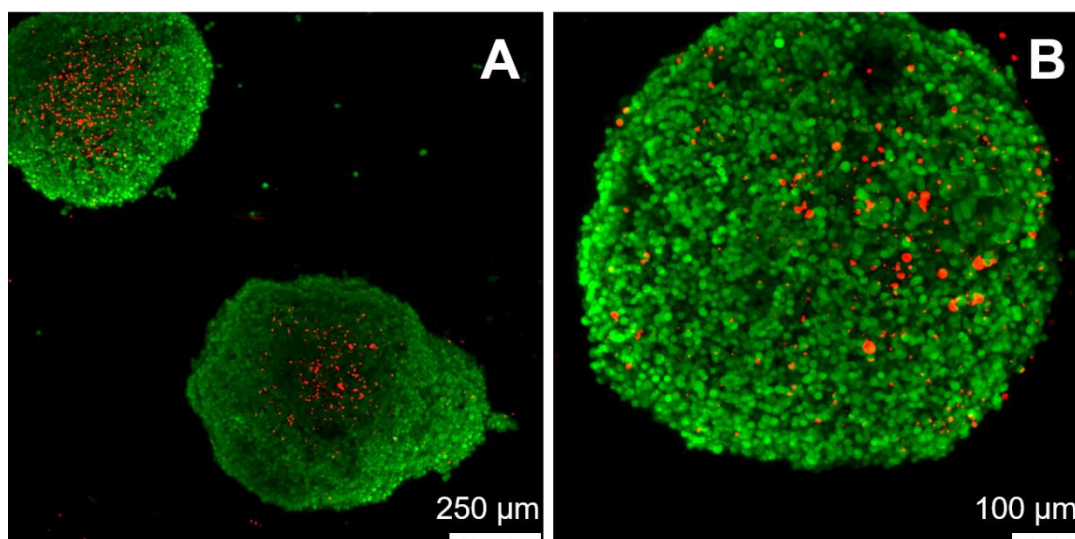


Figure 3.31. Cell viability assays of Saos-2 spheroids using Live/Dead staining on Day 25. (A, B) CLSM micrographs of stained Saos-2 cells spheroids. Calcein AM (green) viable cells; ethidium homodimer-1 (red) nonviable cells.

Tumor spheroids have several unique properties. They have chemical gradients of oxygen, nutrients, and catabolites at diameters beginning from 200 µm and create a necrotic area at the core when the diameter exceeds 500 µm. The diameter of the spheroids prepared in the present study was measured to be approximately 667 µm on Day 25 by using ImageJ (NIH, USA). Cells in spheroid exterior are like actively

proliferating tumor cells *in vivo* located close to capillaries while innermost cells are quiescent and ultimately die with apoptosis or necrosis.

Figure 3.32 shows a scheme with the location of proliferating, quiescent and dead cells in a spheroid. According to this, nutrient, oxygen concentration, ATP debris, carbon dioxide concentration, and acidosis affect the viability of the cells (Zanoni et al., 2016).

Since the size of the present spheroids is larger than 250 μm , and that is a maximum distance for cells to achieve healthy oxygen and nutrient transfer, a necrotic core formed at the center of the spheroids. The live-dead cell distribution profile in the spheroids was expected and desired because a typical tumor tissue also shows this organization. This was also observed by other studies (Charoen et al., 2014; Oliveira et al., 2014).

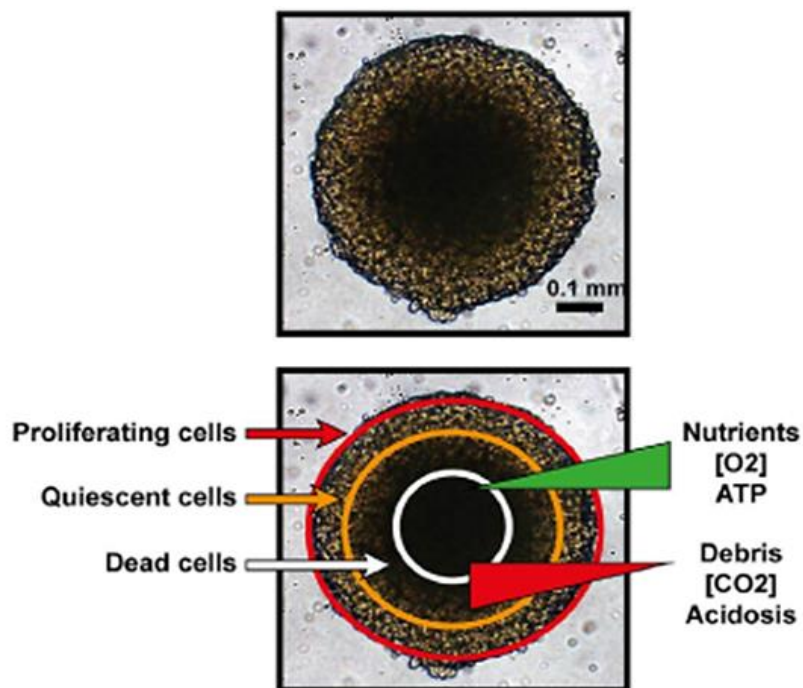


Figure 3.32. Bright field microscopy image of cell spheroid (top) and the same image with pathophysiological gradients (bottom) (Zanoni et al., 2016).

3.4.1.3. SEM Analysis of Saos-2 Spheroids

The morphology of spheroids was investigated by using SEM (Figure 3.33) that enabled a more detailed evaluation. Spherical morphology of the spheroids is seen to show the generated shape and the close-up. Tight, well-shaped spheroids with a rough surface was observed. At higher magnifications, the formation of many filopodia could be observed and these show good cell-cell interactions.

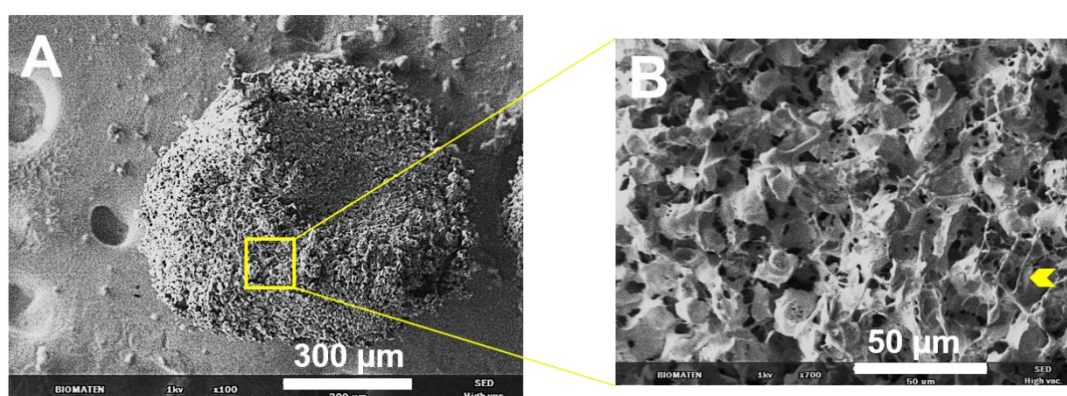


Figure 3.33. SEM of Saos-2 spheroids.

3.4.2. Quantification of Cell Numbers in BTM-SS

Alamar Blue assay was performed on BTM-SS consisting of Saos-2 spheroids cultured within collagen scaffold inserted into hFOB/HUVEC seeded PLGA/TCP scaffold. Approximately 3-4 spheroids were seeded on each collagen sponge while a total of 2×10^5 hFOB:HUVEC (1:1) were seeded on each PLGA/TCP scaffold. The Alamar Blue test results show that on Day 7, the number of cells is very low (approximately 5×10^4). Still, the number of cells in the BTM-SS significantly increased during the next 2 weeks (Figure 3.34A).

DNA quantification test was also performed to determine the proliferation of cells in the BTM-SS. The number of cells was calculated from the amount DNA (Figure

3.34B). 1.8×10^6 cells were counted on Day 7 and cell number further increased after 3 weeks of culture. This result demonstrated that the culturing of three types of cells did not affect the cell metabolism and cells proliferated over time showing the success of the model.

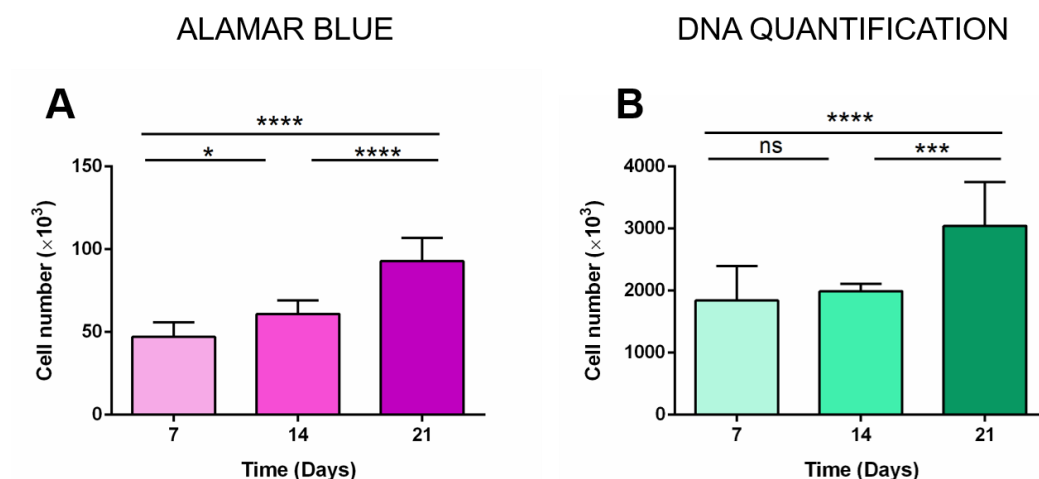


Figure 3.34. Cell (Saos-2 + hFOB + HUVEC) proliferation in the BTM-SS. (A) Alamar Blue assay, and (B) DNA quantification assay results. Statistical analysis of the counts was carried out using two-way ANOVA. * $p < 0.05$, **** $p < 0.0001$, and ns: not significant.

3.4.3. Live/Dead Assay of BTM-SS

Live/Dead cell viability staining was performed on BTM-SS on Day 21. CLSM micrographs revealed high cell viability on collagen sponge top and a bottom surface and PLGA/TCP sponge bottom surface (Figure 3.35). There were no toxic effects of the scaffolds on the cells. This means that collagen and PLGA/TCP scaffold components of the model support survival of the three cell types used in this study.

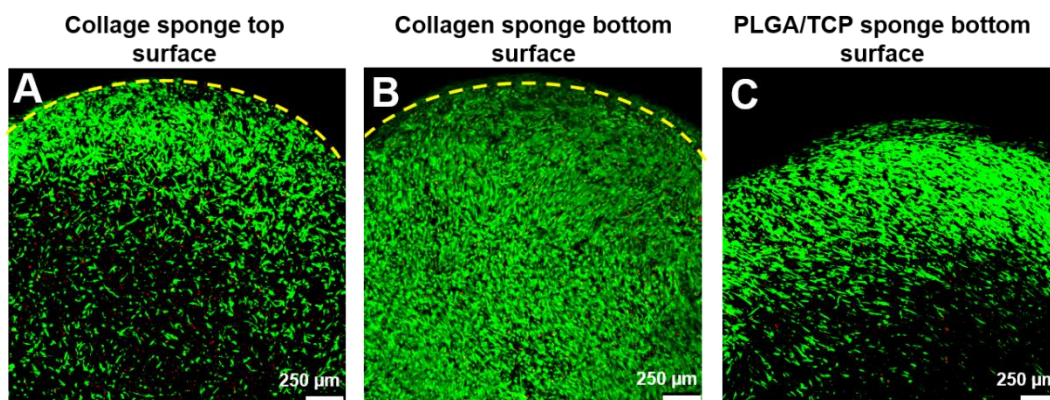


Figure 3.35. CLSM micrographs of Live/Dead assay of the BTM-SS. (A) Collagen sponge top surface, (B) collagen bottom surface, and (C) PLGA/TCP sponge bottom surface. Day 21. Live cells: calcein AM (green) and dead cells: ethidium homodimer-1 (red). Yellow dash lines show the collagen sponge boundary.

3.4.4. Alkaline Phosphatase (ALP) Activity of Cells in BTM-SS

ALP activity of hFOB and Saos-2 spheroids in the BTM-SS was studied by using the ALP assay kit for 21 days. The results were normalized with the cell number. For this reason, determination of ALP activity and the number of cells by measuring the amount of DNA were performed simultaneously (Figure 3.36). ALP activity was almost constant on Days 7 and 14, but decreased on Day 21. ALP is an early marker for the osteoblast phenotype, is up-regulated at the beginning of differentiation and then decrease as differentiation continues. Since differentiation medium was not used for hFOB cells, these cells are not expected to contribute to an increase in ALP activity.

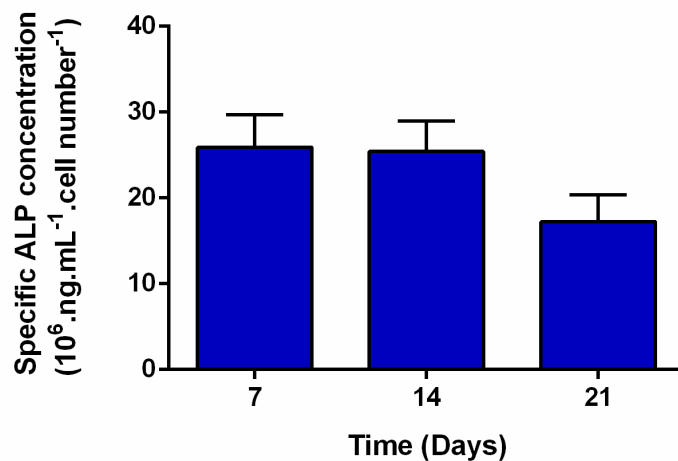


Figure 3.36. Total ALP activities of hFOB and Saos-2 spheroids in the BTM-SS. ALP activities were normalized by dividing by the number of cells obtained from DNA quantification assay.

3.4.5. MicroCT Analysis of BTM-SS

MicroCT images of cell-free and cell seeded BTM-SS are shown in Figure 3.37. A gap was formed after freeze drying between the two scaffolds. This was later solved by increasing the diameter of collagen scaffold to achieve the direct contact between the constructs. Change in the brightness of cell seeded constructs were not be observed over time. This also supported with X-ray absorption spectra of the horizontal section of cell-free and cell seeded BTM-SS (Figure 3.38). The expected change in X-ray absorption due to produced calcium phosphate could not be observed maybe because the amount was very low. Since the number of Saos-2 spheroids seeded on the collagen sponge was low this might be the reason for the low contribution of cells to X-ray opaque regions.

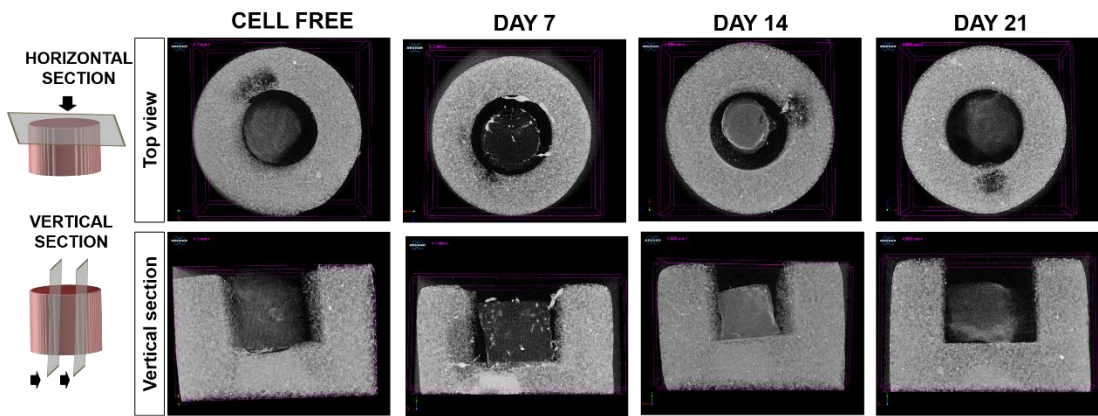


Figure 3.37. MicroCT images of the cell-free and cell seeded BTM-SS (PLGA/TCP sponge+collagen sponge) on Days 7, 14, 21.

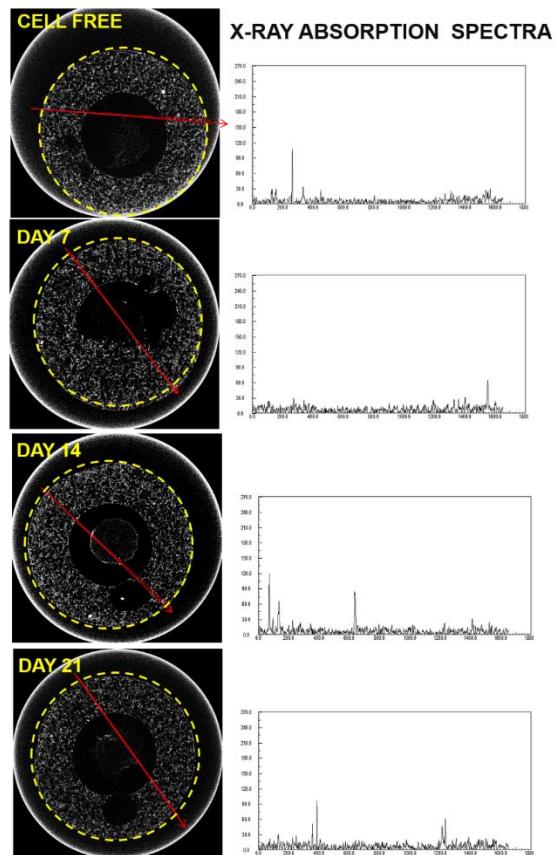


Figure 3.38. MicroCT images (top view) and X-ray absorption spectra of the horizontal section of the cell-free and cell seeded BTM-SS (PLGA/TCP sponge+collagen sponge) on Days 7, 14, and 21. The red lines show X-ray absorption measurement axis. Yellow dashed lines show the outer limit of the PLGA/TCP sponge.

3.4.6. Immunocytochemistry of BTM-SS and BTM-G

CLSM micrographs of the hFOB, HUVECs, Saos-2 cells and spheroids in the BTM-SS on Days 7 and 21 are shown in Figure 3.39. Collagen sponges were removed from PLGA and then the constructs were visualized separately. The cell types could not be distinguished because no cell specific dye was used. The spheroids are seen to be round shaped on Day 7 (Figures 3.39A1 and 3.39A2). Saos-2 cells detached from the spheroid, appear to have spread, proliferated and completely covered the surface of the collagen sponge like a cell sheet (Day 21). On the bottom surface of collagen, cells generally were attached and grew at the edges of the scaffold (Figure 3.39A3 and 3.39B3) probably to have access to the nutrients and oxygen. On the bottom surface of PLGA/TCP sponge, hFOB and HUVECs covered the entire surface (Figures 3.39A4 and 3.39B4). The detachment of the cells was not the desired result since the aim was to preserve the spheroidal morphology. In a study, a similar result was seen when glioma cells spheroids were seeded on the collagen-coated PLGA scaffolds to prepare a 3D tumor model (Ho et al., 2010). They observed that spheroids attached well within the pores of the scaffold and over time, cells detached from the spheroid, spread and proliferated on the scaffold as in a monolayer culture. They reported that the spheroids were in spherical morphology on Day 2, but most were disintegrated on Day 4, as was the case in the present study on Day 7.

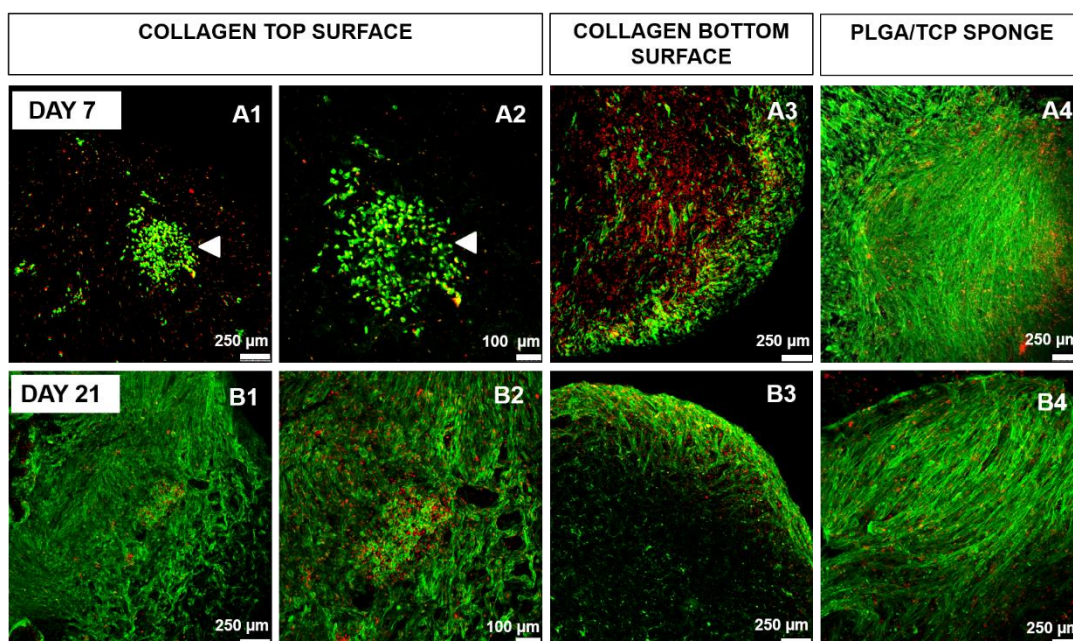


Figure 3.39. CLSM micrographs of hFOB, HUVECs, Saos-2 cells and spheroids in the BTM-SS on Days 7 and 21. CLSM micrographs of the top surface of the Saos-2 spheroid cultured collagen sponge at (A1, B1) 5x and (A2, B2) 10x magnification. (A3, B3) CLSM micrographs of the bottom surface of the Saos-2 spheroid cultured collagen sponge. (A4, B4) CLSM micrographs of hFOB/HUVEC co-cultured on PLGA/TCP sponges. Stains: Actin: Alexa Fluor 532 Phalloidin (green) and Nuclei: DRAQ5 (red). White arrow heads indicate the spheroid.

Saos-2 spheroids cultured on collagen sponge did not preserve their spherical morphology over time, disintegrated and spread on the surface of the sponge. We concluded that collagen sponges were not suitable for culturing spheroids.

Since we aimed to form Saos-2 spheroids that can preserve their integrity, the spheroids were loaded in methacrylated gelatin (GelMA) hydrogels. GelMA was chosen due to its high water content and biocompatibility. Figure 3.40 shows CLSM micrographs of spheroids entrapped into GelMA hydrogels on Day 21. Unlike in collagen sponge, spheroids maintained their morphology for three weeks. Highly hydrophilic nature of the hydrogel prevented the detachment of cells from the spheroid and caused them to stay attached to the neighboring cells. In the previous case, collagen sponge with cell attachment motifs were suitable for the attachment of the cells and the cells attached to the collagen sponge rather than forming aggregates. The

suitability of the hydrogels in the culture of spheroids were also supported by other studies which show the success of the loading the spheroids or the cells intended to generate spheroid in hydrogels. These studies include encapsulation of liver tumor spheroids in collagen hydrogels (Liang et al., 2011), hepatocyte spheroids in heparin-based hydrogels (Kim et al., 2010), prostate cancer cells in hyaluronic acid hydrogels to form spheroids (Xu et al., 2012), hepatocarcinoma cell spheroids in alginate hydrogels (Lee et al., 2011), osteoinduced MSC spheroids in alginate hydrogels (Ho et al., 2017), osteosarcoma and breast adenocarcinoma cell spheroids in collagen hydrogels (Charoen et al., 2014). All these studies showed the suitability of culturing spheroids inside the hydrogels since tumor spheroids are very prone to dissociation during handling and analysis, and also cultural conditions (such as the presence of ECM, cell-matrix interactions, mechanical stiffness) in tumor spheroids cannot be regulated (Pradhan et al., 2017).

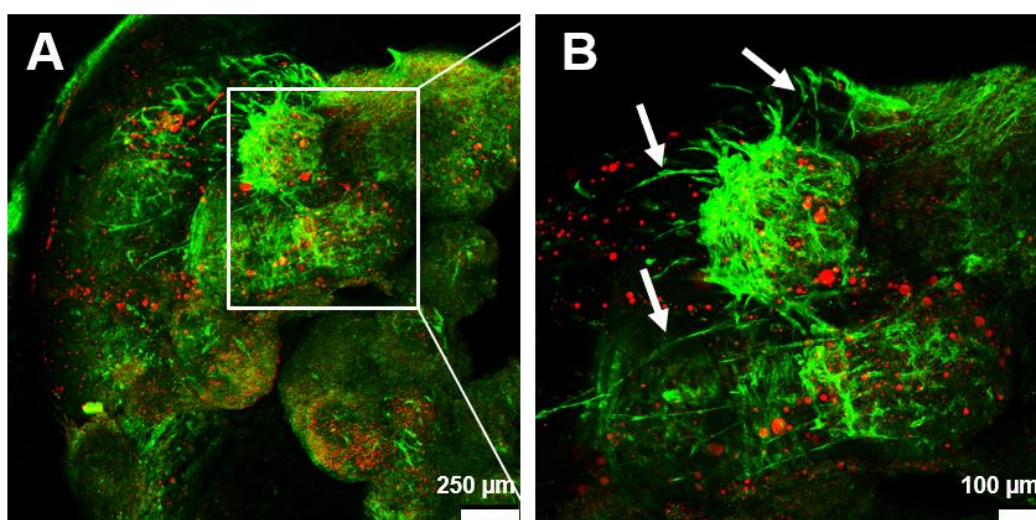


Figure 3.40. CLSM micrographs of BTM-G generated by encapsulating of Saos-2 spheroids in GelMA hydrogel (Day 21). Stains: Actin: Alexa Fluor 532 Phalloidin (green) and Nuclei: DRAQ5 (red).

Immunostaining with anti-human CD31 was performed to show HUVECs in the BTM-SS and BTM-G after taking horizontal sections of the 3D models with cryomicrotome. By using mosaic image capture mode of a fluorescence microscope, the entire image of the 10 mm-wide sections of the models could be obtained. Fluorescence micrographs of BTM-SS show that size of the collagen sponge decreased during incubation while there was no size change in the PLGA/TCP sponge: this created a gap between two tissue mimics (Figure 3.41A). Saos-2 spheroids (and hFOB and HUVECs which may come from PLGA/TCP sponge) spread well in the BTM-SS due to the highly porous internal structure and cell attachment properties of the collagen sponges (Figure 3.41C and 3.41E).

Figure 3.41B shows fluorescence micrographs of BTM-G where spheroids were entrapped in the hydrogel. The hydrogel is not visible but the spheroids are visible. The white arrow head in Figure 3.41D and 3.41F show the contact region between the two parts. The spheroids preserved their spherical morphology instead of disintegrating and spreading. Vascular-like structures can be seen in Figure 3.41F (white arrows), as was seen in Figure 3.40B (white arrows). The formation of vessel-like network structures may be due to the factors released by Saos-2 cells and the hypoxic core of the Saos-2 spheroids that attract the endothelial cells and induce angiogenesis. Similar observations were made by others. Chaddad et al. cultured osteosarcoma cell spheroids on the HUVECs monolayer. They stated that hypoxic core of spheroids induced the secretion of VEGF, which attracted endothelial cells to the spheroid tumor and enhanced formation of vessel-like structures and organization of a vascular network (Chaddad et al., 2017). In other study, spheroids were seeded in the porous polyurethane scaffolds and implanted to a mice to initiate vascularization through the scaffold. They used the spheroids as a potent initiator of blood vessel formation by taking advantage of the hypoxic region in the spheroid and showed that vascularization increased in scaffolds seeded with spheroid by comparing with scaffolds seeded with individual cells (Laschke et al., 2013).

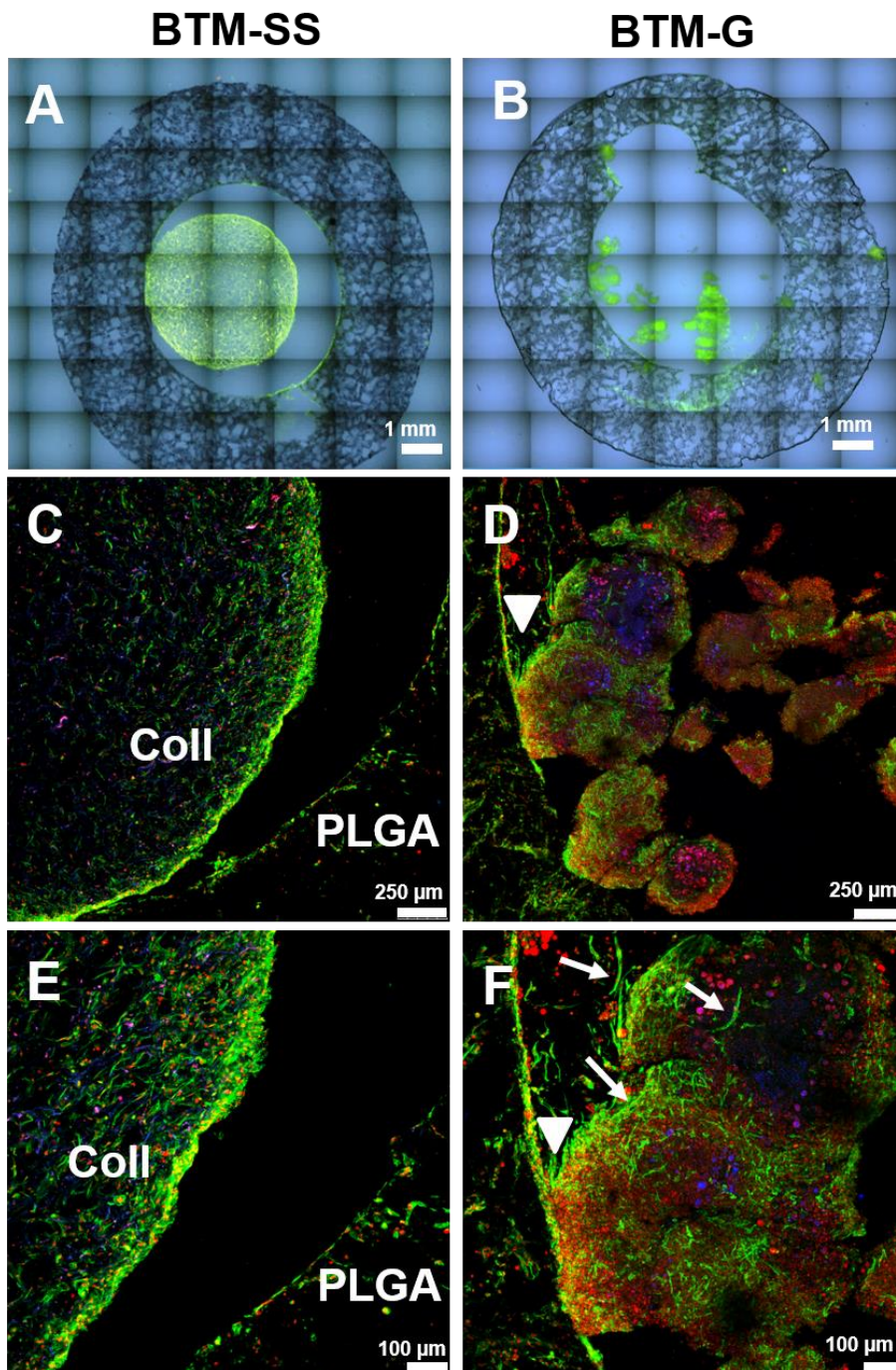


Figure 3.41. Microscopy analysis of Saos-2 spheroids containing BTM-SS and BTM-G on Day 21. (A, B) Fluorescence micrographs of the complete section of the models. CLSM micrographs of horizontal sections of (C, E) BTM-SS and (D, F) BTM-G. White arrow heads show the interface between the spheroid loaded hydrogel and PLGA/TCP sponge. Stains: Actin: Alexa Fluor 532 Phalloidin (green), Nuclei: DRAQ5 (red), CD31: Alexa Fluor 488 labelled CD31 (blue).

3.4.7. SEM of BTM-SS and BTM-G

SEM micrographs of BTM-SS are given in Figure 3.42. Before SEM analysis, collagen sponges were removed from the cylindrical cavity of healthy bone mimic and SEM analysis was carried out. The spheroids were not seen on the collagen sponge since they disintegrated and the cells released from the spheroids attached and spread on the collagen sponge. In high magnification images (insets), yellow arrow heads show the cells' extensions which demonstrate the presence of good cell-material interaction. On both the PLGA/TCP and collagen scaffolds, which together constitute BTM-SS, cells spread well and covered the surface of the scaffold over time.

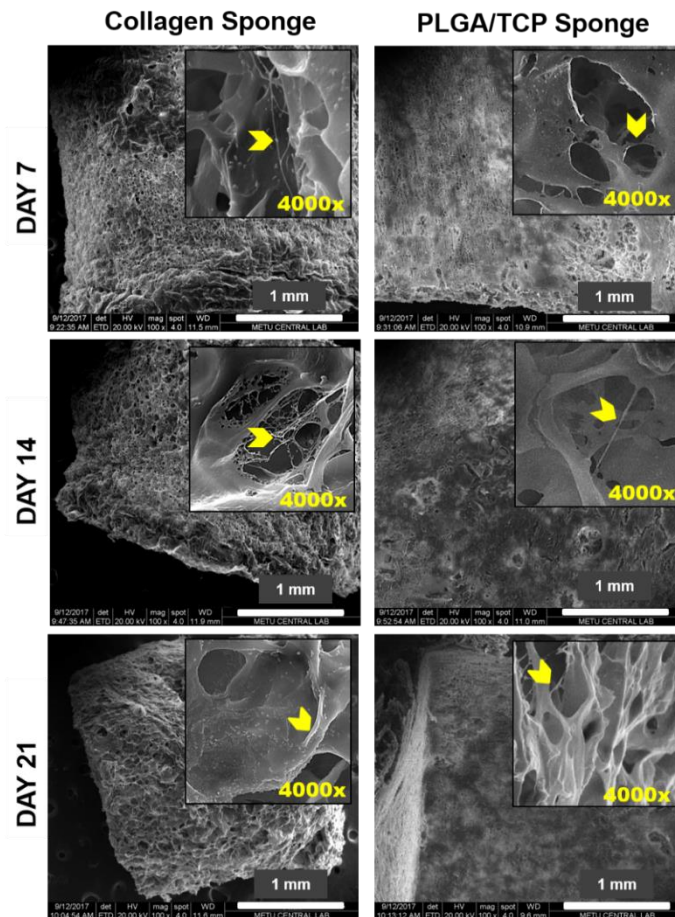


Figure 3.42. SEM micrographs of BTM-SS on Days 7, 14, and 21. Yellow arrow heads show filamentous cell extensions (filopodia) indicating satisfactory cell-material interactions.

Figure 3.43 shows the interface between the two sponges through SEM. BTM-SS had collagen sponge seeded with spheroids which had disintegrated in the sponge. Therefore, a circular and homogeneous collagen core is seen in Figures 3.43A and 3.43B. BTM-G shows the hydrogel carrying the spheroids in the core with salt-leached exterior surrounding it and making a close contact (Figure 3.43C). The interaction is more continuous in the model with hydrogel-loaded spheroids, BTM-G (Figure 3.43D). There is a separation between two scaffolds in BTM-SS because of the shrinkage of collagen sponge in the culture duration. In summary, both models were not at sufficient quality to further continue to study.

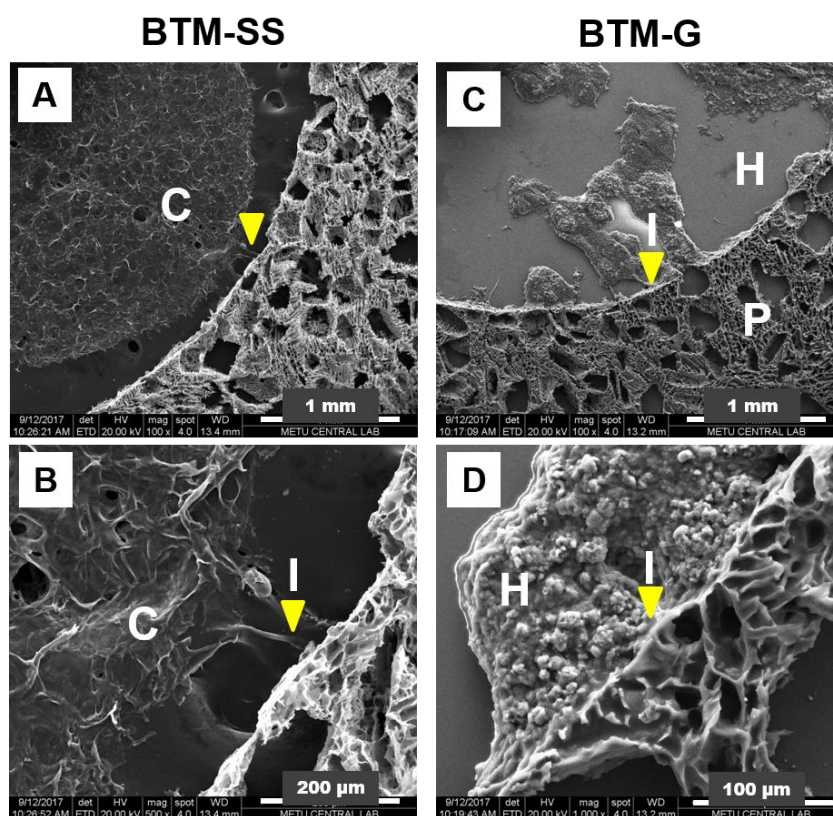


Figure 3.43. SEM analysis of bone tumor models on Day 21. SEM micrographs of horizontal sections of (A, B) BTM-SS, and (C, D) BTM-G with different magnifications. Yellow arrow heads point to the interface between the two components. **C:** Collagen sponge, **H:** Hydrogel, **P:** PLGA/TCP, **I:** Interface.

3.5. Efficacy of Anticancer Agent on BTM-S

Three types of bone tumor models, BTM-S, BTM-SS, and BTM-G, were developed and characterized in this study. However, preparation of spheroids with predetermined number of cells and uniform size is very difficult and this reduces the reproducibility and reliability of the model. Besides, seeding on collagen sponges does not allow them to maintain their spheroid nature. We, therefore, chose BTM-S to use in testing drug efficacy.

3.5.1. Dose-Response Curve and Determination of IC₅₀

In order to assess the suitability of the cancer tissue model we developed in this study, doxorubicin, a drug used in osteosarcoma therapy, was used. A Dose-Response curve was prepared to decide on the concentration of doxorubicin to be used. With this approach, an IC₅₀ value, the concentration of drug that is capable of inhibiting 50% of the cell proliferation, was determined. The Dose-Response curve (Figure 3.44) shows an IC₅₀ value of 0.1876 µg/mL (0.345 µM) when the seeding density was 2x10⁴ cells/well.

In the literature, similar doxorubicin IC₅₀ values of Saos-2 cells in 2D culture were reported: 0.1241 µM (Baek et al., 2016), 0.19 mM (Arai et al., 2013), 0.037 µM (Graat et al., 2006), 0.12 µM (Rimann et al., 2014) and 0.13 µM (Cole et al., 2002). The differences could arise from variations in culture conditions, cell seeding density, passage number of cell line and detection method of cell viability.

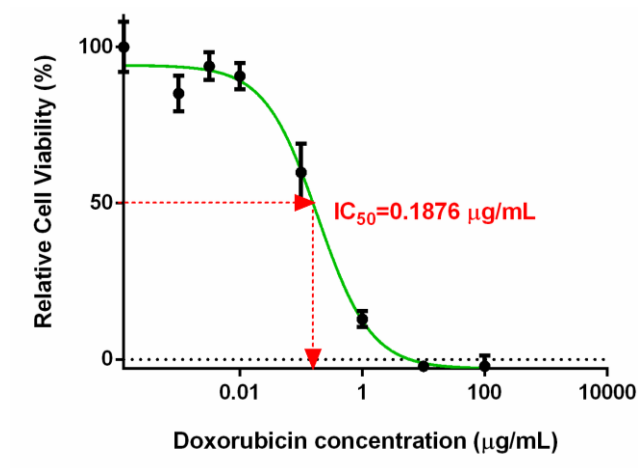


Figure 3.44. Log Dose-Response curve of Saos-2 cells grown in a tissue culture plate treated with doxorubicin. (Cell seeding density = 2×10^4 cells/well).

3.5.2. Alamar Blue Cell Viability Assay

Alamar Blue cell viability test results of untreated BTM-S and doxorubicin-treated BTM-S (BTM-S-D) are presented in Figure 3.45 where reduction (%) of the dye is proportional to live cell number. The cell (Saos-2) number was significantly decreased (approximately 7 fold) as a result of the treatment with doxorubicin. This demonstrated that the model responded properly to the use of the anti-cancer agent doxorubicin.

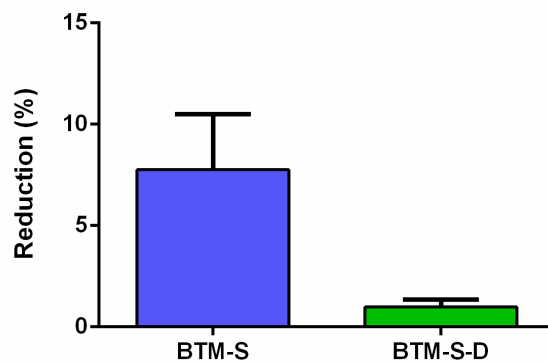


Figure 3.45. Alamar Blue cell viability test results of doxorubicin-treated BTM-S. Reduction (%) of the dye is proportional to live cell number.

The same dose of the drug (2.7 $\mu\text{g}/\text{mL}$) had killed all the cells in the 2D culture of the cells. This indicates that effect in 2D is higher than 3D and shows the difference between the 2D and 3D culture types. Cancer cell monolayers spread on tissue culture plate have direct contact with the drug containing medium over the major part of their surface area, which can result in inaccurate predictions about the efficacy of anticancer drugs. In addition, the expression of many critical signals and key regulators, such as cell-cell attachment molecules and receptors, are less in 2D cultures due to absence of the structural and molecular interactions present in 3D cell cultures or in the complete organism. This significantly suggests that signaling pathways and cellular responses to a specific drug in 3D microenvironments would differ from those observed in monolayers (Levinger et al., 2014). There are reports showing the effects that make tumor cells less sensitive to drugs in 3D than in 2D cultures. These effects decrease in access to drugs in the medium, pathophysiological differences due to hypoxia, differences in the cell cycle (Kapałczyńska et al., 2018). Hsieh et al. showed that inconsistent culture conditions and the type of culture method used can dramatically affect cell metabolic activity and proliferation that results in cell sensitivity to drugs. They also reported that among 2D, 3D and spheroid models, only 3D cell culture, with the same cell density as natural tissue, mimic a drug response comparable to that of a solid tumor (Hsieh et al., 2015). Fong et al. studied the effects of cell-cell contact in doxorubicin resistance in the 3D model by changing the cell density in the models. They found that 3D models seeded with high cell number revealed 8.7-fold greater chemoresistance (IC_{50} , 4.225 μM) than that of low cell number (IC_{50} , 0.485 μM), demonstrating a negative correlation between cell-cell contact and drug sensitivity (Fong et al., 2013). Better communication between the cells in 3D culture may enhance the ability of the cells to prepare for stress caused by drug toxicity. On the other hand, the reason of drug resistance in 3D are still unclear, and current studies are researching whether sensitivity is a result of enhanced cell-cell contact alone or there are other factors (e.g., intracellular changes, paracrine signaling, modifications in the supporting matrix).

In some studies, the reason of chemoresistance in tumor spheroids was shown as a result of limited drug penetration into the innermost cell layers (Burdett et al., 2010; Sutherland et al., 1979). However, Fong et al. compared the drug resistance in Ewing sarcoma cells in 2D culture plate and 3D PCL scaffolds and showed that within the concentration range of doxorubicin after adsorption onto the PCL scaffold, cytotoxicity in 2D is still greater than 90%, demonstrating that the decreased drug sensitivity revealed in 3D is not because of the decreased availability of doxorubicin after adsorption onto the PCL scaffold (Fong et al., 2013). Human MCF-7 cells showed low chemosensitivity to some anticancer agents when culture on porous 3D scaffolds, leading to 12- to 23-fold difference in IC_{50} values of cells in comparison to cells cultured in 2D. It was noted that this difference was related to the low percentage (26%) of cells exposed to toxic drug concentrations in the 3D model by comparing with cells in 2D culture (Horning et al., 2008). In a study, 3D Saos-2 spheroids showed higher IC_{50} values (2.4 fold) for doxorubicin than 2D monolayer culture (Rimann et al., 2014). In another study, a significant decrease in drug response in 3D cells compared to 2D culture cells was shown, which mimics *in vivo* osteosarcoma for treatment (Arai et al., 2013).

Moreover, since doxorubicin targets the actively dividing cells, the cytotoxicity assays for the osteosarcoma cells cultured in the presence of doxorubicin showed that the cells in 2D monolayer culture were more sensitive to doxorubicin than in the 3D scaffolds. As indicated in Section 3.2.1, lower cell division rate of osteosarcoma cells in 3D culture was reported in some studies and this may be the result of lower cytotoxicity of doxorubicin on the 3D culture of Saos-2 (Tan et al., 2016). Consequently, the proliferative state of cells on the scaffolds, the surface area exposure to drug and density of cell-cell contact determine the effectiveness of antimetabolic drugs and demonstrate the importance of 3D to obtain reliable drug efficacy results.

3.5.3. Live/Dead Assay

CLSM micrographs of live/dead stained cells on different parts of the BTM-S are shown in Figure 3.46. The number of dead cells is higher in the doxorubicin-treated BTM-S when compared to untreated ones. Doxorubicin seems to be more effective especially on the top surface of the collagen sponge since this part of the model is in direct contact with the culture medium that contains the drug.

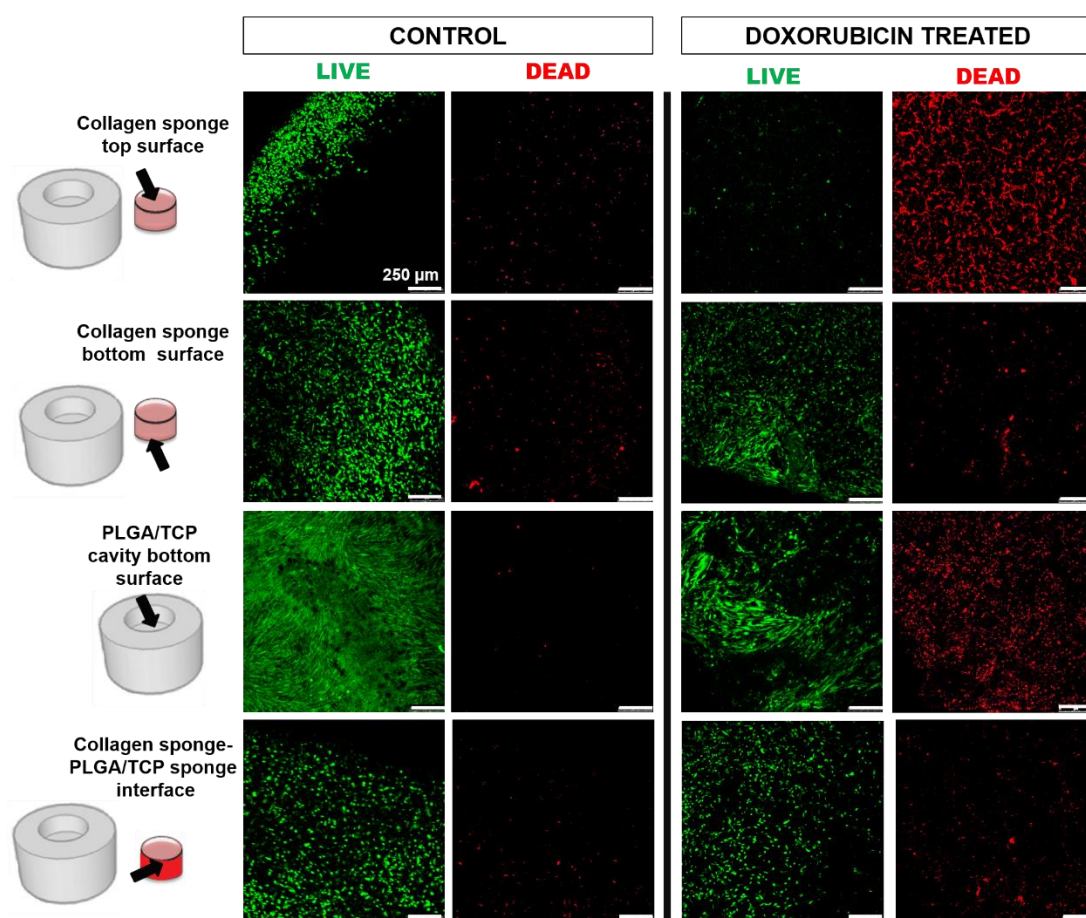


Figure 3.46. Cell viability assay of doxorubicin-treated BTM-S model using Live/Dead staining. The sites of microscopy are shown in the schemes on the left. Calcein AM (green) shows viable cells, ethidium homodimer-1 (red) shows nonviable cells. Scale bar=250 μ m for all images.

Figure 3.46, bottom row, shows the control and drug-treated cells on the collagen sponge that has the direct interface with the healthy bone mimic. This part is not in direct contact with the drug-containing medium and so, the number of dead cells after drug administration is lower than the cells on the collagen sponge top surface. It can be concluded that the BTM-S successfully mimicked the natural bone tumor, and could be a good model for use in drug efficacy studies.

3.5.4. Caspase-3 Enzyme Activity Assay

Caspase-3 enzyme activity is an indicator of apoptosis. Doxorubicin was applied to the bicomponent bone tumor model, BTM-S, and the enzyme activity was measured separately for each component. On the Saos-2 seeded collagen-based tumor mimic the increase in caspase-3 activity is around 2.5 fold whereas on the healthy tissue mimic the caspase-3 activity of drug treated sponge carrying HUVEC and hFOB is almost the same as untreated PLGA/TCP sponge. Therefore, caspase-3 activity on collagen is very significant as expected from the action mechanism (Figure 3.47). It was expected that the drug would be more effective on cancer tissue and cells. This can be a result of the difference in the proliferation rate of the tumor and normal cells. As cancer cells undergo rapid cell divisions, they are generally more susceptible to the effects of doxorubicin than normal cells. In addition, cancer cells often have impaired ability to recognize and/or repair DNA damage, which increases the chance that they cannot properly replicate their DNA, eventually causing cell death by mitotic catastrophe or by apoptosis.

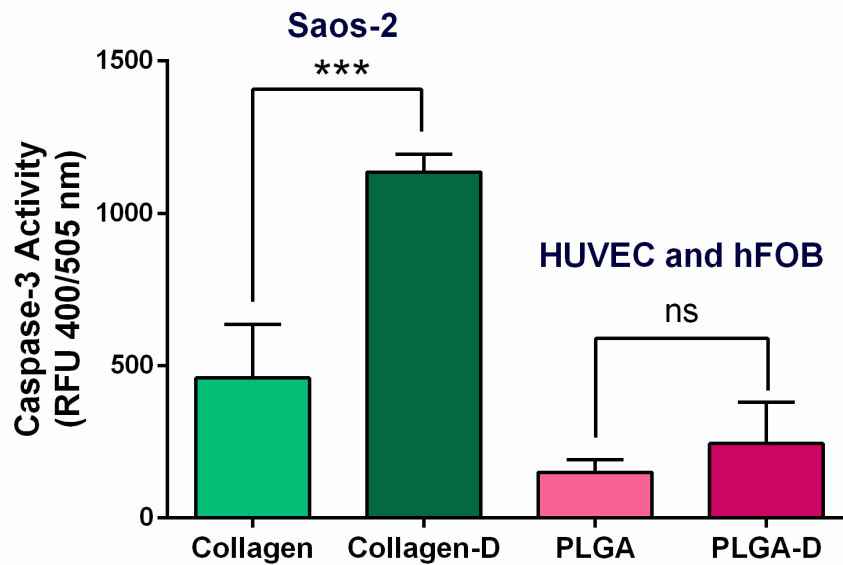


Figure 3.47. Caspase-3 enzyme activity of doxorubicin treated BTM-S. After treatment of doxorubicin on the combined BTM-S model, tumor mimic was removed from healthy bone mimic and caspase-3 enzyme activity assay was carried out separately. Control: Collagen, PLGA. Doxorubicin treated sponges: Collagen-D, PLGA-D.

Moreover, in a study, it was reported that doxorubicin-induced apoptosis originates from different signal transduction mechanism in normal cells, such as endothelial cells and cardiomyocytes (H_2O_2 -dependent), in comparison with tumor cells (p53-dependent). Even, doxorubicin-induced apoptotic cell death in normal versus tumor cells became a promising approach in developing drugs that selectively decrease the toxic side effects of doxorubicin without affecting its antitumor action (Wang et al., 2004). In the present study, the reason for higher caspase-3 enzyme activity in tumor mimic than healthy bone mimic may be due to this different mechanism of doxorubicin on normal and tumor cells.

CHAPTER 4

CONCLUSION

Osteosarcoma (OS) is the most common primary malignant bone tumor in children and adolescents, and is characterized by high local aggressiveness and rapid metastasis capacity leading to an early onset tumor with poor survival. A model of OS was required to study and understand the tumor biology and design and test new drugs without using test animals or 2D test systems which do not properly simulate the tumor tissue. In the present study, the aim was to design a 3D OS model in the form of multicellular 3D culture that would constitute a ‘more clinically relevant’ bone tumor model.

A functional *in vitro* 3D bone tumor (osteosarcoma) model (BTM-S) was successfully designed and constructed by culturing osteosarcoma cells in a collagen scaffold and then by placing it into a healthy bone mimic that was formed by culturing hFOB and HUVECs on the PLGA/TCP scaffolds serving as the healthy bone matrix. This model basically mimicked the *in vivo* tumor stroma by allowing the cancer cells to interact with the healthy bone cells.

Meanwhile, two other bone tumor models were prepared by using Saos-2 spheroids instead of Saos-2 cells and either seeded on collagen sponge or embedded in GelMA hydrogel which were surrounded with healthy bone mimics to construct BTM-SS and BTM-G, respectively. Spheroids preserved their spherical morphology only on the BTM-G; however, difficulty in production of high numbers of spheroids in a short time with known cell number and uniform size and entrapping the same number of spheroids reproducibly in every sample decreased its reliability and reproducibility. Thus, BTM-S was chosen as an actual model and used in drug testing. Angiogenesis and drug efficacy tests were conducted only on the BTM-S.

By constructing a natural bone tumor microenvironment, we showed that cancer cells increase the expression of angiogenic factors when cultured in the 3D model. The anticancer agent, doxorubicin, was tested to study the models functionally and it was observed that drug affects especially the cancer cells. Saos-2 cells cultured on 3D collagen scaffolds show low doxorubicin sensitivity by comparing with the cells cultured on the 2D culture plates, all cells on the culture plate killed after treatment with the same dose of the drug with 3D culture. After doxorubicin administration, a high number of dead cells was observed on the collagen sponge top surface that has the direct contact with the drug containing medium while the number of dead cells was low at the interface of the two tissue mimics and the bottom surface that located far from the drug. These indicate a new strategy in tumor modeling where tumor cells cultured in an engineered bone construct to mimic native host tissue.

In conclusion, it was decided that the 3D BTM-S could be a good candidate to test drug efficacy by creating a reliable 3D tumor microenvironment and is a promising approach in the personalized drug therapy in finding the right type, combination, and dose of the drugs.

REFERENCES

- Abarrategi, A., Tornin, J., Martinez-Cruzado, L., Hamilton, A., Martinez-Campos, E., Rodrigo, J. P., González, M. V., Baldini, N., Garcia-Castro, J., and Rodriguez, R. 2016. Osteosarcoma: Cells-of-Origin, Cancer Stem Cells, and Targeted Therapies. *Stem Cells International*, 2016, 1–13.
- Alemany-Ribes, M., and Semino, C. E. 2014. Bioengineering 3D environments for cancer models. *Advanced Drug Delivery Reviews*, 79, 40–49.
- Alford, A. I., Kozloff, K. M., and Hankenson, K. D. 2015. Extracellular matrix networks in bone remodeling. *The International Journal of Biochemistry and Cell Biology*, 65, 20–31.
- Alfranca, A., Martinez-Cruzado, L., Tornin, J., Abarrategi, A., Amaral, T., de Alava, E., Menendez, P. Garcia-Castro, J., and Rodriguez, R. 2015. Bone microenvironment signals in osteosarcoma development. *Cellular and Molecular Life Sciences*, 72(16), 3097–3113.
- Alghazali, K. M., Nima, Z. A., Hamzah, R. N., Dhar, M. S., Anderson, D. E., and Biris, A. S. 2015. Bone-tissue engineering: complex tunable structural and biological responses to injury, drug delivery, and cell-based therapies. *Drug Metabolism Reviews*, 47(4), 431–454.
- Amini, A. R., Laurencin, C. T., and Nukavarapu, S. P. 2012. Bone Tissue Engineering: Recent Advances and Challenges. *Critical Reviews in Biomedical Engineering*, 40(5), 363.
- Arai, K., Sakamoto, R., Kubota, D., and Kondo, T. 2013. Proteomic approach toward molecular backgrounds of drug resistance of osteosarcoma cells in spheroid culture system. *Proteomics*, 13(15), 2351–2360.
- Arca, T., Proffitt, J., and Genever, P. 2011. Generating 3D tissue constructs with mesenchymal stem cells and a cancellous bone graft for orthopaedic applications. *Biomedical Materials*, 6(2), 025006.
- Arinzeh, T., and Guiro, K. 2016. Bioengineering Models for Breast Cancer Research. *Breast Cancer: Basic and Clinical Research*, 9(Suppl 2), 57.
- Artel, A., Mehdizadeh, H., Chiu, Y.-C., Brey, E. M., and Cinar, A. 2011. An Agent-Based Model for the Investigation of Neovascularization Within Porous Scaffolds. *Tissue Engineering Part A*, 17(17–18), 2133–2141.

- Bachelder, R. E., Crago, A., Chung, J., Wendt, M. A., Shaw, L. M., Robinson, G., and Mercurio, A. M. 2001. Vascular endothelial growth factor is an autocrine survival factor for neuropilin-expressing breast carcinoma cells. *Cancer Research*, 61(15), 5736–5740.
- Baek, N., Seo, O. W., Kim, M., Hulme, J., and An, S. S. A. 2016. Monitoring the effects of doxorubicin on 3D-spheroid tumor cells in real-time. *OncoTargets and Therapy*, 9, 7207–7218.
- Baek, N., Seo, O. W., Lee, J., Hulme, J., and Baek, N. 2016. Real-time monitoring of cisplatin cytotoxicity on three-dimensional spheroid tumor cells. *Drug Design, Development and Therapy*, 10, 2155–2165.
- Baghaban, M., and Faghihi, F. 2011. Mesenchymal Stem Cell-Based Bone Engineering for Bone Regeneration. In *Regenerative Medicine and Tissue Engineering - Cells and Biomaterials*. InTech.
- Borra, R. C., Lotufo, M. A., Gaglioti, S. M., Barros, F. de M., and Andrade, P. M. 2009. A simple method to measure cell viability in proliferation and cytotoxicity assays. *Brazilian Oral Research*, 23(3), 255–262.
- Botter, S. M., Neri, D., and Fuchs, B. 2014. Recent advances in osteosarcoma. *Current Opinion in Pharmacology*, 16, 15–23.
- Bozycki, L., Komiazyk, M., Mebarek, S., Buchet, R., Pikula, S., and Strzelecka-Kiliszek, A. 2018. Analysis of Minerals Produced by hFOB 1.19 and Saos-2 Cells Using Transmission Electron Microscopy with Energy Dispersive X-ray Microanalysis. *Journal of Visualized Experiments*, (136), e57423.
- Burdett, E., Kasper, F. K., Mikos, A. G., and Ludwig, J. A. 2010. Engineering tumors: a tissue engineering perspective in cancer biology. *Tissue Engineering. Part B, Reviews*, 16(3), 351–359.
- Cancer Facts and Statistics 2015 | Research | American Cancer Society. 2015. Retrieved December 25, 2016, from <http://www.cancer.org>.
- Chaddad, H., Kuchler-Bopp, S., Fuhrmann, G., Gegout, H., Ubeaud-Sequier, G., Schwinté, P., Bornert, F., Benkirane-Jessel, N., and Idoux-Gillet, Y. 2017. Combining 2D angiogenesis and 3D osteosarcoma microtissues to improve vascularization. *Experimental Cell Research*, 360(2), 138–145.
- Charoen, K. M., Fallica, B., Colson, Y. L., Zaman, M. H., and Grinstaff, M. W. 2014. Embedded multicellular spheroids as a biomimetic 3D cancer model for evaluating drug and drug-device combinations. *Biomaterials*, 35(7), 2264–2271.
- Chen, C., Chen, K., and Yang, S.-T. 2003. Effects of Three-Dimensional Culturing on Osteosarcoma Cells Grown in a Fibrous Matrix: Analyses of Cell Morphology, Cell Cycle, and Apoptosis. *Biotechnology Progress*, 19(5), 1574–1582.

- Coch, L., Mejias, M., Berzigotti, A., Garcia-Pras, E., Gallego, J., Bosch, J., Mendez, R., and Fernandez, M. 2014. Disruption of negative feedback loop between vasohibin-1 and vascular endothelial growth factor decreases portal pressure, angiogenesis, and fibrosis in cirrhotic rats. *Hepatology*, 60(2), 633–647.
- Cole, P., Smith, A., and Kamen, B. 2002. Osteosarcoma cells, resistant to methotrexate due to nucleoside and nucleobase salvage, are sensitive to nucleoside analogs. *Cancer Chemotherapy and Pharmacology*, 50(2), 111–116.
- Cox, M. C., Reese, L. M., Bickford, L. R., and Verbridge, S. S. 2015. Toward the Broad Adoption of 3D Tumor Models in the Cancer Drug Pipeline. *ACS Biomaterials Science and Engineering*, 1(10), 877–894.
- Craig, L. E., Dittmer, K. E., and Thompson, K. G. 2016. *Bones and Joints*. Jubb, Kennedy and Palmer's Pathology of Domestic Animals: Volume 1. W.B. Saunders.
- Cvelbar, U., Mozetic, M., and Klanjšek-Gunde, M. 2005. Selective oxygen plasma etching of coatings. *IEEE Transactions on Plasma Science*, 33(2), 236–237.
- De Luca, A., Raimondi, L., Salamanna, F., Carina, V., Costa, V., Bellavia, D., Alessandro, R., Fini, M., and Giavaresi, G. 2018. Relevance of 3d culture systems to study osteosarcoma environment. *Journal of Experimental and Clinical Cancer Research : CR*, 37(1), 2.
- Deckers, M. M. L., Karperien, M., van der Bent, C., Yamashita, T., Papapoulos, S. E., and Löwik, C. W. G. M. 2000. Expression of Vascular Endothelial Growth Factors and Their Receptors during Osteoblast Differentiation. *Endocrinology*, 141(5), 1667–1674.
- DiMasi, J. A., Grabowski, H. G. 2007. Economics of New Oncology Drug Development. *Journal of Clinical Oncology*, 25(2), 209–216.
- Doğan, A., Demirci, S., Bayir, Y., Halici, Z., Karakus, E., Aydin, A., Cadirci, E., Albayrak, A., Demirci, E., Karaman, A., Ayan, A. K., Gundogdu, C., and Şahin, F. 2014. Boron containing poly-(lactide-co-glycolide) (PLGA) scaffolds for bone tissue engineering. *Materials Science and Engineering: C*, 44, 246–253.
- Doke, S. K., and Dhawale, S. C. 2015. Alternatives to animal testing: A review. *Saudi Pharmaceutical Journal*, 23(3), 223–229.
- Drexler, J. W., and Powell, H. M. 2011. Dehydrothermal Crosslinking of Electrospun Collagen. *Tissue Engineering Part C: Methods*, 17(1), 9–17.
- Edwards, N., Langford-Smith, A. W. W., Wilkinson, F. L., and Alexander, M. Y. 2018. Endothelial Progenitor Cells: New Targets for Therapeutics for Inflammatory Conditions With High Cardiovascular Risk. *Frontiers in Medicine*, 5, 200.

- Elenjord, R., Allen, J. B., Johansen, H. T., Kildalsen, H., Svineng, G., Maelandsmo, G. M., Loennechen, T., and Winberg, J.-O. 2009. Collagen I regulates matrix metalloproteinase-2 activation in osteosarcoma cells independent of S100A4. *FEBS Journal*, 276(18), 5275–5286.
- Ermis, M., Antmen, E., and Hasirci, V. 2018. Micro and Nanofabrication methods to control cell-substrate interactions and cell behavior: A review from the tissue engineering perspective. *Bioactive Materials*, 3(3), 355–369.
- Fallica, B., Maffei, J. S., Villa, S., Makin, G., and Zaman, M. 2012. Alteration of Cellular Behavior and Response to PI3K Pathway Inhibition by Culture in 3D Collagen Gels. *PLoS ONE*, 7(10), e48024.
- Ferrarini, M., Steimberg, N., Ponzoni, M., Belloni, D., Berenzi, A., Girlanda, S., and Rajkumar, S. 2013. Ex-Vivo Dynamic 3-D Culture of Human Tissues in the RCCS™ Bioreactor Allows the Study of Multiple Myeloma Biology and Response to Therapy. *PLoS one*, 8(8), e71613.
- Fischbach, C., Chen, R., Matsumoto, T., Schmelzle, T., Brugge, J. S., Polverini, P. J., and Mooney, D. J. 2007. Engineering tumors with 3D scaffolds. *Nature Methods*, 4(10), 855–860.
- Fitzgerald, K. A., Guo, J., Tierney, E. G., Curtin, C. M., Malhotra, M., Darcy, R., O'Brien, F. J., and O'Driscoll, C. M. 2015. The use of collagen-based scaffolds to simulate prostate cancer bone metastases with potential for evaluating delivery of nanoparticulate gene therapeutics. *Biomaterials*, 66, 53–66.
- Fong, E. L. S., Lamhamedi-Cherradi, S.-E., Burdett, E., Ramamoorthy, V., Lazar, A. J., Kasper, F. K., Farach-Carson, M. C., Vishwamitra, D., Demicco, E. G., Menegaz, B. A., Amin, H. M., Mikos, A. G., and Ludwig, J. A. 2013. Modeling Ewing sarcoma tumors in vitro with 3D scaffolds. *Proceedings of the National Academy of Sciences of the United States of America*, 110(16), 6500–6505.
- Fong, E. L. S., Wan, X., Yang, J., Morgado, M., Mikos, A. G., Harrington, D. A., Navone, N. M., and Farach-Carson, M. C. 2016. A 3D in vitro model of patient-derived prostate cancer xenograft for controlled interrogation of in vivo tumor-stromal interactions. *Biomaterials*, 77, 164–172.
- Ghaeli, I., de Moraes, M., Beppu, M., Lewandowska, K., Sionkowska, A., Ferreirada-Silva, F., Ferraz, M., and Monteiro, F. 2017. Phase Behaviour and Miscibility Studies of Collagen/Silk Fibroin Macromolecular System in Dilute Solutions and Solid State. *Molecules*, 22(8), 1368.
- Gill, B. J., and West, J. L. 2014. Modeling the tumor extracellular matrix: Tissue engineering tools repurposed towards new frontiers in cancer biology. *Journal of Biomechanics*, 47(9), 1969–1978.

- Godugu, C., Patel, A. R., Desai, U., Andey, T., Sams, A., Singh, M., and Jablons, D. 2013. AlgiMatrix™ Based 3D Cell Culture System as an In-Vitro Tumor Model for Anticancer Studies. *PLoS one*, 8(1), e53708.
- Graat, H. C. A., Witlox, M. A., Schagen, F. H. E., Kaspers, G. J. L., Helder, M. N., Bras, J., and van Beusechem, V. W. 2006. Different susceptibility of osteosarcoma cell lines and primary cells to treatment with oncolytic adenovirus and doxorubicin or cisplatin. *British Journal of Cancer*, 94(12), 1837–1844.
- Graciano, T. B., Coutinho, T. S., Cressoni, C. B., Freitas, C. de P., Pierre, M. B. R., de Lima Pereira, S. A., and Garcia, M. T. J. 2015. Using chitosan gels as a toluidine blue O delivery system for photodynamic therapy of buccal cancer: In vitro and in vivo studies. *Photodiagnosis and Photodynamic Therapy*, 12(1), 98–107.
- Guelcher, S. A. 2008. Biodegradable Polyurethanes: Synthesis and Applications in Regenerative Medicine. *Tissue Engineering Part B: Reviews*, 14(1), 3–17.
- Guijarro, M. V, Ghivizzani, S. C., and Gibbs, C. P. 2014. Animal models in osteosarcoma. *Frontiers in Oncology*, 4, 189.
- Haffner, M. E. (2006). Adopting Orphan Drugs — Two Dozen Years of Treating Rare Diseases. *New England Journal of Medicine*, 354(5), 445–447.
- Hagenmüller, H., Hofmann, S., Kohler, T., Merkle, H. P., Kaplan, D. L., Vunjak-Novakovic, G., Müller, R., and Meinel, L. 2007. Non-Invasive Time-Lapsed Monitoring and Quantification of Engineered Bone-Like Tissue. *Annals of Biomedical Engineering*, 35(10), 1657–1667.
- Harada, S., and Rodan, G. A. 2003. Control of osteoblast function and regulation of bone mass. *Nature*, 423(6937), 349–355.
- Hasirci, V., and Kenar, H. 2006. Novel surface patterning approaches for tissue engineering and their effect on cell behavior. *Nanomedicine*, 1(1), 73–90.
- Hasirci, N., Kilic, C., Kömez, A., Bahcecioglu, G., and Hasirci, V. 2016. Hydrogels in Regenerative Medicine (pp. 1–52).
- Haugh, M. G., Jaasma, M. J., and O'Brien, F. J. 2009. The effect of dehydrothermal treatment on the mechanical and structural properties of collagen-GAG scaffolds. *Journal of Biomedical Materials Research Part A*, 89A(2), 363–369.
- He, X., Kawazoe, N., and Chen, G. 2014. Preparation of cylinder-shaped porous sponges of poly(L-lactic acid), poly(DL-lactic-co-glycolic acid), and poly(ϵ -caprolactone). *BioMed Research International*, 2014, 106082.

- Hickman, J. A., Graeser, R., de Hoogt, R., Vidic, S., Brito, C., Gutekunst, M., and Kuip, H. 2014. Three-dimensional models of cancer for pharmacology and cancer cell biology: Capturing tumor complexity in vitro/ex vivo. *Biotechnology Journal*, 9(9), 1115–1128.
- Hirschhaeuser, F., Menne, H., Dittfeld, C., West, J., Mueller-Klieser, W., and Kunz-Schughart, L. A. 2010. Multicellular tumor spheroids: An underestimated tool is catching up again. *Journal of Biotechnology*, 148(1), 3–15.
- Ho, S. S., Keown, A. T., Addison, B., and Leach, J. K. 2017. Cell Migration and Bone Formation from Mesenchymal Stem Cell Spheroids in Alginate Hydrogels Are Regulated by Adhesive Ligand Density. *Biomacromolecules*, 18(12), 4331–4340.
- Ho, W. J., Pham, E. A., Kim, J. W., Ng, C. W., Kim, J. H., Kamei, D. T., and Wu, B. M. 2010. Incorporation of multicellular spheroids into 3-D polymeric scaffolds provides an improved tumor model for screening anticancer drugs. *Cancer Science*, 101(12), 2637–2643.
- Horning, J. L., Sahoo, S. K., Vijayaraghavalu, S., Dimitrijevic, S., Vasir, J. K., Jain, T. K., Panda, A. K., and Labhasetwar, V. 2008. 3D Tumor Model for In Vitro Evaluation of Anticancer Drugs. *Molecular Pharmaceutics*, 5(5), 849–862.
- Hsieh, C. H., Chen, Y.-D., Huang, S.-F., Wang, H.-M., and Wu, M.-H. 2015. The Effect of Primary Cancer Cell Culture Models on the Results of Drug Chemosensitivity Assays: The Application of Perfusion Microbioreactor System as Cell Culture Vessel. *BioMed Research International*, 2015, 1–10.
- Imparato, G., Urciuolo, F., and Netti, P. A. 2015. In vitro three-dimensional models in cancer research: a review. *International Materials Reviews*, 60(6), 297–311.
- Indovina, P., Rainaldi, G., and Santini, M. T. 2008. Hypoxia increases adhesion and spreading of MG-63 three-dimensional tumor spheroids. *Anticancer Research*, 28(2A), 1013–1022.
- Jang, J.-H., Castano, O., and Kim, H.-W. 2009. Electrospun materials as potential platforms for bone tissue engineering. *Advanced Drug Delivery Reviews*, 61(12), 1065–1083.
- Jeong, S.-Y., Lee, J.-H., Shin, Y., Chung, S., and Kuh, H. J. 2016. Co-Culture of Tumor Spheroids and Fibroblasts in a Collagen Matrix-Incorporated Microfluidic Chip Mimics Reciprocal Activation in Solid Tumor Microenvironment. *PLoS one*, 11(7), e0159013.
- Kapałczyńska, M., Kolenda, T., Przybyła, W., Zajączkowska, M., Teresiak, A., Filas, V., Ibs, M., Bliźniak, R., Łuczewski, Ł., and Lamperska, K. 2018. 2D and 3D cell cultures - a comparison of different types of cancer cell cultures. *Archives of Medical Science : AMS*, 14(4), 910–919.

- Kaufmann, J. E., Oksche, A., Wollheim, C. B., Günther, G., Rosenthal, W., and Vischer, U. M. 2000. Vasopressin-induced von Willebrand factor secretion from endothelial cells involves V2 receptors and cAMP. *The Journal of Clinical Investigation*, 106(1), 107–116.
- Keogh, M. B., O'Brien, F. J., and Daly, J. S. 2010. Substrate stiffness and contractile behaviour modulate the functional maturation of osteoblasts on a collagen–GAG scaffold. *Acta Biomaterialia*, 6(11), 4305–4313.
- Khojasteh, A., Fahimipour, F., Eslaminejad, M. B., Jafarian, M., Jahangir, S., Bastami, F., Tahriri, M., Karkhaneh, A., and Tayebi, L. (2016). Development of PLGA-coated β -TCP scaffolds containing VEGF for bone tissue engineering. *Materials Science and Engineering: C*, 69, 780–788.
- Kilic Bektas, C., and Hasirci, V. 2018. Mimicking corneal stroma using keratocyte-loaded photopolymerizable methacrylated gelatin hydrogels. *Journal of Tissue Engineering and Regenerative Medicine*, 12(4), e1899–e1910.
- Kilic, C., Girotti, A., Rodriguez-Cabello, J. C., and Hasirci, V. 2014. A collagen-based corneal stroma substitute with micro-designed architecture. *Biomater. Sci.*, 2(3), 318–329.
- Kim, M., Lee, J. Y., Jones, C. N., Revzin, A., and Tae, G. 2010. Heparin-based hydrogel as a matrix for encapsulation and cultivation of primary hepatocytes. *Biomaterials*, 31(13), 3596–3603.
- Kim, S. H., Kim, S. H., and Jung, Y. 2015. Bi-layered PLCL/(PLGA/ β -TCP) composite scaffold for osteochondral tissue engineering. *Journal of Bioactive and Compatible Polymers*, 30(2), 178–187.
- Kimlin, L. C., Casagrande, G., and Virador, V. M. 2013. In vitro three-dimensional (3D) models in cancer research: An update. *Molecular Carcinogenesis*, 52(3), 167–182.
- Kola, I., and Landis, J. 2004. Opinion: Can the pharmaceutical industry reduce attrition rates? *Nature Reviews Drug Discovery*, 3(8), 711–716.
- Komez, A., Baran, E. T., Erdem, U., Hasirci, N., and Hasirci, V. 2016. Construction of a Patterned Hydrogel - Fibrous Mat Bilayer Structure to Mimic Choroid and Bruch's Membrane Layers of Retina. *Journal of Biomedical Materials Research Part A*, 104(9), 2166-2177.
- Kozłowska, J., Sionkowska, A., Osyczka, A. M., and Dubiel, M. 2017. Stabilizing effect of carbodiimide and dehydrothermal treatment crosslinking on the properties of collagen/hydroxyapatite scaffolds. *Polymer International*, 66(8), 1164–1172.

- Kwakwa, K. A., Vanderburgh, J. P., Guelcher, S. A., and Sterling, J. A. 2017. Engineering 3D Models of Tumors and Bone to Understand Tumor-Induced Bone Disease and Improve Treatments. *Current Osteoporosis Reports*, 15(4), 247–254.
- Kwon, H., Kim, H. J., Rice, W. L., Subramanian, B., Park, S.-H., Georgakoudi, I., and Kaplan, D. L. 2010. Development of an in vitro model to study the impact of BMP-2 on metastasis to bone. *Journal of Tissue Engineering and Regenerative Medicine*, 4(8), 590–599.
- Lama, R., Zhang, L., Naim, J. M., Williams, J., Zhou, A., and Su, B. 2013. Development, validation and pilot screening of an in vitro multi-cellular three-dimensional cancer spheroid assay for anti-cancer drug testing. *Bioorganic and Medicinal Chemistry*, 21(4), 922–931.
- Lamhamedi-Cherradi, S.-E., Santoro, M., Ramammoorthy, V., Menegaz, B. A., Bartholomeusz, G., Iles, L. R., Amin, H. M., Livingston, J. A., Mikos, A. G. and Ludwig, J. A. 2014. 3D tissue-engineered model of Ewing's sarcoma. *Advanced Drug Delivery Reviews*, 79–80, 155–171.
- Langer, R., and Vacanti, J. P. 1993. Tissue engineering. *Science (New York, N.Y.)*, 260(5110), 920–926.
- Laschke, M. W., Schank, T. E., Scheuer, C., Kleer, S., Schuler, S., Metzger, W., Eglin, D., Alini, M., and Menger, M. D. 2013. Three-dimensional spheroids of adipose-derived mesenchymal stem cells are potent initiators of blood vessel formation in porous polyurethane scaffolds. *Acta Biomaterialia*, 9(6), 6876–6884.
- Lee, K. H., No, D. Y., Kim, S.-H., Ryoo, J. H., Wong, S. F., and Lee, S.-H. 2011. Diffusion-mediated in situ alginate encapsulation of cell spheroids using microscale concave well and nanoporous membrane. *Lab on a Chip*, 11(6), 1168.
- Lee, S. K., Han, C.-M., Park, W., Kim, I. H., Joung, Y. K., and Han, D. K. 2019. Synergistically enhanced osteoconductivity and anti-inflammation of PLGA/ β -TCP/Mg(OH)₂ composite for orthopedic applications. *Materials Science and Engineering. C, Materials for Biological Applications*, 94, 65–75.
- Lehocký, M., Drnovská, H., Lapčíková, B., Barros-Timmons, A., Trindade, T., Zembala, M., and Lapčík, L. 2003. Plasma surface modification of polyethylene. *Colloids and Surfaces A: Physicochemical and Engineering Aspects*, 222(1–3), 125–131.
- Leikin, S., Rau, D. C., and Parsegian, V. A. 1995. Temperature-favoured assembly of collagen is driven by hydrophilic not hydrophobic interactions. *Nature Structural Biology*, 2(3), 205–210.

- Levinger, I., Ventura, Y., and Vago, R. 2014. Life is Three Dimensional—As In Vitro Cancer Cultures Should Be. In *Advances in cancer research*, 121, 383–414.
- Lian, J. B., Stein, G. S., van Wijnen, A. J., Stein, J. L., Hassan, M. Q., Gaur, T., and Zhang, Y. 2012. MicroRNA control of bone formation and homeostasis. *Nature Reviews Endocrinology*, 8(4), 212–227.
- Liang, Y., Jeong, J., DeVolder, R. J., Cha, C., Wang, F., Tong, Y. W., and Kong, H. 2011. A cell-instructive hydrogel to regulate malignancy of 3D tumor spheroids with matrix rigidity. *Biomaterials*, 32(35), 9308–9315.
- Lin, L., and Gao, H. 2016. Modification of β -TCP/PLGA scaffold and its effect on bone regeneration in vivo. *Journal of Wuhan University of Technology-Mater. Sci. Ed.*, 31(2), 454–460.
- Llorens, E., Calderón, S., del Valle, L. J., and Puiggali, J. 2015. Polybiguanide (PHMB) loaded in PLA scaffolds displaying high hydrophobic, biocompatibility and antibacterial properties. *Materials Science and Engineering: C*, 50, 74–84.
- Lobov, I. B., Renard, R. A., Papadopoulos, N., Gale, N. W., Thurston, G., Yancopoulos, G. D., and Wiegand, S. J. 2007. Delta-like ligand 4 (Dll4) is induced by VEGF as a negative regulator of angiogenic sprouting. *Proceedings of the National Academy of Sciences*, 104(9), 3219–3224.
- Ma, L., Barker, J., Zhou, C., Li, W., Zhang, J., Lin, B., Foltz, G., Küblbeck, J., and Honkakoski, P. 2012. Towards personalized medicine with a three-dimensional micro-scale perfusion-based two-chamber tissue model system. *Biomaterials*, 33(17), 4353–4361.
- Meinel, L., Hofmann, S., Betz, O., Fajardo, R., Merkle, H. P., Langer, R., Evans, C. H., Vunjak-Novakovic, G., and Kaplan, D. L. 2006. Osteogenesis by human mesenchymal stem cells cultured on silk biomaterials: Comparison of adenovirus mediated gene transfer and protein delivery of BMP-2. *Biomaterials*, 27(28), 4993–5002.
- Melke, J., Midha, S., Ghosh, S., Ito, K., and Hofmann, S. 2016. Silk fibroin as biomaterial for bone tissue engineering. *Acta Biomaterialia*, 31, 1–16.
- Mohseny, A. B., Hogendoorn, P. C. W., and Cleton-Jansen, A.-M. 2012. Osteosarcoma Models: From Cell Lines to Zebrafish. *Sarcoma*, 2012, 1–11.
- Mygind, T., Stiehler, M., Baatrup, A., Li, H., Zou, X., Flyvbjerg, A., and Bünger, C. 2007. Mesenchymal stem cell ingrowth and differentiation on coralline hydroxyapatite scaffolds. *Biomaterials*, 28(6), 1036–1047.
- Naito, Y., Shinoka, T., Duncan, D., Hibino, N., Solomon, D., Cleary, M., and Breuer, C. 2011. Vascular tissue engineering: Towards the next generation vascular grafts. *Advanced Drug Delivery Reviews*, 63(4–5), 312–323.

- NIH Categorical Spending -NIH Research Portfolio Online Reporting Tools (RePORT). (n.d.).
- Ning, Y., Manegold, P. C., Hong, Y. K., Zhang, W., Pohl, A., Lurje, G., and Lenz, H.-J. 2011. Interleukin-8 is associated with proliferation, migration, angiogenesis and chemosensitivity in vitro and in vivo in colon cancer cell line models. *International Journal of Cancer*, 128(9), 2038–2049.
- Oliveira, M. B., Neto, A. I., Correia, C. R., Rial-Hermida, M. I., Alvarez-Lorenzo, C., and Mano, J. F. 2014. Superhydrophobic Chips for Cell Spheroids High-Throughput Generation and Drug Screening. *ACS Applied Materials and Interfaces*, 6(12), 9488–9495.
- Pampaloni, F., Reynaud, E. G., and Stelzer, E. H. K. 2007. The third dimension bridges the gap between cell culture and live tissue. *Nature Reviews Molecular Cell Biology*, 8(10), 839–845.
- Pang, L., Hu, Y., Yan, Y., Liu, L., Xiong, Z., Wei, Y., and Bai, J. 2007. Surface modification of PLGA/ β -TCP scaffold for bone tissue engineering: Hybridization with collagen and apatite. *Surface and Coatings Technology*, 201(24), 9549–9557.
- Pathi, S. P., Kowalczewski, C., Tadipatri, R., Fischbach, C., Guise, T., Mundy, G., and Yasuda, H. 2010. A Novel 3-D Mineralized Tumor Model to Study Breast Cancer Bone Metastasis. *PLoS ONE*, 5(1), e8849.
- Pattnaik, S., Nethala, S., Tripathi, A., Saravanan, S., Moorthi, A., and Selvamurugan, N. 2011. Chitosan scaffolds containing silicon dioxide and zirconia nano particles for bone tissue engineering. *International Journal of Biological Macromolecules*, 49(5), 1167–1172.
- Peister, A., Deutsch, E. R., Kolambkar, Y., Hutmacher, D. W., and Guldberg, R. E. 2009. Amniotic Fluid Stem Cells Produce Robust Mineral Deposits on Biodegradable Scaffolds. *Tissue Engineering Part A*, 15(10), 3129–3138.
- Peister, A., Woodruff, M. A., Prince, J. J., Gray, D. P., Hutmacher, D. W., and Guldberg, R. E. 2011. Cell sourcing for bone tissue engineering: Amniotic fluid stem cells have a delayed, robust differentiation compared to mesenchymal stem cells. *Stem Cell Research*, 7(1), 17–27.
- Peng, N., Gao, S., Guo, X., Wang, G., Cheng, C., Li, M., and Liu, K. 2016. Silencing of VEGF inhibits human osteosarcoma angiogenesis and promotes cell apoptosis via VEGF/PI3K/AKT signaling pathway. *American Journal of Translational Research*, 8(2), 1005–1015.

- Petrovito, L., Leo, A., Gori, V., Lulli, M., Parri, M., Becherucci, V., Chiarugi, P. 2018. Bone marrow-derived mesenchymal stem cells promote invasiveness and transendothelial migration of osteosarcoma cells via a mesenchymal to amoeboid transition. *Molecular Oncology*, 12(5), 659–676. 7.
- Porter, B., Lin, A., Peister, A., Hutmacher, D., and Guldberg, R. (2007). Noninvasive image analysis of 3D construct mineralization in a perfusion bioreactor. *Biomaterials*, 28(15), 2525–2533.
- Porter, J. R., Ruckh, T. T., and Popat, K. C. 2009. Bone tissue engineering: A review in bone biomimetics and drug delivery strategies. *Biotechnology Progress*, 25(6), 1539-1560.
- Pradhan, S., Clary, J. M., Seliktar, D., and Lipke, E. A. 2017. A three-dimensional spheroidal cancer model based on PEG-fibrinogen hydrogel microspheres. *Biomaterials*, 115, 141–154.
- Pulieri, E., Chiono, V., Ciardelli, G., Vozi, G., Ahluwalia, A., Domenici, C., and Giusti, P. 2008. Chitosan/gelatin blends for biomedical applications. *Journal of Biomedical Materials Research Part A*, 86A(2), 311–322.
- Raggatt, L. J., and Partridge, N. C. 2010. Cellular and Molecular Mechanisms of Bone Remodeling. *Journal of Biological Chemistry*, 285(33), 25103–25108.
- Ramírez-Rodríguez, G. B., Montesi, M., Panseri, S., Sprio, S., Tampieri, A., and Sandri, M. 2017. Biom mineralized Recombinant Collagen-Based Scaffold Mimicking Native Bone Enhances Mesenchymal Stem Cell Interaction and Differentiation. *Tissue Engineering Part A*, 23(23–24), 1423–1435.
- Reinke, S. K., Hauf, K., Vieira, J., Heinrich, S., and Palzer, S. 2015. Changes in contact angle providing evidence for surface alteration in multi-component solid foods. *Journal of Physics D: Applied Physics*, 48(46), 464001.
- Rimann, M., Laternser, S., Gvozdenovic, A., Muff, R., Fuchs, B., Kelm, J. M., and Graf-Hausner, U. 2014. An in vitro osteosarcoma 3D microtissue model for drug development. *Journal of Biotechnology*, 189, 129–135.
- Rosso, F., Giordano, A., Barbarisi, M., and Barbarisi, A. 2004. From Cell-ECM interactions to tissue engineering. *Journal of Cellular Physiology*, 199(2), 174–180.
- Saalfrank, A., Janssen, K.-P., Ravon, M., Flisikowski, K., Eser, S., Steiger, K., and Schnieke, A. 2016. A porcine model of osteosarcoma. *Oncogenesis*, 5(3), e210–e210.
- Saito, T., Takeda, N., Amiya, E., Nakao, T., Abe, H., Semba, H., and Maemura, K. 2013. VEGF-A induces its negative regulator, soluble form of VEGFR-1, by modulating its alternative splicing. *FEBS Letters*, 587(14), 2179–2185.

- Salgado, A. J., Coutinho, O. P., and Reis, R. L. 2004. Bone Tissue Engineering: State of the Art and Future Trends. *Macromolecular Bioscience*, 4(8), 743–765.
- Sanjeeb K. Sahoo, Amulya K. Panda, and Labhassetwar, V. 2005. Characterization of Porous PLGA/PLA Microparticles as a Scaffold for Three Dimensional Growth of Breast Cancer Cells, *Biomacromolecules*, 6(2), 1132-1139.
- Schmidt, M., Scholz, C.-J., Polednik, C., and Roller, J. 2016. Spheroid-based 3-dimensional culture models: Gene expression and functionality in head and neck cancer. *Oncology Reports*, 35(4), 2431–2440.
- Schuessler, T. K., Chan, X. Y., Chen, H. J., Ji, K., Park, K. M., Roshan-Ghias, A., and Kuhn, N. Z. 2014. Biomimetic tissue-engineered systems for advancing cancer research: NCI Strategic Workshop report. *Cancer Research*, 74(19), 5359–5363.
- Seong, J. M., Kim, B.-C., Park, J.-H., Kwon, I. K., Mantalaris, A., and Hwang, Y.-S. 2010. Stem cells in bone tissue engineering. *Biomedical Materials*, 5(6), 062001.
- Sitarski, A. M., Fairfield, H., Falank, C., and Reagan, M. R. 2018. 3D Tissue Engineered in Vitro Models of Cancer in Bone. *ACS Biomaterials Science and Engineering*, 4(2), 324–336.
- Subburaj, K., Ravi, B., and Agarwal, M. 2010. Computer-aided methods for assessing lower limb deformities in orthopaedic surgery planning. *Computerized Medical Imaging and Graphics*, 34(4), 277–288.
- Sun, L., Li, B., Yao, D., Song, W., and Hou, H. 2018. Effects of cross-linking on mechanical, biological properties and biodegradation behavior of Nile tilapia skin collagen sponge as a biomedical material. *Journal of the Mechanical Behavior of Biomedical Materials*, 80, 51–58.
- Sutherland, R. M., Eddy, H. A., Bareham, B., Reich, K., and Vanantwerp, D. 1979. Resistance to adriamycin in multicellular spheroids. *International Journal of Radiation Oncology, Biology, Physics*, 5(8), 1225–1230.
- Suzuki, Y., Kobayashi, M., Miyashita, H., Ohta, H., Sonoda, H., and Sato, Y. 2010. Isolation of a small vasohibin-binding protein (SVBP) and its role in vasohibin secretion. *Journal of Cell Science*, 123(18), 3094–3101.
- Talukdar, S., Mandal, M., Hutmacher, D. W., Russell, P. J., Soekmadji, C., and Kundu, S. C. (2011). Engineered silk fibroin protein 3D matrices for in vitro tumor model. *Biomaterials*, 32(8), 2149–2159.
- Tan, M. L., Shao, P., Friedhuber, A. M., van Moorst, M., Elahy, M., Indumathy, S., and Dass, C. R. 2014. The potential role of free chitosan in bone trauma and bone cancer management. *Biomaterials*, 35(27), 7828–7838.

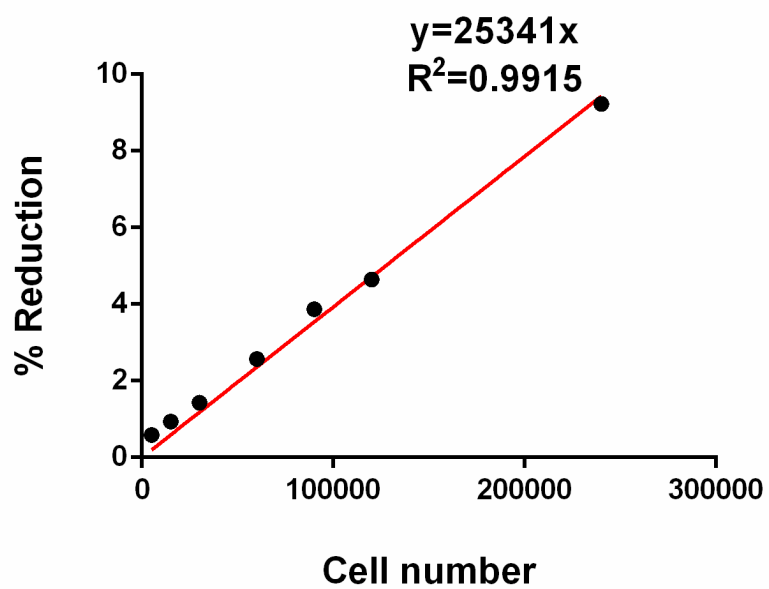
- Tan, P. H. S., Aung, K. Z., Toh, S. L., Goh, J. C. H., and Nathan, S. S. 2011. Three-dimensional porous silk tumor constructs in the approximation of in vivo osteosarcoma physiology. *Biomaterials*, 32(26), 6131–6137.
- Tan, P. H. S., Chia, S. S., Toh, S. L., Goh, J. C. H., and Nathan, S. S. 2014. The dominant role of IL-8 as an angiogenic driver in a three-dimensional physiological tumor construct for drug testing. *Tissue Engineering. Part A*, 20(11–12), 1758–1766.
- Tan, P. H. S., Chia, S. S., Toh, S. L., Goh, J. C. H., and Nathan, S. S. 2016. Three-dimensional spatial configuration of tumour cells confers resistance to chemotherapy independent of drug delivery. *Journal of Tissue Engineering and Regenerative Medicine*, 10(8), 637–646.
- Thimm, B. W., Wechsler, O., Bohner, M., Müller, R., and Hofmann, S. 2013. In Vitro Ceramic Scaffold Mineralization: Comparison Between Histological and Micro-Computed Tomographical Analysis. *Annals of Biomedical Engineering*, 41(12), 2666–2675.
- Uluçkan, Ö., Segaliny, A., Botter, S., Santiago, J. M., and Mutsaers, A. J. 2015. Preclinical mouse models of osteosarcoma. *BoneKEy Reports*, 4, 670.
- Venkatesan, J., Bhatnagar, I., Manivasagan, P., Kang, K.-H., and Kim, S.-K. 2015. Alginate composites for bone tissue engineering: A review. *International Journal of Biological Macromolecules*, 72, 269–281.
- Verbridge, S. S., Choi, N. W., Zheng, Y., Brooks, D. J., Stroock, A. D., and Fischbach, C. 2010. Oxygen-Controlled Three-Dimensional Cultures to Analyze Tumor Angiogenesis. *Tissue Engineering Part A*, 16(7), 2133–2141.
- Verrecchia, F., and Rédini, F. 2018. Transforming Growth Factor- β Signaling Plays a Pivotal Role in the Interplay Between Osteosarcoma Cells and Their Microenvironment. *Frontiers in Oncology*, 8, 133.
- Villasante, A., Marturano-Kruik, A., and Vunjak-Novakovic, G. 2014. Bioengineered human tumor within a bone niche. *Biomaterials*, 35(22), 5785–5794.
- Villasante, A., and Vunjak-Novakovic, G. 2015. Tissue-engineered models of human tumors for cancer research. *Expert Opinion on Drug Discovery*, 10(3), 257–268.
- Wang, S., Konorev, E. A., Kotamraju, S., Joseph, J., Kalivendi, S., and Kalyanaraman, B. 2004. Doxorubicin Induces Apoptosis in Normal and Tumor Cells via Distinctly Different Mechanisms. *Journal of Biological Chemistry*, 279(24), 25535–25543.
- Wastfelt, M., Fadeel, B., and Henter, J.-I. 2006. A journey of hope: lessons learned from studies on rare diseases and orphan drugs. *Journal of Internal Medicine*, 260(1), 1–10.

- Weadock, K. S., Miller, E. J., Keuffel, E. L., and Dunn, M. G. 1996. Effect of physical crosslinking methods on collagen-fiber durability in proteolytic solutions. *Journal of Biomedical Materials Research*, 32(2), 221–226.
- Wu, L., and Ding, J. 2004. In vitro degradation of three-dimensional porous poly(d,l-lactide-co-glycolide) scaffolds for tissue engineering. *Biomaterials*, 25(27), 5821–5830.
- Wu, Y., Adeeb, S., and Doschak, M. R. 2015. Using Micro-CT Derived Bone Microarchitecture to Analyze Bone Stiffness - A Case Study on Osteoporosis Rat Bone. *Frontiers in Endocrinology*, 6, 80.
- Xie, X.-H., Wang, X.-L., Zhang, G., He, Y.-X., Wang, X.-H., Liu, Z., and Qin, L. 2010. Structural and degradation characteristics of an innovative porous PLGA/TCP scaffold incorporated with bioactive molecular icaritin. *Biomedical Materials*, 5(5), 054109.
- Xu, X., Farach-Carson, M. C., and Jia, X. 2014. Three-dimensional in vitro tumor models for cancer research and drug evaluation. *Biotechnology Advances*, 32(7), 1256–1268.
- Xu, X., Gurski, L. A., Zhang, C., Harrington, D. A., Farach-Carson, M. C., and Jia, X. 2012. Recreating the tumor microenvironment in a bilayer, hyaluronic acid hydrogel construct for the growth of prostate cancer spheroids. *Biomaterials*, 33(35), 9049–9060.
- Yahyouche, A., Zhidao, X., Czernuszka, J. T., and Clover, A. J. P. 2011. Macrophage-mediated degradation of crosslinked collagen scaffolds. *Acta Biomaterialia*, 7(1), 278–286.
- Yang, Y., Tang, G., Zhao, Y., Zhang, Y., Li, X., and Yuan, X. 2011. Effect of degradation of PLGA and PLGA/ β -TCP scaffolds on the growth of osteoblasts. *Chinese Science Bulletin*, 56(10), 982–986.
- Zanoni, M., Piccinini, F., Arienti, C., Zamagni, A., Santi, S., Polico, R., and Bevilacqua, A. 2016. 3D tumor spheroid models for in vitro therapeutic screening: a systematic approach to enhance the biological relevance of data obtained. *Scientific Reports*, 6, 19103.
- Zanoni, M., Piccinini, F., Arienti, C., Zamagni, A., Santi, S., Polico, R., and Tesei, A. 2016. 3D tumor spheroid models for in vitro therapeutic screening: a systematic approach to enhance the biological relevance of data obtained. *Scientific Reports*, 6(1), 19103.
- Zhang, M., Li, X. H., Gong, Y. D., Zhao, N. M., and Zhang, X. F. 2002. Properties and biocompatibility of chitosan films modified by blending with PEG. *Biomaterials*, 23(13), 2641–2648.

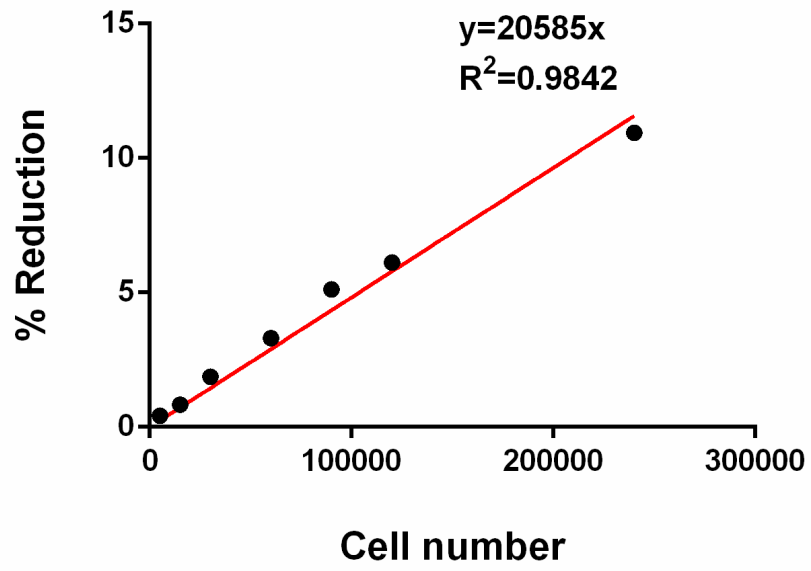
- Zhang, N., Yan, H., and Wen, X. 2005. Tissue-engineering approaches for axonal guidance. *Brain Research Reviews*, 49(1), 48–64.
- Zhang, P., Wu, H., Wu, H., Lù, Z., Deng, C., Hong, Z., and Chen, X. 2011. RGD-Conjugated Copolymer Incorporated into Composite of Poly(lactide-co-glycotide) and Poly(l-lactide)-Grafted Nanohydroxyapatite for Bone Tissue Engineering. *Biomacromolecules*, 12(7), 2667–2680.
- Zhou, H., Lawrence, J. G., and Bhaduri, S. B. 2012. Fabrication aspects of PLA-CaP/PLGA-CaP composites for orthopedic applications: A review. *Acta Biomaterialia*, 8(6), 1999–2016.

APPENDICES

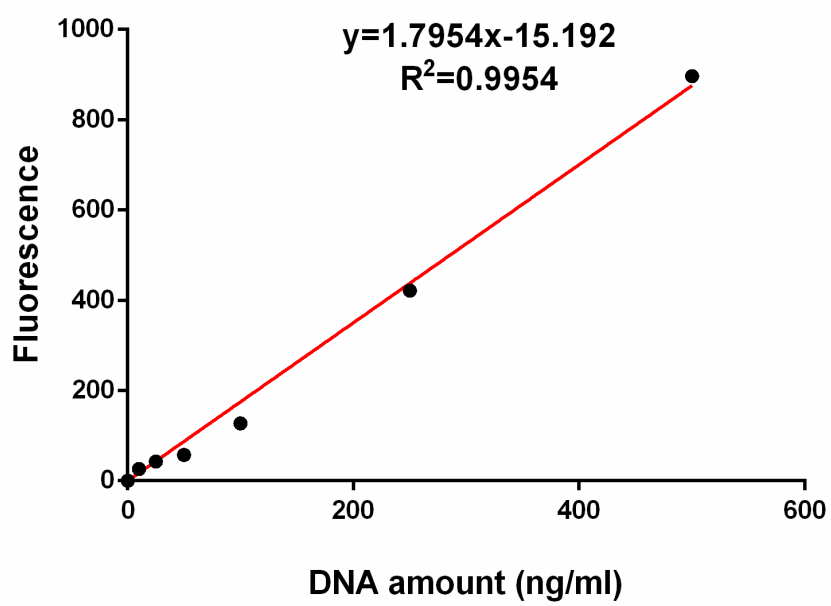
A. Alamar Blue Assay Calibration Curve for hFOB and HUVECs



B. Alamar Blue Assay Calibration Curve for Saos-2



C. Standard Curve for DNA Quantification



CURRICULUM VITAE

PERSONAL INFORMATION

Surname, Name : Kömez, Aylin
Nationality : Turkish (TC)
Date and Place of Birth : 01 January 1989, Ankara
Phone : +90 312 210 51 93
E-mail : komez.aylin@metu.edu.tr

EDUCATION

Degree	Institution	Year of Graduation
PhD	METU, Dept. of Biotechnology	2019
MS	METU, Dept. of Biotechnology	2015
BS	METU, Dept. of Biological Science	2012
High School	Cumhuriyet Anatolian High School, Ankara	2006

FOREIGN LANGUAGES

Advanced English

PUBLICATIONS

Komez A., Buyuksungur A., Antmen E., Hasirci N., Hasirci V. “3D Bone Tumor Model Designed for Screening Efficacy of Drugs for Personalized Therapy” (2019). (Submitted)

Komez A., Buyuksungur S., Hasirci V., Hasirci N. “Effect of chemical structure on properties of polyurethanes: Temperature responsiveness and biocompatibility”, *Journal of Bioactive and Compatible Polymers*, 33(5), 479-497 (2018).

Komez A., Baran E. T., Erdem U., Hasirci N., Hasirci V. “Construction of a Patterned Hydrogel - Fibrous Mat Bilayer Structure to Mimic Choroid and Bruch’s Membrane Layers of Retina”, *Journal of Biomedical Materials Research Part A*, 104(9), 2166-2177 (2016).

Hasirci N., Kilic C., **Komez A.**, Bahcecioglu G., Hasirci V. “Hydrogels in regenerative medicine”, GELS HANDBOOK: Fundamentals, Properties and Applications Volume 2. World Scientific Publishing. (2016).

CONFERENCE PROCEEDINGS

Komez A., Buyuksungur A., Antmen E., Hasirci N., Hasirci V. *İn Vitro* Koşullarda 3 Boyutlu Kemik Tümör Modeli Geliştirilmesi. 23. Biyomedikal Bilim ve Teknoloji Sempozyumu (BIOMED2018-TR), 15-16 December, 2018, İstanbul, Turkey (*Poster Presentation*).

Komez A., Buyuksungur A., Antmen E., Hasirci N., Hasirci V. Development of an *in vitro* 3D Bone Tumor Model. 2nd International Biomedical Engineering Congress 2018 (IBMEC-2018), 24-27 May 2018, North Cyprus (*Oral Presentation*).

Komez A., Baran E.T., Hasirci N., Hasirci V. Construction of Retina Substitute by Using Tissue Engineering Approach. 1st East West Asia Biomaterials Symposium EWAB 2015, 21 October 2015, Antalya, Turkey (*Oral Presentation*).

Komez A., Baran E.T., Hasirci N., Hasirci V. Construction of Retina Substitute by Using Tissue Engineering Approach. International Symposium on Biomedical Science and Technology (BIOMED), October 2015, Antalya, Turkey (*Poster Presentation*).

Komez A., Buyuksungur S., Hasirci V., Hasirci N. Synthesis of Polyurethane for Coating of Neurostimulator. BIOMED 2015, October 2015, Antalya, Turkey (*Poster Presentation*).

Komez A., Baran E.T., Hasirci N., Hasirci V. Vascular network generation in hyaluronic acid by micromolding and photoimmobilization of fibronectin, 26th Annual Conference of the European Society for Biomaterials (ESB), 31 August – 3 September 2014, Liverpool, UK (*Oral Presentation*)

HOBBIES

Classical Turkish Music, Playing Kanun (beginner level), Nature Discovery